

UNIVERSITÉ DE MONTRÉAL

ADVANCED INSTRUMENTATION FOR PRACTICAL APPLICATIONS OF
TERAHERTZ SPECTROSCOPY AND IMAGING

HICHEM GUERBOUKHA
DÉPARTEMENT DE GÉNIE PHYSIQUE
ÉCOLE POLYTECHNIQUE DE MONTRÉAL

MÉMOIRE PRÉSENTÉ EN VUE DE L'OBTENTION
DU DIPLÔME DE MAÎTRISE ÈS SCIENCES APPLIQUÉES
(GÉNIE PHYSIQUE)
MAI 2015

UNIVERSITÉ DE MONTRÉAL

ÉCOLE POLYTECHNIQUE DE MONTRÉAL

Ce mémoire intitulé:

ADVANCED INSTRUMENTATION FOR PRACTICAL APPLICATIONS OF
TERAHERTZ SPECTROSCOPY AND IMAGING

présenté par: GUERBOUKHA Hichem

en vue de l'obtention du diplôme de: Maîtrise ès sciences appliquées

a été dûment accepté par le jury d'examen constitué de:

M. LEBLOND Frédéric, Ph. D., président

M. SKOROBOGATIY Maksim A., Ph. D., membre et directeur de recherche

M. YAMILOV Alexey G., Ph. D., membre

ACKNOWLEDGEMENTS

I would like to express my sincere gratitude to Prof. Maksim Skorobogatiy for his great support and guidance. Under his supervision, I learned more than I could have ever thought. These past two years were full of discoveries and I am grateful to him for welcoming me in his research group and letting me learn and grow through those years. I also want to thank Prof. Alexey Yamilov and Prof. Frédéric Leblond for accepting to read and comment the results of my efforts.

I want to acknowledge all the people closely or remotely involved in the completion of this thesis. This include Guofeng Yan, Olga Skorobogata, Andrey Markov and Hang Qu. I also extend my thanks to all the people in the office or in the lab for the day-to-day pleasant moments. I cannot forget the meticulous technical assistance of Evgueni Babian and Yves Leblanc. I tried to learn as much as possible from the many fruitful discussions we had.

I must also thank the Fonds de Recherche du Québec en Nature et Technologie and the Natural Sciences and Engineering Research Council of Canada who, by their repeated trust and generous financial support, made this research possible.

Finally, I dedicate this work to my family. First, to my parents who raised me in an atmosphere of questioning and pursuit of knowledge. To my brother and sisters for their unconditional support and motivation. Last but not least, to my lovely wife who, by her kindness, caring and compassion, pushed me to excel myself.

RÉSUMÉ

Dans le spectre électromagnétique, la bande des térahertz (THz) est située entre les micro-ondes et l'infrarouge. Le système de spectroscopie térahertz dans le domaine du temps (THz-SDT) permet d'extraire directement le champ électrique multifréquentiel. Déjà, plusieurs applications avantageuses ont été trouvées pour l'imagerie et la spectroscopie THz, et ce dans divers domaines. Cependant, malgré le potentiel que recèle les THz, plusieurs défis doivent être relevés pour faciliter sa généralisation. Dans cette thèse, nous suggérons des solutions nouvelles à deux problèmes et nous présentons une implémentation d'un système d'imagerie THz 3D, connu sous le nom de tomographie assistée par ordinateur.

Premièrement, la manipulation du faisceau THz est difficile. Afin de remédier à cela, nous explorons deux types de guides d'onde en mousse : la mousse de polystyrène et la mousse de soie. La mousse de polystyrène est utilisée comme gaine pour le guide d'onde THz à deux fils métalliques. Nous montrons que les pertes additionnelles dues à la gaine de mousse sont négligeables par rapport à l'avantage d'avoir une encapsulation robuste et hermétique du guide d'onde. Pour la mousse de soie, nous montrons que les pertes sont un ordre de grandeur inférieures à celles de la soie solide. La mousse de soie a l'avantage d'être biocompatible pour des applications biomédicales ou agroalimentaires.

Deuxièmement, l'acquisition de l'impulsion THz prend beaucoup de temps. La composante la plus lente dans un système THz-SDT est la ligne à délai optique. Nous implémentons une ligne à délai rotative qui est capable de réduire significativement le temps d'acquisition total. De plus, nous présentons des applications nouvelles pour les THz. Ces applications étaient auparavant impossibles en raison, justement, du long temps d'acquisition. Spécifiquement, nous observons, en temps réel, les processus d'évaporation de liquides transparents, l'application et le séchage de la peinture aérosol opaque, ainsi que la détection et l'évaluation de l'épaisseur d'objets mobiles.

Troisièmement, nous implémentons un système d'imagerie THz 3D de tomographie assistée par ordinateur. Le système THz-SDT permet d'imager sur plusieurs fréquences et d'extraire l'indice de réfraction complexe d'un échantillon. Cependant, lors de l'implémentation d'un système d'imagerie THz 3D de tomographie assistée par ordinateur, plusieurs défis s'imposent, le principal étant le long temps d'acquisition. Ici, nous présentons un début d'implémentation d'un tel système. Nous discutons de plusieurs problèmes et nous présentons des solutions pour certains.

ABSTRACT

In the electromagnetic spectrum, the terahertz (THz) frequency band is located between the microwave and the infrared. The pulsed THz time-domain spectroscopy (THz-TDS) system allows direct access to the THz electric field and its multifrequency nature. Already, THz imaging and spectroscopy have been applied to many different fields. Despite all the interest and potential, there are still some hurdles impeding its generalized use. In this thesis, we suggest novel solutions to two issues and we present an implementation of a THz 3D imaging modality known as computed tomography.

First, the handling of the THz beam is difficult. To overcome this, we explore two kinds of foam waveguides : polystyrene foam and silk foam. We use the polystyrene foam as a cladding for the THz two-wire waveguide. We show that the additional losses are offset by the mechanically robust and hermetical foam encapsulation. As for the silk foam, we show that the losses are one order of magnitude lower than those of solid silk. Here, the silk foam has the advantage of being biocompatible for biomedical and agro-alimentary applications.

Second, the acquisition of the THz pulse is time-consuming. The slowest component in a regular THz-TDS system is the linear optical delay line. We implement a fast rotary delay line that is able to significantly reduce the overall time acquisition. Additionally, we present novel applications for THz. These applications were not possible before, because of the long time acquisition. Specifically, we observe, in real time, the evaporation of transparent liquids, the spray painting process, as well as the detection and thickness evaluation of moving objects.

Third, we implement a THz 3D computed tomography imaging system. The THz-TDS allows multifrequency imaging and direct extraction of the complex refractive index. However, when doing computed tomography imaging on a THz-TDS system, several challenges arise, the main one being the time acquisition. Here, we present an early implementation of such a system. We discuss several issues and we present solutions to some.

TABLE OF CONTENTS

ACKNOWLEDGEMENTS	iii
RÉSUMÉ	iv
ABSTRACT	v
TABLE OF CONTENTS	vi
LIST OF TABLES	ix
LIST OF FIGURES	x
LIST OF ACRONYMS AND SYMBOLS	xv
INTRODUCTION	1
CHAPTER 1 TERAHERTZ TIME-DOMAIN SPECTROSCOPY SYSTEM	5
1.1 Generation and detection of THz	5
1.2 THz beam steering and focusing	7
1.3 Time resolved detection with an optical delay line	9
1.4 Data acquisition and lock-in amplifier	9
1.5 THz pulse in time and frequency domains	11
1.6 Refractive index and losses	12
CHAPTER 2 HYBRID METAL-DIELECTRIC THz WAVEGUIDES	14
2.1 THz waveguides literature overview	14
2.1.1 Metallic waveguide	14
2.1.2 Dielectric waveguides	15
2.2 Two-wire waveguides with polystyrene foam cladding	15
2.2.1 Bulk polystyrene foam	17
2.2.2 Two-wire waveguide with a polystyrene foam cladding	18
CHAPTER 3 ARTICLE 1 : SILK FOAM TERAHERTZ WAVEGUIDES	21
3.1 Authors	21
3.2 Abstract	21
3.3 Introduction	22

3.4	Characterization of silk foams	24
3.4.1	Characterization of silk foam porosity	24
3.4.2	Optical characterization of silk foams in the THz spectral range	26
3.4.3	Intepretation of the cutback measurements	27
3.5	Silk fiber measurement	32
3.5.1	Optical characterization of the silk foam fibers in the THz spectral range	32
3.5.2	Interpretation of the cutback measurements of silk foam fibers	32
3.6	Guidance mechanism in the silk foam fibers	38
3.7	Discussion	40
3.8	Conclusion	41
3.9	Experimental section	42
3.9.1	Purified aqueous silk fibroin solution	42
3.9.2	Silk foams and foam-based fibers	42
3.10	Acknowledgments	43
CHAPTER 4 ARTICLE 2 : TIME RESOLVED DYNAMIC MEASUREMENTS AT THz FREQUENCIES USING A ROTARY OPTICAL DELAY LINE		44
4.1	Authors	44
4.2	Abstract	44
4.3	Introduction	45
4.4	Characterization of the FRLODL	47
4.5	Practical applications of the FRLODL	55
4.5.1	Monitoring of the evaporation process	55
4.5.2	Monitoring of spray painting	55
4.5.3	Detection and thickness evaluation of moving objects	56
4.6	Conclusion	59
4.7	Acknowledgment	60
CHAPTER 5 3D THz COMPUTED TOMOGRAPHY		61
5.1	Principles of 3D CT	61
5.1.1	Radon transform	61
5.1.2	Filtered back-projection reconstruction	62
5.2	3D CT in THz	64
5.3	Implementation of THz CT imaging	65
5.3.1	Technical issues	65
5.3.2	Fast acquisition and correction for THz CT imaging	65
5.4	Reconstruction	66

CHAPTER 6 GENERAL DISCUSSION	70
6.1 Polyurethane foam as a THz waveguide	70
6.2 Silk foam terahertz waveguides	72
6.3 Trigger for fast rotary delay line	72
6.4 Waveguide and rotary delay line in a THz CT imaging system	74
CONCLUSION	75
REFERENCES	77

LIST OF TABLES

Table 3.1	Porosity of the silk bulk foams.	26
Table 4.1	Thickness of LDPE samples assessed with micrometer and FRLODL.	59

LIST OF FIGURES

Figure 1.1	THz-TDS Setup	5
Figure 1.2	(a) Optical excitation of the THz-PCA. (b) Generation and (c) detection of THz with the THz-PCA.	6
Figure 1.3	Geometrical construction using specular reflection law on a parabolic function. The rays emitted from the focal point are collimated parallel to the axis of symmetry.	8
Figure 1.4	(a)-(b) Time domain pulse. (c) Normalized amplitude spectrum. The dotted lines correspond to absorption in the water molecule [37, 38]. (d) Unwrapped phase spectrum.	11
Figure 2.1	(a) Time-domain electric field. (b) Transmission spectra. (c) Unwrapped phase relative to the reference. Each color represents a particular length of polystyrene foam.	16
Figure 2.2	(a) Effective refractive index. The mean value is indicated by the red dashed line. (b) Extinction losses and numerical fit with a fourth-order polynomial (dashed green) and Lorentzian function (dashed red). The sum of the two is plotted in blue.	18
Figure 2.3	Photograph of the two-wire ABS 3D-printed holder (a) with and (b) without polystyrene foam. (c) Magnification of the metal coupler used also as an aperture. (d) Holder with two wires between two apertures inside the THz-TDS system.	19
Figure 2.4	Time-domain electric field of (a) two-wire waveguide embedded in polystyrene foam, (b) two wires only, and (c) ABS holder only. (d) Transmission spectra of the corresponding electric field.	20
Figure 3.1	(a) A typical sample of a silk foam; (b) transverse cut of a silk foam sample; SEM images of the foam crosssection taken with different magnifications in the vicinity of the sample center: (c) large scale view, (d) vicinity of the center, (e,f) exactly at the center.	25
Figure 3.2	Schematic of the THz setup used for characterization of the bulk foam samples.	27
Figure 3.3	Cutback measurements using bulk foam sample presented in Figure 3.1. (a) Unnormalized transmission spectra, (b) unwrapped phases (relative to the reference), (c) foam absorption losses, (d) foam refractive index.	29

Figure 3.4	Time traces corresponding to the cutback measurements of a bulk foam sample of Figure 3.1. (a) Solid lines – experimentally measured time traces, dotted lines – analytical fit Equation 3.7 using Equations 3.2, 3.3 for the foam refractive index and bulk losses obtained by interpreting spectral transmission data at low frequencies. (b) Solid lines – experimentally measured time traces, dotted lines – analytical fit Equation 3.7 using Equation 3.9, 3.10 for the foam refractive index and bulk losses obtained by minimizing the difference between experimental and theoretical time traces.	31
Figure 3.5	Schematic of the THz setup used for characterization of the foam-based fibers. Insets – 5 mm-diameter fiber crosssection, silk foam fiber mounted inside of a setup.	33
Figure 3.6	Cutback measurements using 5 mm-diameter silk foam fiber. (a) Un-normalized transmission spectra, (b) unwrapped phases (relative to the 2.04 cm-long fiber reference). Extracted (c) fiber absorption losses, (d) modal effective refractive index.	35
Figure 3.7	Time traces corresponding to the cutback measurements of 5 mm-diameter silk foam fibers. (a) Solid lines – experimentally measured time traces, dotted lines – analytical fit (Equation 3.14) using 3.15 and 3.16 for the core material refractive index and bulk losses. (b) Optical properties of the fundamental HE_{11} mode of a silk foam fiber.	37
Figure 3.8	(a) Longitudinal flux distribution in the fundamental HE_{11} mode of a step-index silk foam fiber at various frequencies. Black circle marks the core/cladding interface. Top row – fiber diameter is 1.5 mm. Bottom row – fiber diameter is 4.0 mm. (b) Propagation loss of HE_{11} mode normalized by the bulk absorption loss of the core material. (c) Group velocity dispersion of the HE_{11} mode.	39
Figure 4.1	(a) The schematic of an individual rotating blade consisting of two curvilinear reflectors [27]; (b) The time delay of the FRLODL; (c) The optical setup of the FRLODL in Zemax.	48

Figure 4.2	(a-d) The outgoing beam captured by the detector screen at the rotation angle θ of 5, 10, 20 and 30°. The rotation angle θ is defined in Figure 4.1 (a). Particularly, when the rotation angle is 5°, the incoming beam is cut by the edge of the curvilinear reflector, thus resulting in an incomplete reflection. (e) The RMS radius of the outgoing beam at different rotation angles; (f) The centroid position of the outgoing beam in OX and OY direction on the detector screen as a function of the rotation angle.	50
Figure 4.3	(a-d) The outgoing beams reflected by a rotary disk with 1 μm average roughness of the reflector surfaces for rotation angles 5, 10, 20 and 30° respectively. The rotation angle θ is defined in Figure 4.1 (a). (e) The RMS radius of the outgoing beam at different rotation angles. (f) The centroid position of the outgoing beam in OX and OY direction on the detector screen as a function of the rotation angle.	51
Figure 4.4	The experimental setup. Inset shows the FRLODL disk with its four manufactured blades. Notice the parallel incoming and outgoing optical beams at different rotation angles.	52
Figure 4.5	Characterization of the FRLODL. (a) THz time traces for different delays between the emitter and detector lines and (b) the deduced positions (in ms) of the main peak knowing the delay (in ps). (c) The averaged and normalized pulses for different rotation speeds and (d) the corresponding power spectra. The arrow points to the noise level of the FRLODL measurements. The "Linear" curve corresponds to the measurement with a standard micropositioning linear stage and is added for comparison of the positions of the water absorption lines. (e) The signal-to-noise ratio for different rotation speeds and (f) the dynamic range as a function of the number of averaging.	54
Figure 4.6	The evaporation process measured with the FRLODL. (a) The normalized electric field amplitude of the main THz peak as a function of time for water, acetone and methanol. Inset: longer time scale. (b) The time traces (top) and spectra (bottom) for the evaporation of acetone.	56

Figure 4.7	Monitoring of the painting process using the FRLODL. (a) The normalized amplitude (top blue) and time shift (bottom red) of the main THz peak along time. (b) The THz time traces during spraying (top) and drying (bottom). (c) The normalized power spectra evolution along time. (d) The averaged pulse before and after the painting process.	57
Figure 4.8	The detection of fast moving LDPE samples. (a) Experimental setup. The THz beam is collimated and the LDPE sample drops vertically. (b) The detected time delay by the passing of the LDPE samples. Inset: zoom at the passing of the 14.72 mm sample and (c) the corresponding time traces. (d) The inaccuracy of the temporal position of the peak when using the motor trigger (top) or the photodiode trigger (bottom).	58
Figure 5.1	Principles of Radon transform. (a) Line integral projection at angle ϕ along x' , performed in the direction of the y' axis. (b) Collection of all the projections results in a sinogram $g(x', \phi)$	63
Figure 5.2	Visual explanation of the Fourier slice theorem.	63
Figure 5.3	Removal of high frequencies in the acquired data. (a) Electric field and (b) spectrum of one THz pulse before (blue) and after (red) the correction.	67
Figure 5.4	Superimposition of multiple pulses. A hundred electric fields (a) before and (b) after the correction.	67
Figure 5.5	Fully corrected pulse. (a) Electric field and (b) spectrum.	67
Figure 5.6	The configuration of the LDPE rod with three holes in the THz-TDS system in (a) a top (b) and lateral view. Note that the beam waist is not at scale compared to the size of the holes.	68
Figure 5.7	(a)-(d) Sinograms at different frequencies : (a) 0.25, (b) 0.50, (c) 0.75 and (d) 1 THz. (e)-(f) Corresponding filtered back-projections : (e) 0.25, (f) 0.50, (g) 0.75 and (h) 1 THz. (i)-(k) Averaged sinograms on the (i) 0.25 – 0.50 THz band, (j) 0.50 – 0.75 THz band and (k) 0.75 – 1 THz band. Corresponding filtered back-projections : (l) 0.25 – 0.50 THz band, (m) 0.50 – 0.75 THz band and (n) 0.75 – 1 THz band. (o) Simulated LDPE rod with three holes and (p) its Radon transform	69
Figure 6.1	(a) Photograph of the polyurethane foam. Diameter is 95 mm. (b) Time-domain electric field of the cutback measurement for different lengths of polyurethane foam. The reference corresponds to the measurement in an empty THz-TDS system. It has been multiplied by 0.25 for clarity. (c) Transmission spectra. (d) Unwrapped phase relative to reference.	71

Figure 6.2	(a) Refractive index and (b) losses of polyurethane foam.	71
Figure 6.3	SEM images of the fiber silk foam. (a) Low magnification revealing the macrostructure. The dotted line indicates the position of the tape used to hold the sample. (b) Periphery of the sample. (c) Higher magnifications showing the flat walls and (d) the circular holes.	73
Figure 6.4	Generation of the trigger based on the electrical output of the rotation motor. (a) Raw electrical output of the motor. (b) Saturated signal. (c) Electronic logical counters stage.	74

LIST OF ACRONYMS AND SYMBOLS

CNC	Computer numerical control
CT	Computed tomography
DR	Dynamic range
FRLODL	Fast rotary linear optical delay line
LDPE	Low density polyethylene
LT-GaAs	Low-temperature GaAs
THz	Terahertz
THz-TDS	THz time-domain spectroscopy
THz-PCA	THz photoconductive antenna
SEM	Scanning electron microscopy
SNR	Signal-to-noise ratio

INTRODUCTION

In the electromagnetic spectrum, the terahertz ($1 \text{ THz} = 10^{12} \text{ Hz}$) region lies from 0.1 to 10 THz, corresponding to wavelengths of 3 mm to $30 \mu\text{m}$. At the junction of the microwave and the infrared, the THz frequency band has a number of relevant, sometimes unique, applications. However, for many years, the scientific community lacked the technological tools for the manipulation of THz. Even generation and detection were problematic. Nowadays, the research has been able to overcome many hurdles, but some challenges remain.

Throughout time, the pulsed THz time-domain spectroscopy (THz-TDS) technology has emerged as a leader in the field. The THz pulse contains multiple frequencies and the time-domain sampling provides direct access to the THz electric field. Thereby, the complex spectroscopic nature of a sample can be fully experimentally extracted. A two or three dimensional mapping of the complex refractive index can then lead to hyperspectral imaging.

THz imaging and spectroscopy have well recognized unique benefits. First, the THz are able to penetrate, with different attenuation levels, most dielectric materials, for example polymers and fabrics. Second, unlike microwaves, the THz wavelength is sufficiently small to provide high resolution images. Third, various solid and gaseous materials show unique signatures in the THz band, leading to identification spectroscopy. Fourth, the THz induce no harmful photoionization in biological tissue. Therefore, it is not surprising to see that THz imaging and spectroscopy have been applied to many different fields.

In the biomedical domain [1], THz waves were used to detect various kinds of cancers : breast [2], skin [3] and oral [4] cancer for example. More fundamentally, THz have been used to probe biological molecules, such as proteins [5] or sugars [6]. As for pharmaceutical applications, tablet coating thickness [7] and crystallinity of pharmaceutical materials [8] were quantified using THz.

Similarly, several applications have been found for industrial applications of THz [9]. For polymers, in-line thickness evaluation [10], identification of degradation products [11] and in-line monitoring of compounding process [12] were demonstrated. In the food industry, detection of contaminants [13], homogeneity and moisture quantification of mixtures [14] have been performed. Failure in semiconductors was determined [15] and petroleum products were distinguished with THz [16]. In the paper industry, THz-TDS provides a non-contact method to quantify the composition and thickness of paper products during their production [17, 18].

Other relevant technological applications of THz include art conservation [19], detection

and identification of explosives [20] and non-contact inspection of space shuttle foam insulation [21]. Intensive research is also conducted in the field of THz communications, where higher carrier frequencies hold the potential to allow faster transmission of huge data [22].

Challenges and objectives

Despite all the interest and potential, there are still many hurdles impeding a wide use of THz imaging and spectroscopy. In this thesis, we suggest novel solutions to two problems : the THz beam handling and the acquisition time. Lastly, we present an implementation of a 3D imaging modality known as Computed tomography.

First, the handling of the THz beam is difficult and alignment is time-consuming. Besides, practical operation often requires a variable distance between the THz emitter and the sample. To address this, intensive research activity has been carried out to develop THz waveguides. In this thesis, we present two foam structures to guide the THz wave : two metal wires in a polystyrene foam and a silk foam. As we will see, the silk foam has the added advantage of being biocompatible.

Second, in a THz-TDS, a time-domain sampling is performed in order to reconstruct the THz pulse. This is usually done with a micrometer linear stage in which a displacement step corresponds to a time step. This operation is time-consuming, often in the minute scale. This is not compatible with probing of in-line industrial processes for example. Therefore, it is highly desirable to have a faster way to acquire the THz pulse. In this thesis, we implement a fast rotary delay line that is able, as we will see, to reduce significantly the time acquisition.

Third, THz has the ability to penetrate various materials. 3D imaging along with full 3D mapping of the complex refractive index is therefore possible and has been previously performed by others. The last work done within the framework of this thesis is a practical implementation of a THz 3D Computed tomography system.

The objectives of this thesis are:

1. To overcome the THz beam handling issue by investigating the dielectric foam waveguides,
2. To reduce significantly the acquisition time by implementing a fast rotary delay line in a THz-TDS system,
3. To perform 3D imaging by implementing a Computed tomography system based on THz-TDS.

Structure of the thesis

This thesis is divided in six chapters. As we cover relatively different subjects, the literature review is introduced when necessary.

In Chapter 1, we introduce the basics behind a regular THz-TDS system. We do not intend to exhaustively present all the possible configurations, but we rather focus on the system that we used within this thesis.

Then, in Chapter 2, we present a first solution for the beam handling problem in the form of a hybrid metal-dielectric foam waveguide. The chapter begins with a brief overview of the previous work on two kinds of THz waveguide : the metal and the dielectric waveguides. Then, we present our novel solution : a two-wire waveguide in a polystyrene foam. Notably, Section 2.2 summarizes part 3 of our published paper in the *Journal of the Optical Society of America B* [23].

Chapter 3 is a transcript of our full paper published in *Advanced Optical Materials* [24]. Again, it addresses the beam handling issue with another kind of dielectric foam : the silk foam. As we will see, this rather exotic biological material has the potential to guide the THz for the biomedical and agro-alimentary industries. As such, to the best of our knowledge, it is the first biocompatible material used for THz waveguiding. This publication has been highlighted by *Nature photonics* in its *Research Highlights* [25].

In Chapter 4, we address the second issue of time acquisition. The chapter is a full transcript of our paper published in *IEEE Transactions on Terahertz Science and Technology* [26]. In it, we present an implementation of a fast rotary delay line. The regular linear delay line is very slow and, mechanically, a rotary movement can reach higher speeds. In a previous work, our group presented a theoretical analysis of several classes of curvilinear surfaces that provide, in reflection, linear delay line with the rotation angle [27]. In this chapter, we fabricate and present full characterization of such a surface. Additionally, we present new practical applications for the THz, that were before impossible because of the long time acquisition.

In Chapter 5, we present the latest work performed within this thesis : the implementation of a 3D Computed tomography system. First, we describe a method for image reconstruction. Then, we implement it with a THz-TDS system. The work presented in this chapter is still in progress. For that reason, results are not final. Although some issues are addressed in this thesis, some others remain and, for them, we point out potential solutions.

Finally, in Chapter 6, we discuss complementary details about the previous chapters. For completeness, we add experimental characterization of polyurethane foam for waveguide applications. The preliminary results were not sufficiently encouraging for further analysis. We

also comment on several points that were not covered in the publications of Chapters 3 and 4. Specifically, we present scanning electron microscopy imaging of the fiber silk foam. We also comment the trigger operation for the fast rotary delay line. Lastly, we discuss about the integration of the waveguides and the rotary delay line in a THz computed tomography system.

CHAPTER 1 TERAHERTZ TIME-DOMAIN SPECTROSCOPY SYSTEM

In this chapter, we present the basics underlying a standard THz-TDS system. We do not intend to present all the possible configurations, but rather the principles underlying the one used within this thesis.

In Figure 1.1, we depict a standard THz-TDS system. As in a pump-probe scheme, an optical beam coming from an ultrafast femtosecond laser is divided in two paths: emission and detection lines. On one path, a retroreflector mounted on a translation stage is placed to add relative time delay. A voltage is supplied on the THz emitter, while a current is recorded on the THz detector.

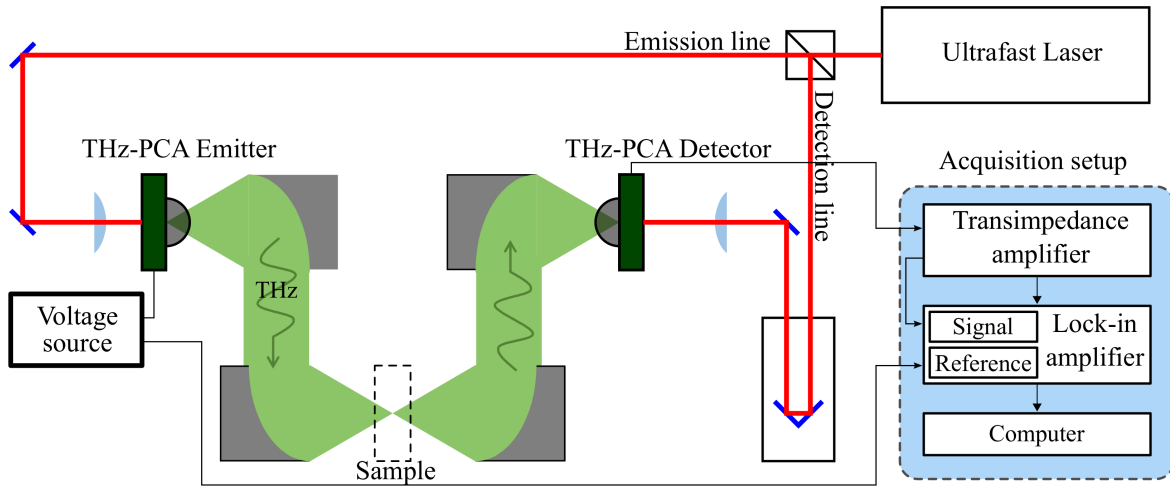


Figure 1.1 THz-TDS Setup

1.1 Generation and detection of THz

The generation and detection of the THz wave are based on Auston switches [28], also known as THz photoconductive antenna (THz-PCA). A THz-PCA is an optical switch that generates free carriers when excited by a photon with sufficient energy and time duration. More specifically, it is formed by metal electrodes on a semiconductor substrate, typically low-temperature GaAs (LT-GaAs). The optical beam is focused on the gap between the two electrodes (Figure 1.2 (a)). The same THz-PCA can be used for both generation and detection of THz.

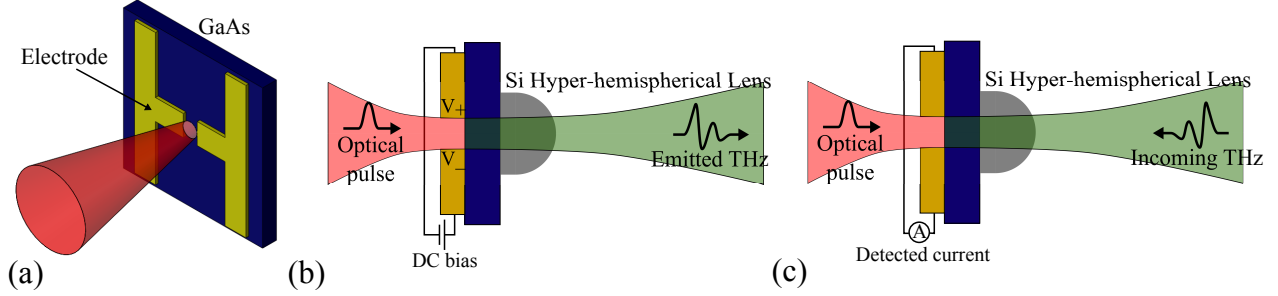


Figure 1.2 (a) Optical excitation of the THz-PCA. (b) Generation and (c) detection of THz with the THz-PCA.

In an emitting configuration, a DC bias electric field is applied between the electrodes (Figure 1.2 (b)). Free carriers¹ are generated by photons with energy larger than the semiconductor bandgap. Then, they are accelerated by the DC field while simultaneously being trapped in defects in the semiconductor structure. This rapid rise and fall of the transient photocurrent gives rise to a subpicosecond pulse of electromagnetic radiation. In frequency, this corresponds to the THz region.

The radiation source can be modelled as a Hertzian dipole antenna in which the dipole size (gap between electrodes) is much smaller than the wavelength [30]. It is possible to show that:

$$E_{\text{THz}} \propto \frac{dJ_{\text{PC}}(t)}{dt} \quad (1.1)$$

where E_{THz} is the radiated THz electric field and J_{PC} is the generated transient photocurrent. The latter can be modeled with the classical Drude-Lorentz model, which is beyond the scope of this thesis [30–32]. In this model, under saturation, it can be shown that the emitted THz field increases proportionally with the amplitude of the DC field and the intensity of the optical pulse.

Placed in a detecting configuration, the THz-PCA follows the same principles. Again, the focused optical beam generates free carriers. However, this time, they are accelerated by the incoming THz electric field. This will result on the generation of a net photocurrent between the electrodes (Figure 1.2 (c)). This current depends on both the THz electric field and the

¹Free carriers can either be electrons or holes. However, in the generally used LT-GaAs, electrons are the main carriers [29].

transient surface conductivity $\sigma_s(t)$ as the following convolution [30]:

$$J(t) = \int_{-\infty}^t \sigma_s(t-t') E_{\text{THz}}(t') dt' \quad (1.2)$$

that can be transformed by the use of the convolution theorem as:

$$\tilde{J}(\nu) = \tilde{\sigma}_s(\nu) \tilde{E}_{\text{THz}}(\nu) \quad (1.3)$$

where the \sim denotes the Fourier transform. These last equations show two things. First, the measured photocurrent is the incoming THz frequency filtered by the surface conductivity, meaning that the detected bandwidth is limited by the semiconductor conductive properties. Second, the photocurrent is directly proportional to the THz electric field. Thus, time resolved detection of the photocurrent leads to complete resolution of the electric field waveform, both in amplitude and phase.

1.2 THz beam steering and focusing

At the output of the emitter THz-PCA, the THz is not radiated in a narrow beam but rather like a point-source, because the wavelength is much longer than the dipole size. Furthermore, the dielectric interface between air and the substrate implies that the energy radiated into the substrate is higher than the energy radiated into free space by a factor of the substrate dielectric constant ϵ_r . Since for typical LT-GaAs substrate, $\epsilon_r \approx 12$, most of the energy is reflected back in the substrate [30, 33].

Thus, commonly, a hyper-hemispherical lens is placed just at the tip of the antenna substrate. High resistivity silicon is used for this because its refractive index (3.418) is very close to the GaAs semiconductor in the THz band [34]. Therefore, this type of lens has two advantages. First, it limits the internal reflections. Second, it confines the outgoing beam in a 34° diverging cone [30]².

To further collimate the beam, it is necessary to place optical components, such as an off-axis parabolic mirror. Recall the general equation for a parabola in cartesian coordinates:

$$y = ax^2 + bx + c \quad (1.4)$$

²This value comes from ray optics calculations. See p.67-68 of [30] for a detailed demonstration

The vertex P and the focus F are at the $[x, y]$ coordinates:

$$P = \left[-\frac{b}{2a}, \frac{-\Delta}{4a} \right] \quad F = \left[-\frac{b}{2a}, \frac{1-\Delta}{4a} \right] \quad (1.5)$$

where $\Delta = b^2 - 4ac$ is the discriminant of the quadratic equation. The axis of symmetry is defined as the line passing P and F . Using the law of reflection, it is possible to show that a ray parallel to the axis of symmetry is directed toward the focal point and, conversely, a ray emitted from the focal point is reflected parallel to the axis of symmetry (Figure 1.3).

In a off-axis geometry, only a small part of the parabolic shape is used (bold in Figure 1.3). Thus, it becomes possible to position the THz antenna at F . The parabolic mirror can be used both to collimate a divergent beam coming from the emitter and focus a parallel beam into the detector. In practice, a tridimensional paraboloid with the same properties is used. The mirror has to be coated with a metal. A study showed that gold, silver or aluminium coatings reflects equally THz waves [35]. The skin depth, which is the penetration depth of an electromagnetic radiation inside a conductor, is 65 nm at 1 THz and because regular optical mirrors have coatings in the micrometer range, they can be used to reflect THz. Moreover, the roughness of optical mirrors are more than sufficient for THz. Indeed, 1 THz corresponds to 300 μm and optical mirrors have generally roughness ~ 10 nm. We mention that flat mirrors can also be used to reflect the beam without modifying its shape.

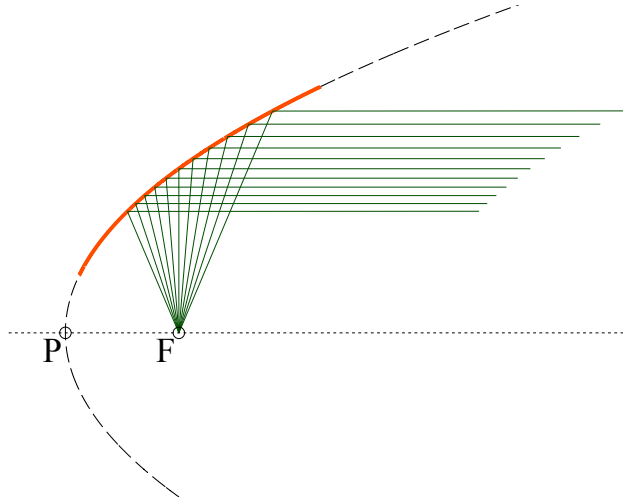


Figure 1.3 Geometrical construction using specular reflection law on a parabolic function. The rays emitted from the focal point are collimated parallel to the axis of symmetry.

1.3 Time resolved detection with an optical delay line

To temporally resolve the photocurrent, an optical delay line is used. Indeed, the detector measures a photocurrent only when the optical pulse excites photocarriers in the detecting THz-PCA. Essentially, the width of the excitation femtosecond pulse can be considered very small compared to the picosecond THz pulse. Therefore, by adding relative delay in one of the arm, it is possible to resolve the THz pulse.

In such a measurement, the independent variable is the position z of the delay line. It can be converted to time domain by :

$$t = \frac{2 \cdot z}{c} \quad (1.6)$$

where the 2 expresses the fact that the optical beam travels twice the distance z because it is reflected back.

Then, the complex spectrum can be obtained by taking the Fourier transform of the pulse along time. By the properties of the Fourier transform, the maximal frequency f_{\max} and the frequency resolution δf are linked to time domain increment δt and the total scanned temporal delay Δt :

$$\begin{aligned} f_{\max} &= \frac{1}{2 \cdot \delta t} = \frac{c}{4 \cdot \delta z} \\ \delta f &= \frac{1}{\Delta t} = \frac{c}{2 \cdot \Delta z} \end{aligned} \quad (1.7)$$

with δz and Δz are the corresponding spatial resolution and total spatial delay. For example, a 10 μm scanning step for a displacement of 20 mm yields a spectrum with a maximal frequency of 7.5 THz and a resolution of 7.5 GHz. Typically, the delay line is instructed to move to each step, where the amplitude and phase of the THz pulse are recorded by the means explained in Section 1.4. Yet, this process can take several seconds, sometimes minutes. In Chapter 4, we present a rotary delay line that reduces considerably the time acquisition.

1.4 Data acquisition and lock-in amplifier

Inset of Figure 1.1 depicts a scheme for the data acquisition. The output of the detection THz-PCA is a current. The first step is to preamplify this current and convert it to measurable voltage. This is performed using a transimpedance amplifier. Then, typically, a lock-in amplifier is used to selectively amplify the useful data without amplifying the noise. As this is

a crucial step for the understanding of the data collection, we present hereafter a conceptual and mathematical understanding of the process [36].

The lock-in amplifier is based on the use a reference frequency that is directly linked to the desired signal. Typically, in a THz-TDS system, one can either chop the optical beam or supply a AC voltage to the emission THz-PCA with known frequency and phase, respectively f and ϕ_r . The idea is to detect the signal at the same values.

Let us denote the reference as V_R and the desired signal V_S . By supposing that the two frequencies of these signals are the same, we can write them as:

$$\begin{aligned} V_s &= K \cos(2\pi ft + \phi_S) \\ V_r &= \cos(2\pi ft + \phi_R) \end{aligned} \quad (1.8)$$

where K and ϕ_S are the desired amplitude and phase of the signal that we wish to obtain. These two voltages are multiplied with each other by the use of a mixer to yield:

$$\begin{aligned} V_M &= K \cos(2\pi ft + \phi_S) \cos(2\pi ft + \phi_r) \\ &= 1/2K[\cos(\phi_S - \phi_R) + \cos(2\pi 2ft + \phi_S + \phi_R)] \end{aligned} \quad (1.9)$$

In this last equation, we see two frequencies. To extract only the DC component, a low-pass filter is applied:

$$V = \frac{1}{2}K \cos(\phi_S - \phi_R) \quad (1.10)$$

However, in general, $\phi_S \neq \phi_R$ and so it is not possible to retrieve both phase and amplitude with this simple approach. This is why a better dual-phase lock-in amplifying is used. There, two mixers are used, the second one having a π phase added to the reference signal. Then, the same procedure is applied to get a complex number such as:

$$\begin{aligned} V_x &= \frac{1}{2}K \cos(\phi_S - \phi_R) \\ V_y &= \frac{1}{2}K \sin(\phi_S - \phi_R) \\ V &= V_x + iV_y = K e^{i(\phi_S - \phi_R)} \end{aligned} \quad (1.11)$$

From this, the amplitude and phase can be extracted with the usual equations:

$$\begin{aligned} K &= \sqrt{V_x^2 + V_y^2} \\ \phi_S &= \arctan\left(\frac{V_y}{V_x}\right) + \phi_R \end{aligned} \quad (1.12)$$

1.5 THz pulse in time and frequency domains

We present in Figure 1.4 (a) and (b) a typical measured pulse. To obtain the spectrum, we simply compute the Fourier transform. Note that the result will be complex, leading to amplitude and phase spectra that we present in Figure 1.4 (c) and (d) respectively. In Figure 1.4 (c), the vertical dotted lines indicate the positions of the water absorption peaks [37, 38]. They are caused by rotational transitions in the water molecule. In some applications, it is desirable to have a clean smooth spectrum. Therefore, a common way to remove the humidity in the air is to enclose the THz beam in a box and purge it with nitrogen. We will perform this a few times during this thesis.

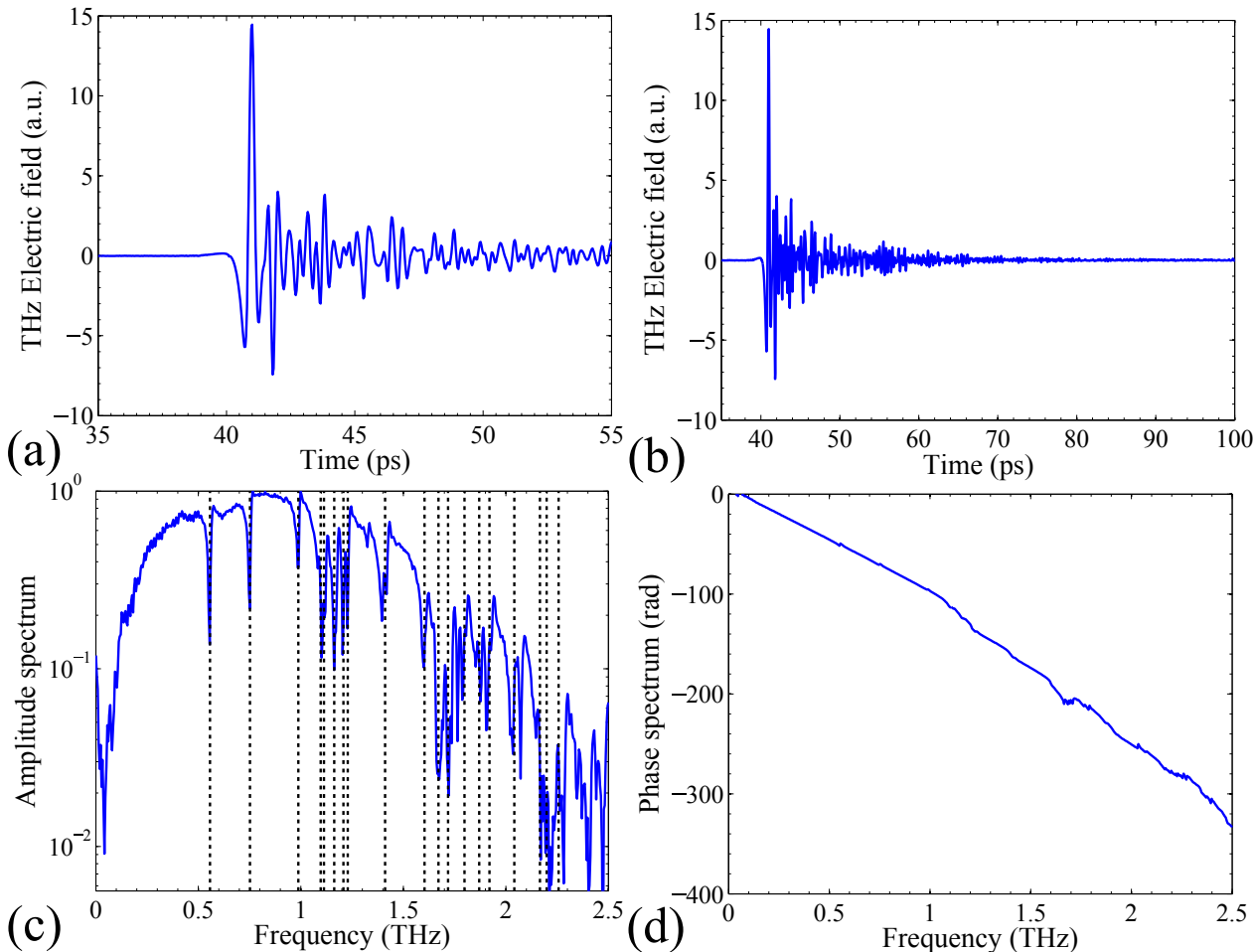


Figure 1.4 (a)-(b) Time domain pulse. (c) Normalized amplitude spectrum. The dotted lines correspond to absorption in the water molecule [37, 38]. (d) Unwrapped phase spectrum.

1.6 Refractive index and losses

When a THz pulse is transmitted through a given sample, it undergoes several modifications. In this section, we present a transmission characterization method from the recorded THz pulse. Let $E_0(\omega)$ be the reference THz pulse. Then, the transmitted pulse $E_t(\omega)$ can be written as

$$E_t(\omega) = E_0(\omega) \cdot t_0 \cdot e^{-\alpha(\omega)L} \cdot e^{i\phi(\omega)} \quad (1.13)$$

L is the length of the sample and $\alpha(\omega)$ is the extinction coefficient. For THz applications, we generally express it in cm^{-1} . Note that this extinction coefficient is given here for amplitude extinction. t_0 is the Fresnel transmission coefficient that needs to be written as two successive transmissions, from the air to the sample and from the sample to the air. Recall that the Fresnel transmission from media 1 to media 2 is

$$t_{1 \rightarrow 2} = \frac{2n_1}{n_1 + n_2} \quad (1.14)$$

where n_1 and n_2 are the refractive indices of the media 1 and 2 respectively. In our case, media 1 is the air ($n_1 = 1$) and media 2 is the sample ($n_2 = n(\omega)$). Therefore, for two successive transmissions, we can write

$$t_0 = t_{\text{air} \rightarrow \text{sample}} \cdot t_{\text{sample} \rightarrow \text{air}} = \frac{4n(\omega)}{(n(\omega) + 1)^2} \quad (1.15)$$

In Equation 1.13, $\phi(\omega)$ corresponds to the additional phase of the sample subtracted by the air phase, because the sample replaces the air.

$$\phi(\omega) = -\frac{\omega}{c}(n(\omega) - 1)L \quad (1.16)$$

Therefore, the refractive index and the extinction coefficient can be retrieved from the refer-

ence and sample measurements with the following formulas :

$$\begin{aligned} n(\omega) &= 1 + \frac{c_0}{\omega L} \angle \left(\frac{E_t(\omega)}{E_0(\omega)} \right) \\ \alpha(\omega) &= -\frac{1}{L} \ln \left[\frac{(n(\omega) + 1)^2}{4n(\omega)} \left| \frac{E_t(\omega)}{E_0(\omega)} \right| \right] \end{aligned} \quad (1.17)$$

CHAPTER 2 HYBRID METAL-DIELECTRIC THz WAVEGUIDES

In this chapter, we address the THz beam handling issue. We begin by presenting a brief literature overview of two classes of THz waveguides : the metallic and the dielectric waveguides. Then, we present a strategy to overcome the handling issue in the particular case of the two-wire waveguide. It uses a polystyrene foam.

Section 2.2 of this chapter is a summary of our work published in section 3 of [23], entitled *Hybrid metal wire-dielectric terahertz waveguides: challenges and opportunities* and authored by A. Markov, H. Guerboukha and M. Skorobogatiy. It is an invited review paper that contains also new experimental demonstrations. Here, we summarized the relevant new experimental demonstrations as it was part of the work done under this thesis. In particular, for section 3 of [23], the work included the experimental investigations, the data analysis and the writing.

2.1 THz waveguides literature overview

2.1.1 Metallic waveguide

The metallic waveguides were developed by ideas coming from the microwaves. The simplest example is the hollow circular or rectangular metallic waveguide [39, 40]. There, the pulse suffer most from Ohmic losses ($\alpha \sim 0.7 \text{ cm}^{-1}$ at 1 THz.). Moreover, the higher frequencies traveling faster leads to a significant group velocity dispersion (negative chirp). For example, a 1 ps stretches to ~ 70 ps after 2.4 cm propagation in a 240 μm diameter stainless steel waveguide [39].

Similarly, parallel plate metallic waveguides raised attention [41, 42]. In this geometry, two metallic plates separated by $\sim 100 \mu\text{m}$ are able to support a single TEM mode. They feature virtually no dispersion and very low losses. For example, in [41], an incoming 0.22 ps pulse broadens to 0.39 ps after 25 cm propagation. In the same paper, by using very thin copper strips (100 μm thick), the authors were able to bend the waveguide.

The so-called Sommerfeld waveguide [43, 44] was also considered. It is a simple wire that supports a radially-polarized plasmon mode. There, the mode has a very large evanescent field extending far in the air cladding. It shows very low losses and low group velocity dispersion. However, the coupling is rather difficult in the radially-polarized mode, because the available THz emitters are generally linearly polarized. Plus, the field is mainly present in the air cladding surrounding the wire, leading to very high bending losses.

Based on the same approach, two-wire waveguide was also proposed [45]. There, two wires are put close to each other with a constant spatial separation. Compared to the Sommerfeld waveguide, this design has the advantage of confining the mode in the region between the wires. As a consequence, the coupling with a linear polarized input beam is greatly enhanced and losses due to bending are reduced. However, as with the Sommerfeld waveguide, it is not practical. In Section 2.2, we present a solution that we developed to overcome the handling problem of the two-wire waveguide.

2.1.2 Dielectric waveguides

A second class of THz waveguides is the dielectric waveguides. The majority of them are fabricated with polymers, which tend to be the lowest absorbing materials in the THz. Nevertheless, standard total internal reflection is not possible, because those losses are still quite high. Several strategies have been employed to overcome the loss problem.

The simplest dielectric waveguides are the small core subwavelength-diameter fibers [46–49]. Like the Sommerfeld waveguide, they feature a highly evanescent mode in a air cladding surrounding, this time, a polymer wire. The fundamental mode is linearly polarized, leading to high coupling efficiencies. Yet, because of the highly delocalized nature of the mode, it suffers from high bending losses and the handling is still problematic.

Large hollow-core multi-mode tube waveguides were also demonstrated. There, the light is confined inside the air core by different cladding reflection mechanisms : photonic crystal reflection [50], attenuation total internal reflection [51], Fabry-Pérot reflection [52] or Bragg reflection [53–55]. Although very low losses were demonstrated, each type of waveguide has its own disadvantages that cause handling of the THz beam impractical (for a more in-depth discussion see [56, 57]).

2.2 Two-wire waveguides with polystyrene foam cladding

In the previous section, we summarized different strategies for guiding the THz. A common factor to all these waveguides is the fraction of power guided in the air. In fact, gases are the lowest absorbing materials for the THz. In what follows, we use a highly porous polystyrene foam to get an important fraction of the power in the gaseous phase.

In fact, there is an increased interest in using hybrid waveguides that borrows advantages from both the metal and the dielectric waveguides [23, 58–63]. In previous work, our group proposed to use a porous dielectric support for the two-wire waveguide [60]. The idea is to use the advantage of the stable linearly polarized fundamental mode of the two-wire waveguide

in a dielectric highly porous matrix. The porous structure is then able to overcome the absorption problem of the dielectric waveguides. In this section, we present the two-wire waveguide structure in a polystyrene foam [23].

As discussed earlier, a large fraction of power guided inside a dry low-loss gas is desired. Polymer foams are inherently highly porous. They are formed by a matrix of solid polymer in which open or closed cell gas regions are uniformly distributed. Characterization of polystyrene foam [64] showed very low refractive index (1.017 – 1.022 from 0.1 to 4 THz) and very low losses (under 1.5 cm^{-1} below 4 THz). Likewise, polymethacrylimide foams showed the same of kind of behavior in the THz range [65].

This impressive performance is explained within the effective medium approximation, which describes propagation of electromagnetic waves in composite materials made of subwavelength particles or inclusions implanted into a host material [35-36]. Thus, even if *solid* polystyrene is known to have a refractive index of 1.6 in the THz, highly porous polystyrene *foam* has a refractive index closer to the gas inside the pores.

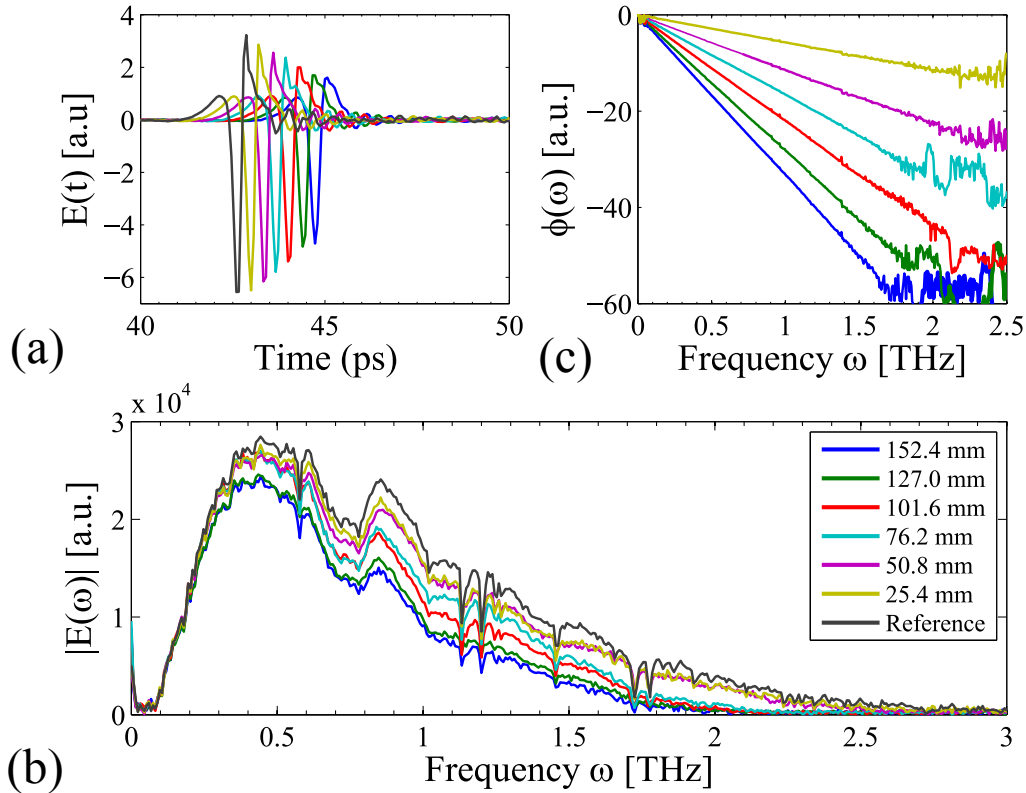


Figure 2.1 (a) Time-domain electric field. (b) Transmission spectra. (c) Unwrapped phase relative to the reference. Each color represents a particular length of polystyrene foam.

Ultimately, the THz extinction coefficient is influenced by the nature of the solid material (absorption loss), but also by the foam microstructure (scattering loss). In particular, scattering losses become important when the scatterer (gas pocket) size becomes comparable to the wavelength. We note also that careful consideration should be given to the type of gas (blowing agent) used in the foam fabrication, as it can exhibit undesirable absorptions in the THz.

In what follows, we first present bulk polystyrene foam characterization in the THz. As we will see, we find a low refractive index and very low losses. Then, we use this foam to demonstrate it as a cladding for the two-wire waveguide.

2.2.1 Bulk polystyrene foam

THz characterization of a polystyrene foam sample is conducted in a regular THz-TDS system. Six slabs of polystyrene foam from McMaster-Carr (item 9335K11) of dimensions $60 \times 60 \times 25.4$ mm are placed in the path of the THz beam. Then, we conduct a series of seven measurements of the THz electric field by successively removing the six slabs. The seventh measurement is the reference and corresponds to the pulse propagation through the empty system. In Figure 2.1, we present time-domain electric fields and the corresponding transmission spectra and unwrapped phases.

To extract the refractive index and the extinction coefficient, we consider the transmission of the THz electric field through the polystyrene foam sample and we use equations presented in Section 1.6 to calculate the refractive index and the losses (Figure 2.2).

Consistent with prior studies, the foam refractive index is essentially constant in the whole spectrum and the extinction coefficient is very low ($<0.15 \text{ cm}^{-1}$ below 1.5 THz). Moreover, we see that the frequency dependence of the extinction coefficient can be well fitted with a fourth order polynomial and a Lorentzian :

$$\alpha_f[\text{cm}^{-1}] = a \cdot \nu^4 + b \cdot \nu^2 + c + d \cdot \left(\frac{\Gamma}{\Gamma^2 + (\nu - \nu_r)^2} \right)$$

$$a = 0.01276; \quad b = 0.03337; \quad c = 0.00409; \quad d = 0.01779; \quad (2.1)$$

$$\Gamma = 0.1219 \text{ [THz]}; \quad \nu_r = 0.7974[\text{THz}],$$

ν is in THz.

There, the fourth-order polynomial describes the joint contribution of scattering and material absorption losses. In the vicinity of 0.8 THz, we observe a broad resonance that we fit with a Lorentzian and that we attribute to the spectral signature of the gas blowing agent filling the

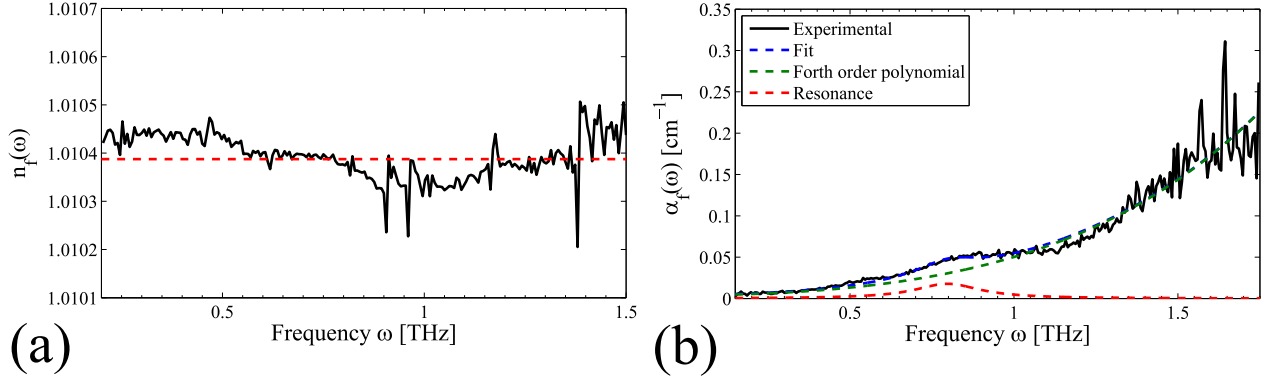


Figure 2.2 (a) Effective refractive index. The mean value is indicated by the red dashed line. (b) Extinction losses and numerical fit with a fourth-order polynomial (dashed green) and Lorentzian function (dashed red). The sum of the two is plotted in blue.

pores. In Figure 2.2 (b), the fourth-order polynomial is plotted in green and the resonance in red. The sum of those two terms is plotted in blue and fits well with the experimental data in black.

2.2.2 Two-wire waveguide with a polystyrene foam cladding

Encouraged by the positive results in a bulk polystyrene foam, we now turn to encapsulation of the two-wire waveguide. For this, we perform a comparative study of the THz pulse transmission through a 14 cm long two-wire waveguide with and without the polystyrene foam. First, we design and, using a 3D printer, manufacture an acrylonitrile butadiene styrene (ABS) holder (Figure 2.3). The copper wires are then wound on four metallic barrels that also control the $750 \mu\text{m}$ interwire separation. The holder is then placed in the THz-TDS system between two 3 mm apertures.

Three types of measurements are performed. In the first measurement, we firmly press two polystyrene slabs of $6 \times 20 \times 130$ mm against the wires. In the second measurement, we carefully remove the foam cladding and in the third, without touching the holder, we cut the wires. This last measurement effectively measures the level of stray light in the system.

The measured pulse traces and their spectra are presented in Figure 2.4. First, we confirm that the two-wire waveguide effectively guides the THz pulse, by noting that the pulse transmitted with the waveguide (two-wire) is four times stronger than the stray pulse (holder only). Also, we note that in this configuration, the pulse bandwidth is limited to ~ 0.6 THz with a maximal frequency of ~ 0.4 THz. This maximal frequency correlates with the interwire

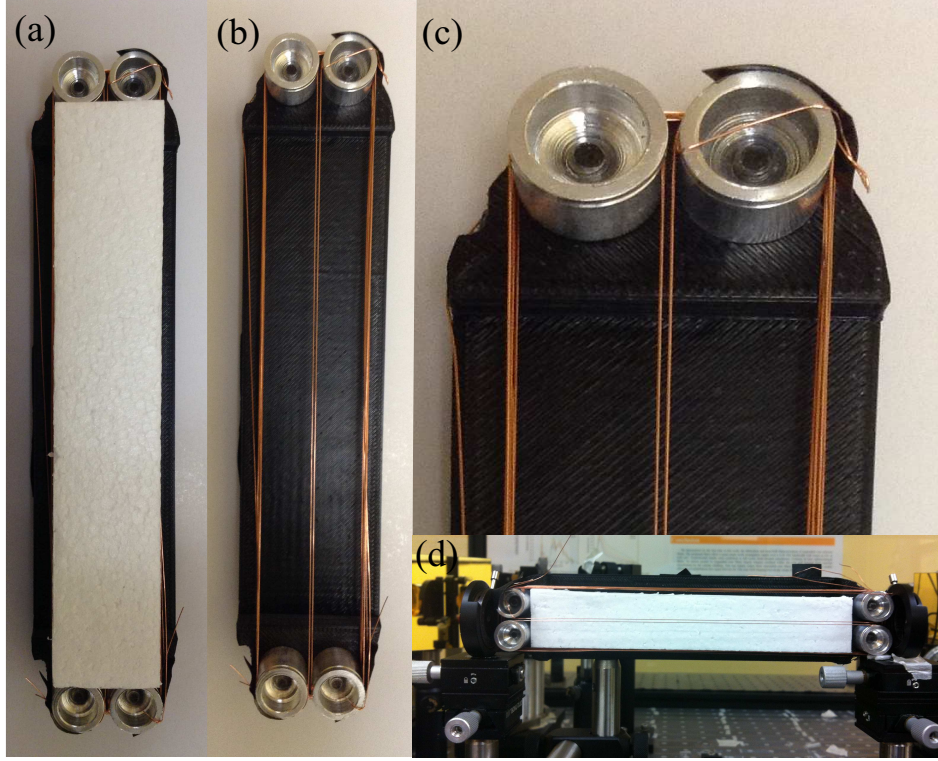


Figure 2.3 Photograph of the two-wire ABS 3D-printed holder (a) with and (b) without polystyrene foam. (c) Magnification of the metal coupler used also as an aperture. (d) Holder with two wires between two apertures inside the THz-TDS system.

distance of ~ 0.75 mm. In the case of the two-wire waveguide, it was well already noted that it is more efficient for the wavelength corresponding to the interwire distance [60].

When adding the foam cladding, the THz pulse undergoes several modifications. Remarkably, the Fourier spectra of the transmitted pulses with and without the foam are quite similar. From the small decrease in intensity, we estimate that the additional loss is $\sim 0.12 \text{ cm}^{-1}$. The pulse experiences a small retardation of $\Delta t = 1.52$ ps, from which we estimate that the average effective modal refractive index is ~ 1.003 , through Equation 2.2.

$$n = \frac{c_0 \Delta t}{L} + 1 \quad (2.2)$$

where L is the length of the waveguide and c_0 the speed of light in vacuum.

From these measurements, we conclude that polystyrene foam can indeed be used as a cladding for the two-wire waveguide. The decrease in waveguide performance is offset by the mechanically robust and hermetical foam encapsulation.

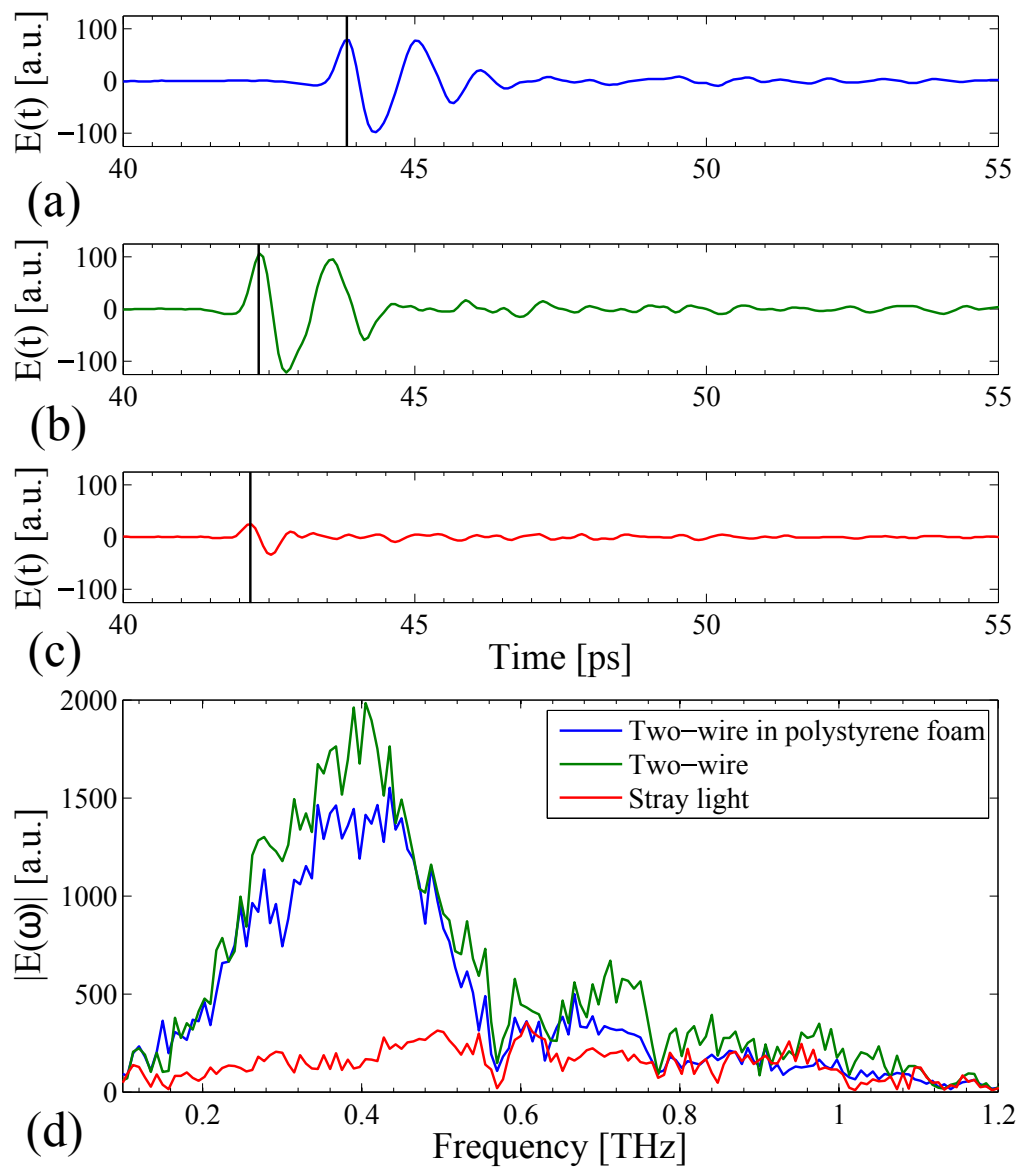


Figure 2.4 Time-domain electric field of (a) two-wire waveguide embedded in polystyrene foam, (b) two wires only, and (c) ABS holder only. (d) Transmission spectra of the corresponding electric field.

CHAPTER 3 ARTICLE 1 : SILK FOAM TERAHERTZ WAVEGUIDES

In this chapter, we continue on addressing the THz beam handling issue. We transcript a manuscript published in *Advanced Optical Materials* [24]. In the previous chapter, we saw different strategies to develop THz waveguides. Then, we presented a polystyrene foam to encapsulate the two-wire waveguide. In this chapter, we explore a novel kind of biological foam material : the silk foam. As we will see, we demonstrate its ability to guide THz waves with low losses and dispersion. This publication was highlighted by *Nature Photonics* in its *Research Highlights* [25].

3.1 Authors

Hichem Guerboukha¹, Guofeng Yan², Olga Skorobogata³ and Maksim Skorobogatiy¹

1. *Department of Engineering Physics, Ecole Polytechnique de Montréal, H3C 3A7, Montreal, Quebec, Canada*
2. *Centre for Optical and Electromagnetic Research, State Key Laboratory of Modern Optical Instrumentation, Zhejiang University, Hangzhou 310058, China*
3. *Department of Anatomy and Cell Biology, McGill University, H3A 0G4, Montreal, Quebec, Canada*

3.2 Abstract

Fabrication and characterization in the THz frequency range of silk foams and silk foam-based waveguides using lyophilisation and casting techniques are reported. The lack of biocompatible and biofriendly waveguides for low-loss, low-dispersion guidance of THz waves motivates the work for applications in remote and stand-off sensing in biomedical and agro-alimentary industries. Silk foams produced are 94% porous. Optical characterization is carried out using THz time-domain spectroscopy. The cutback measurements of foam samples show that the foam refractive index is close to that of air ($n_{foam}^r \approx 1.06$). Silk foam losses scale quadratically with frequency ($\alpha_{foam}[\text{cm}^{-1}] \approx 0.65 + 2.75 \cdot (\nu[\text{THz}])^2$), being one order of magnitude smaller than those of solid silk. As an example of a basic guided wave device, fabrication and optical characterization of 10 cm-long, 5 mm-diameter step-index THz fibers having silk foam in the core and air in the cladding is demonstrated. Cutback measurements confirm that in the mid-THz spectral range, step-index fibers operate effectively in a single mode regime. Effective refractive index and propagation loss at frequencies higher than 0.2 THz

are close to that of a silk foam from which the fiber core is made. At the same time, at these frequencies, modal group velocity dispersion is smaller than $0.2 \text{ ps}/(\text{THz}\cdot\text{cm})$.

3.3 Introduction

Silk is a unique kind of nature protein derived from spiders or worms and it is the strongest natural fiber known to man [66]. *Bombyx mori* silk has excellent mechanical properties, smooth texture and shimmering appearance, so it has been widely used in textile industry over the past five millennia, since its first appearance in Imperial China [67, 68]. Owing to its excellent mechanical and optical properties [69–72], biocompatibility, biodegradability [73, 74] and implant ability [75–77], in recent years, this ancient material has been introduced into biomedical field as a promising biomaterial which opened a new era in the development of optical interfaces and sensors for biomedical applications. Silk material from worm cocoon can be processed into different forms, such as spheres, sponges, fibers [78–80], foams [81] and films [69, 74, 76, 77]. Among these various forms, silk films attracted significant attention for applications in optics and photonics, due to high transparency ($>95\%$) and excellent surface flatness of such films. As a result, a great variety of optical devices has been fabricated using silk films. For example, silk-based diffractive gratings have been fabricated by casting silk solution onto polydimethylsiloxane (PDMS) negative molds. Silk lenses, microlens arrays and 64-phase level 2D diffraction masks were realized using molding technique [69, 82]. Doped fluorescent silk-protein films with a two-dimensional square lattice of air holes were proposed and demonstrated to achieve enhancement in fluorescent emission [83]. Active optical optofluidic pH sensor were realized by chemical modification of the silk protein films with 4-aminobenzoic and by combining the elastomer in a single microfluidic device [84].

Although many silk-based optical devices have been demonstrated, most of them operate in the visible region [69, 70, 76, 82–84]. Recently, the growing demand for THz waveguides and sensors for non-destructive sensing in biomedicine and agriculture is motivating silk material research in THz region. In 2010, split ring resonator-based metamaterials using silk films as a substrate were demonstrated [85]. The authors also showed that silk is semi-transparent in the 0.15–1.5 THz region, having a relatively high loss of $\sim 15 \text{ cm}^{-1}$ at 0.3 THz. In 2012, the same group demonstrated conformal, adhesive, edible food sensors [86] based on the THz metamaterials on silk substrates. By monitoring the antenna resonant response that changes continuously during the food storage, the authors have demonstrated potential of this technology for monitoring changes in the food quality.

To the best of our knowledge, up to date, there were no reports of using silk to fabricate THz waveguides. This, most probably, is related to the high absorption loss of silk in the

THz spectral region. Indeed, bulk absorption loss of silk is almost hundred times larger than the bulk absorption loss of polyethylene ($\sim 0.2 \text{ cm}^{-1}$ at 0.3 THz), which is often used for fabrication of THz fibers [87–89]. At the same time, low-loss, low dispersion waveguides for delivery of THz light is an important enabling technology for stand-off and remote detection using THz waves. Additionally, in biomedical applications, it is desirable to interface THz waveguides directly with the living tissues, which requires the waveguide material to be biocompatible. Hence, using biocompatible materials to guide THz waves can be of significant interest for stand-off and remote sensing in bio-medical, agro-alimentary and other industries.

We note that for applications in the visible spectral range [70], direct writing of silk-based waveguides was recently demonstrated by extrusion of highly concentrated silk solution ($\sim 28 - 30 \text{ wt\%}$) through a $5 \mu\text{m}$ glass deposition nozzle into a methanol-rich reservoir. Unfortunately, this extrusion method cannot be used directly to produce THz fibers as it results in solid core waveguides that show very high absorption loss in THz spectral region. Moreover, extrusion of silk waveguides from aqueous solution can present additional challenge for THz applications due to residual concentration of highly absorbing water molecules in such waveguides.

An alternative fabrication strategy for silk fibers is a direct drawing from a macroscopic preform in a draw tower. Unfortunately, despite the fact that *Bombyx mori* silk has glass transition temperature $\sim 175 \text{ }^\circ\text{C}$ and crystallization temperature $\sim 212 \text{ }^\circ\text{C}$, when heated at a relatively slow rate like 1–20 K/min, the silk melting transition will be obscured by decomposition [90]. It is reported in [91] that at a slow heat rate of 2 K/min the thermal decomposition begins at $\sim 200 \text{ }^\circ\text{C}$, and continues over a broad temperature range, causing mass loss and charring.

The lowest loss materials for THz propagation are dry gases. Therefore, one of the ways to reduce absorption loss is to maximize the fraction of light guided in the gas phase. Foams are inherently highly porous materials featuring both solid and gaseous phases. Polymer foams are used in the industry for various applications including packaging, thermal, acoustic insulation etc. Polystyrene foam was studied at THz frequencies [64, 92]. Very low refractive indices of 1.017 – 1.022 in the 0.1 – 4 THz spectral range were found as well as a small extinction coefficient (smaller than 1.5 cm^{-1} below 4 THz). Polymethacrylimide foam showed the same kind of behavior at THz frequencies [65]. A typical way to produce polystyrene foam is to use pentane gas as a blowing agent to expand the polystyrene beads until they take the shape of a mold. We believe that foam synthesis within a mold is an interesting alternative to fiber drawing technique that is normally used to produce fibers from thermoplastics and glasses. As foam fabrication is not limited to thermoelastic materials, it, thus, opens new

possibilities for development of optical waveguides from advanced materials.

In this paper, we have developed a fabrication method that uses casting from aqueous silk solution in order to produce silk foams through lyophilisation technique. To our knowledge, this is the first time when silk-based waveguides with sub 1 cm^{-1} losses are demonstrated in the mid-THz frequency range. The paper is organized as follows. Section 3.4 presents characterization of the bulk optical properties of silk foams. Section 3.5 describes characterization of the optical properties of THz silk-foam fibers. Section 3.6 presents numerical simulations that detail guidance properties of the silk-foam fibers including propagation loss and modal dispersion. Finally, a detailed comparison between numerical and experimental results is presented.

3.4 Characterization of silk foams

3.4.1 Characterization of silk foam porosity

In Figure 3.1 (a) we present picture of a typical sample of silk foam cast in a conical test tube. Characterization of the foam porosity and its uniformity along the sample length was carried out using cutback technique. Within this method one performs a series of straight cuts through the cylindrical portion of a sample (see Table 1). As each cut section has a simple cylindrical shape, its volume ΔV can be readily evaluated. After each cut, we re-measure the diameter D_2 , the length L , and the weight of the remaining foam sample (see Table 1). From these measurements, and using the value of $\rho_f = 1.35 \text{ g/cm}^3$ for the density of silk fibroin [93], the local filling factor of the cut piece can be evaluated as $V_{\text{fibroin}}/V_{\text{sample}} = \Delta m/(\Delta V \rho_f)V$, where Δm is the mass of a cut section. As shown in Table 1 the silk fibroin filling factor is low $\sim 5 - 6\%$, and slow varying along the sample length, while corresponding porosity (air fraction by volume) of the fabricated foams is higher than 94%.

Moreover, when looking at the silk foam sample crosssection (see Figure 3.1 (b)) we notice highly symmetric patterns formed by the domains of crystallized silk fibroin. Those domains have needle-like shapes extending from the sample center towards the sample periphery. They are multi colored and they shimmer under white light illumination, suggesting thin-film optical interference effects due to silk foam microstructure. Scanning electron microscopy images of the sample crosssection (Figure 3.1 (c-f)) reveal an intricate flaky structure of the silk foams. Namely, the crystallized silk fibroin form crumpled stacks of thin layers that are generally extending from the sample center towards the periphery. The individual silk layers are $\sim 2 \mu\text{m}$ thick and there is $30 - 50 \mu\text{m}$ separation between layers. Additionally, one notices small $1 - 5 \mu\text{m}$ diameter pores piercing the silk layers.

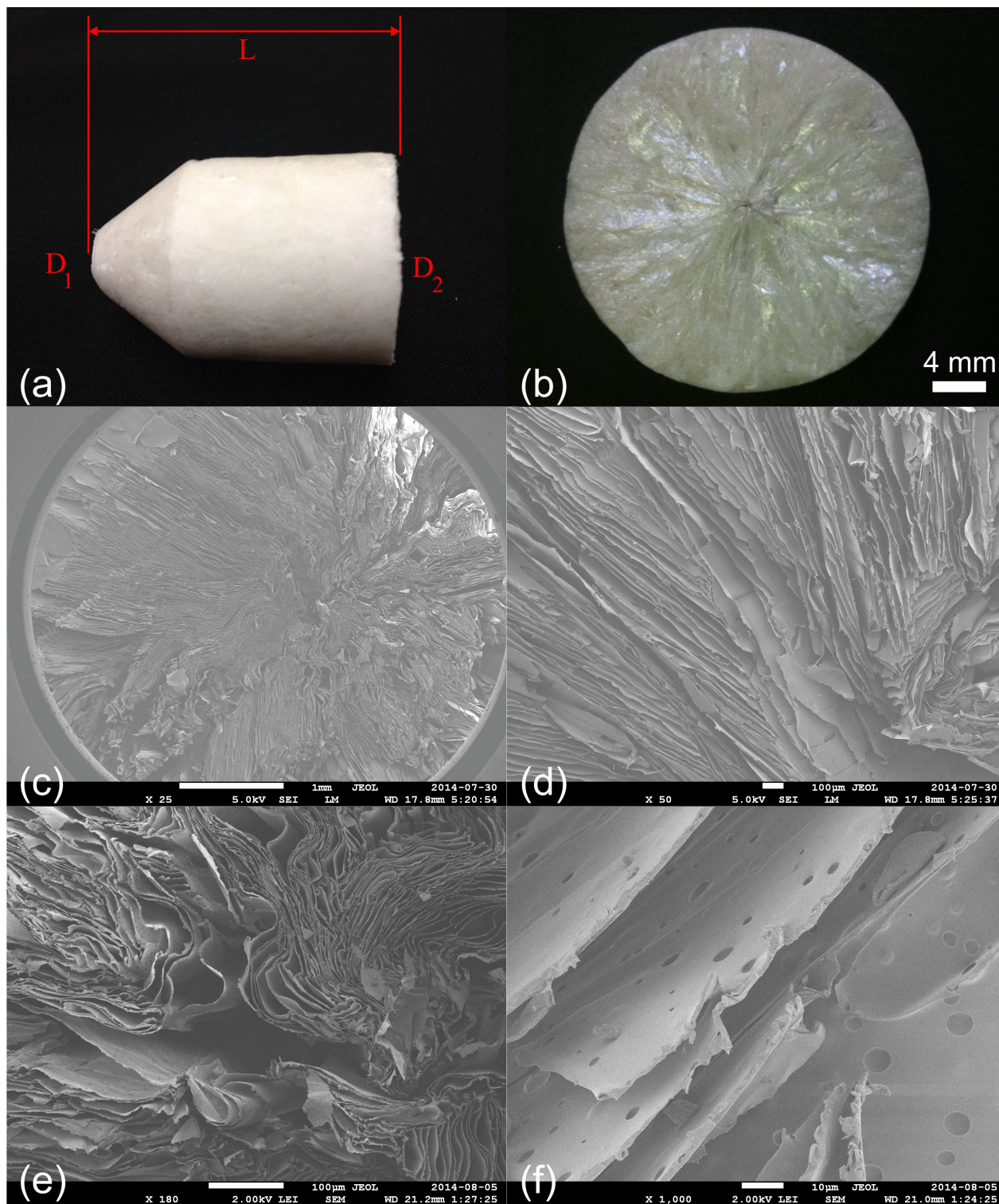






Figure 3.1 (a) A typical sample of a silk foam; (b) transverse cut of a silk foam sample; SEM images of the foam crosssection taken with different magnifications in the vicinity of the sample center: (c) large scale view, (d) vicinity of the center, (e,f) exactly at the center.

Table 3.1 Porosity of the silk bulk foams.

	0	1	2	3
				
Weight [g]	0.989	0.753	0.500	0.360
L [mm]	34.0	27.7	21.0	16.8
D_2 [mm]	24.0	23.8	23.6	23.5
Filling factor ($V_{\text{fibroin}}/V_{\text{sample}}$)		5.0%	5.8%	6.4%

We believe that the radial pattern in Figure 3.1 is caused by the directional dynamics of the freezing process, as well as circular shape of the container. In principle, controlled freezing in judiciously shaped containers could lead to design microstructure alignment that would impact both terahertz wave propagation and its polarization properties.

3.4.2 Optical characterization of silk foams in the THz spectral range

In order to obtain complex refractive index of silk foams, we used THz Time-Domain Spectroscopy (THz-TDS) setup described in [94]. Cutback measurements were performed using conical shaped samples (see Figure 3.1) as obtained directly from the lyophilisation setup. During individual measurements, the small facet of each sample was placed against a semi-closed 3 mm-diameter aperture (A1, Figure 3.2), while the larger diameter end of the sample was placed against an open aperture (A2, Figure 3.2). To ensure consistent measurement conditions, the iris with 3 mm opening was placed at the focal point of a focusing parabolic mirror. The iris was placed on a 3D stage and aligned with the center of the focused beam. The second parabolic mirror (PM2) of 10 cm focal distance was used to collect the transmitted light. The focal point of the second parabolic mirror was aligned with that of the first parabolic mirror (and the center of the aperture) during all experiments. As the size of the collimated beam produced by the THz emitter is $\sim 1 - 2$ cm diameter, and because of the relatively long focal lengths of the two parabolic mirrors, we consider that propagation of light in a focused THz beam is virtually parallel to the sample symmetry axis. Finally, cutback measurements were performed on the two samples by cutting several pieces from each sample and measuring the transmission through the remaining material. The results of these measurements are presented in Figure 3.3 (transmission spectra) and in Figure 3.3 (time traces). Time traces were obtained by averaging over 20, 200 ps-long THz traces. A

typical signal-to-noise ratio in our measurements was ~ 20 dB.

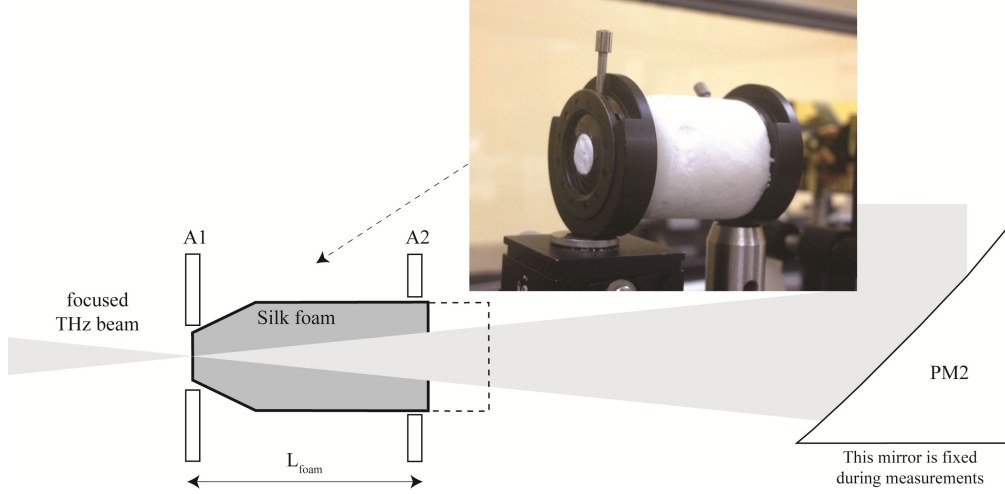


Figure 3.2 Schematic of the THz setup used for characterization of the bulk foam samples.

3.4.3 Intepretation of the cutback measurements

Spectral and phase analysis of cutback data

The real part of the foam effective refractive index $n_{\text{foam}}^r(\omega)$ and the foam extinction coefficient $\alpha_{\text{foam}}(\omega)$ were extracted from the measured cutback data using standard data fitting approach detailed elsewhere (see [94, 95], for example). In our analysis we neglect multiple reflections within the sample (Fabry-Pérot effect) as spectral intensity oscillations associated with this effect are not discernible in the measured data. The complex field transmission coefficient through the sample is then given by:

$$\begin{aligned}
 \frac{E_{\text{foam}}}{E_{\text{ref}}} &= t(\omega)e^{i\phi(\omega)} \\
 t(\omega) &= t_0 \exp(-\alpha(\omega)L_{\text{foam}}) \\
 t_0 &= \frac{4n_{\text{foam}}^r(\omega)}{(n_{\text{foam}}^r(\omega) + 1)^2} \\
 \phi(\omega) &= \phi_{\text{foam}}(\omega) - \phi_{\text{ref}}(\omega) = -\frac{\omega}{c} (n_{\text{foam}}^r - 1) L_{\text{foam}}
 \end{aligned} \tag{3.1}$$

where E_{foam} and E_{ref} are the complex amplitudes of the THz signal with and without a foam sample respectively, and L_{foam} is the length of the foam sample. The transmission coefficient takes into account the loss of intensity due to reflections at the two interfaces between foam and air (coefficient t_0), as well as absorption $\alpha_{\text{foam}}(\omega)$ due to propagation through a lossy

foam sample. Note that in the case of foams $t_0 = 1$ s the foam refractive index is close to 1. Since the complex amplitude could be obtained directly from the THz-TDS measurements, we can, therefore, measure experimentally both the field transmission coefficient $t(\omega)$, and the phase difference $\phi(\omega)$, from which, the real part of the refractive index and the foam extinction coefficient can be calculated using Equations 3.1. In Figure 3.3 (a) we present transmission spectra as measured by the cutback method. If all the spectra are to be used in the interpretation of the cutback results, then our analysis is limited to a narrow frequency range $0.15\text{THz} < \nu < 0.45\text{THz}$, where all the spectra are above the noise level. At these relatively low frequencies, the loss extracted from the cutback data (Figure 3.3 (c)) can be fitted very well with a second order polynomial with respect to frequency:

$$\alpha_{\text{foam}}[\text{cm}^{-1}] = 0.18 + 8.25 \cdot (\nu[\text{THz}])^2 \quad (3.2)$$

In fact, the quadratic scaling of absorption losses is typical for many amorphous materials in the THz range, which is caused by the disorder-induced coupling of radiation into the acoustic phonon modes of the material [96].

In Figure 3.3 (b) we show unwrapped phase relative to the reference (empty system). Fitting of the cutback phase data allows us to extract the effective refractive index, which is shown in Figure 3.3 (d). At low frequencies we find that the refractive index is virtually constant and equals to:

$$n_{\text{foam}}^r = 1.0594 \quad (3.3)$$

From experimental data presented in Figure 3.3 (d), we can also estimate the upper bound for the chromatic dispersion of the bulk foam, which is an important parameter as it allows characterization of the temporal broadening of a THz pulse after propagation over some distance in the foam. To make the estimate, we use Taylor expansion of the foam refractive index in the vicinity of zero frequency, while keeping only two leading terms in order to fit the experimental data presented in Figure 3.3 (d)

$$n_{\text{foam}}^r = n_0 + \beta_1 \omega \quad (3.4)$$

From Equation 3.4 and Figure 3.3 (d) we find that $|\beta_1| < 0.0015 \text{ THz}^{-1}$. The group velocity dispersion of the bulk foam is then:

$$D_{\text{foam}} = \frac{\partial v_g^{-1}}{\partial \omega} = \frac{1}{c} \frac{\partial^2 (n_{\text{foam}}^r(\omega)\omega)}{\partial \omega^2} = \frac{2\beta_1}{c} \quad (3.5)$$

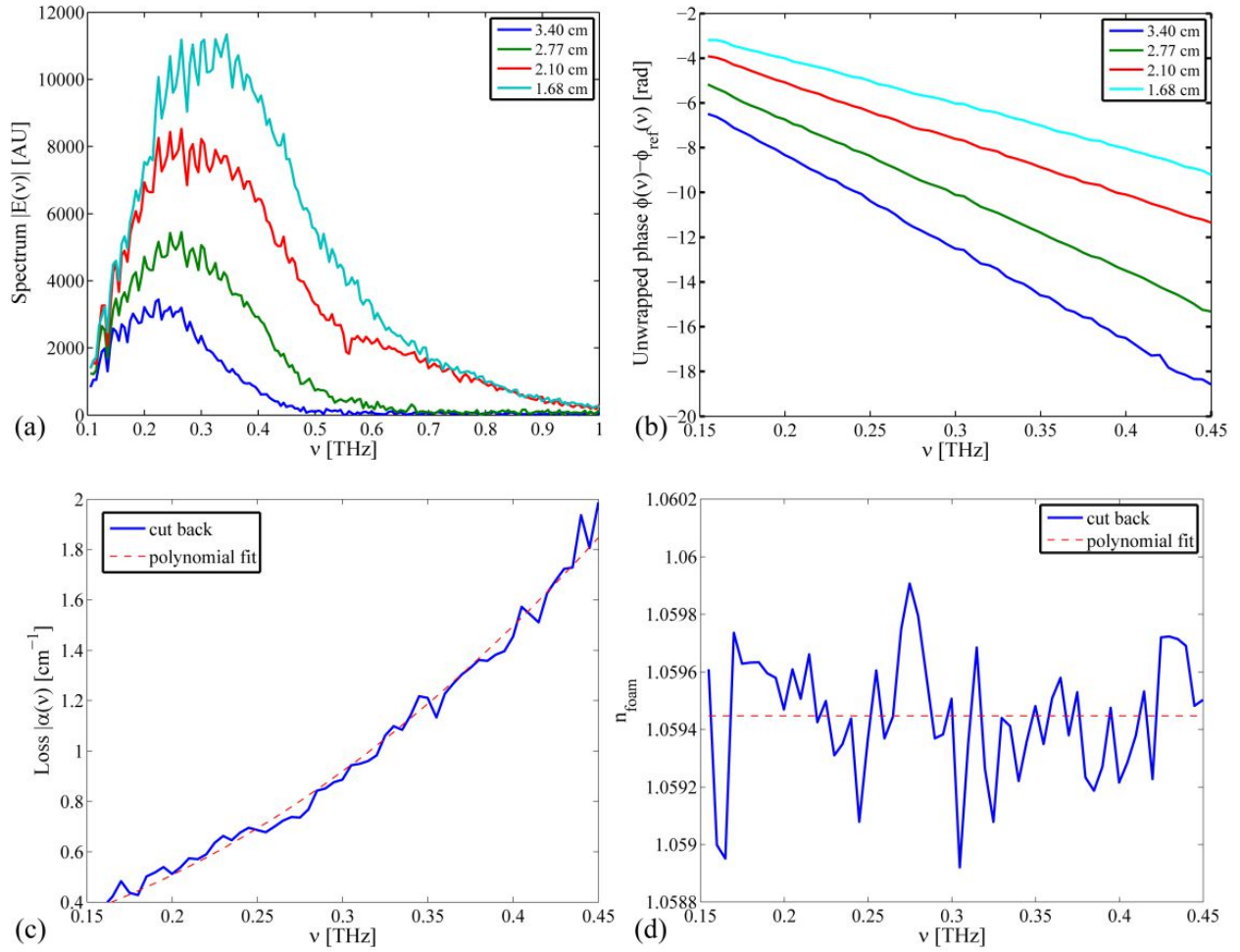


Figure 3.3 Cutback measurements using bulk foam sample presented in Figure 3.1. (a) Un-normalized transmission spectra, (b) unwrapped phases (relative to the reference), (c) foam absorption losses, (d) foam refractive index.

which allows us to estimate the upper limit of the foam group velocity dispersion:

$$|D_{\text{foam}}| < 0.05 \text{ ps}/(\text{THz} \cdot \text{cm}) \quad (3.6)$$

To put this number into perspective, this value of dispersion signifies that a 1 ps-long THz pulse will have to propagate over 20 cm in the bulk foam in order to experience 1 ps temporal broadening. This value of the material dispersion should be compared to the $\sim 1 \text{ ps}/(\text{THz} \cdot \text{cm})$ group velocity dispersion of the fundamental mode of a typical subwavelength plastic fiber, as well as $\sim 0.002 \text{ ps}/(\text{THz} \cdot \text{cm})$ group velocity dispersion of the plasmonic modes in parallel metallic plate waveguides, which are known for their outstanding guidance properties. Note also that the dispersion value is only an upper bound estimate for the bulk foam dispersion, while the actual value could be significantly smaller.

Time trace analysis of the cutback data

We note that polynomial approximations for the foam loss (Equation 3.2) and for the foam refractive index (Equation 3.3) found from the spectral and phase analysis of the cutback data has a limited spectral region of validity. Therefore, when trying to reproduce the measured cutback time traces using Equations 3.2 and 3.3, one does not expect to find a good agreement. Particularly, from Equations 3.1 it follows that the time trace obtained during measurement of a foam sample of length L can be calculated from the reference time trace using a combination of Fourier transform and its inverse:

$$E_{\text{foam}}(t, L_{\text{foam}}) = \text{ifft} \left\{ \text{fft} [E_{\text{ref}}(t)] \exp \left[\frac{-i\omega [n_{\text{foam}}^r(\omega) - 1] L}{c} - \alpha_{\text{foam}}(\omega)L \right] \right\} \quad (3.7)$$

In order to use Equation 3.7 one has to know frequency dependence of the foam refractive index and its losses in the whole THz spectral range. However, polynomial approximations in Equations 3.2, 3.3 were found by fitting experimental data only at low frequencies $0.15 \text{ THz} < \nu < 0.45 \text{ THz}$. Therefore, it is not surprising that using Equation 3.7 together with Equations 3.2 and 3.3 does not result in good correspondence between the measured and predicted time traces (Figure 3.4 (a)). Nevertheless, cut-back measurements are still useful as they provide a consistency check for the values of the foam loss and the foam refractive index, albeit in a limited spectral range.

In order to improve the fit of the pulse traces, we again assume frequency independent foam refractive index n_{foam}^r , as well $\alpha_{\text{foam}} = \alpha_0 + \alpha_1 \cdot \nu^2$ dependence of the foam losses on frequency. Next, we adjust the values of n_{foam}^r , α_0 and α_1 in order to obtain the best possible fit between

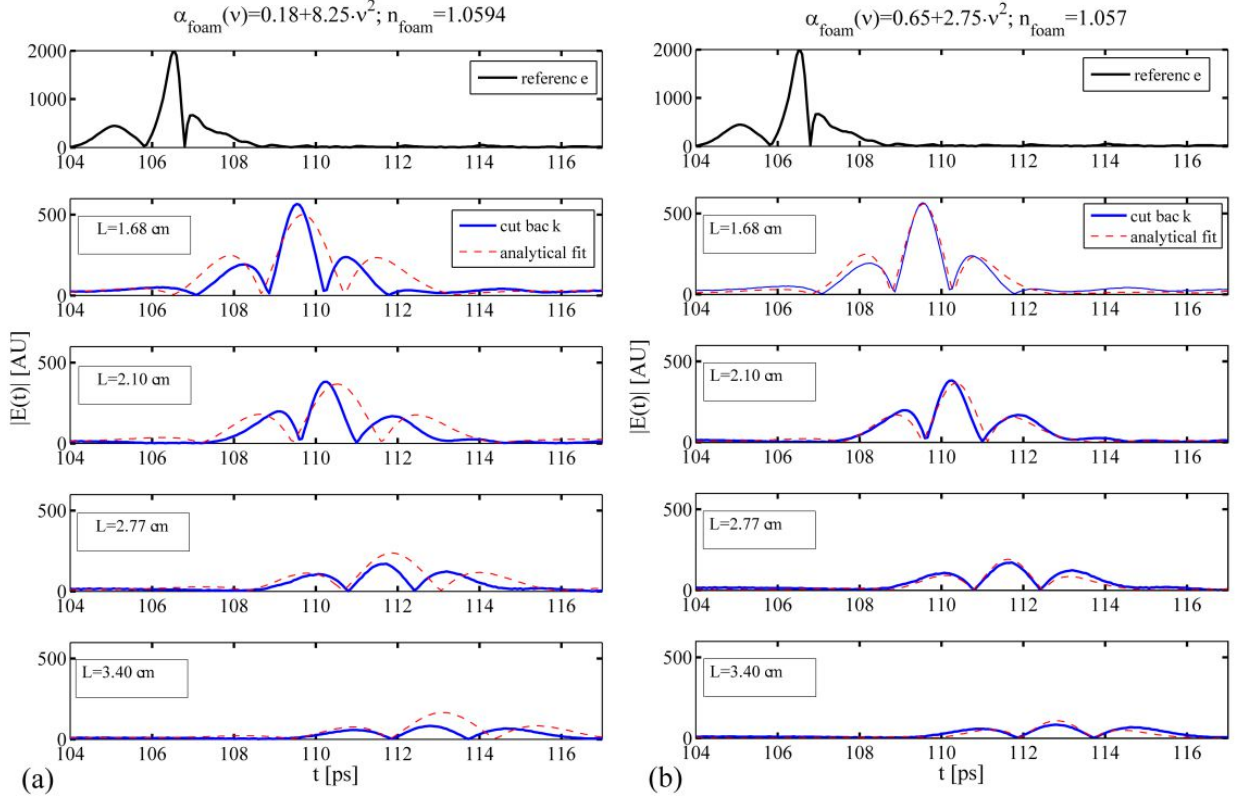


Figure 3.4 Time traces corresponding to the cutback measurements of a bulk foam sample of Figure 3.1. (a) Solid lines – experimentally measured time traces, dotted lines – analytical fit Equation 3.7 using Equations 3.2, 3.3 for the foam refractive index and bulk losses obtained by interpreting spectral transmission data at low frequencies. (b) Solid lines – experimentally measured time traces, dotted lines – analytical fit Equation 3.7 using Equation 3.9, 3.10 for the foam refractive index and bulk losses obtained by minimizing the difference between experimental and theoretical time traces.

the experimental and analytical results. Particularly, we note that n_{foam}^r mostly affects pulse position along the time axis, α_1 has a strong effect on the pulse width, while α_0 mostly affects pulse amplitude. In Figure 3.4 we plot absolute value of the electric field, which is convenient when fitting pulse bandwidth and pulse positions as zeros, maxima and minima of the electric field are easily identifiable in this case. Therefore, by fitting the pulse positions, the pulse widths and the pulse relative amplitudes we can fit very well all the pulse traces assuming the following bulk properties of the silk foams:

$$\alpha_{\text{foam}}[\text{cm}^{-1}] = 0.65 + 2.75 \cdot (\nu[\text{THz}])^2 \quad (3.8)$$

$$n_{\text{foam}}^r = 1.057 \quad (3.9)$$

We note that due to high content of the low-loss dry air in silk foam, the foam bulk absorption is significantly smaller than that of a solid silk. Particularly, from Equations 3.2 and 3.8 we conclude that at 0.3 THz foam absorption loss is $\sim 0.9 \text{ cm}^{-1}$, while that of solid silk is $\sim 15 \text{ cm}^{-1}$. Therefore, the use of silk foams can significantly expand the usefulness of this important biofriendly material in the THz spectral range due to the foam reduced absorption losses.

3.5 Silk fiber measurement

Encouraged by the relatively low losses of silk foams, we then studied the possibility of THz guidance using silk foam-based fibers. The fibers were cast from the purified silk solution using straw molds and lyophilisation technique, thus allowing us to fabricate ~ 10 cm-long silk fibers of 5 mm diameter.

3.5.1 Optical characterization of the silk foam fibers in the THz spectral range

The cutback method was used in order to measure fiber propagation loss and modal effective refractive index. In Figure 3.5, we present schematic of the setup used in our experiments, while in the insets we show a photo of the 5 mm-diameter fiber mounted inside the setup, as well as fiber crosssection. In contrast to the case of bulk foam samples presented in the previous sections, transverse structure of the foam fibers is considerably more uniform, which is clearly related to the difference in dynamics of the lyophilisation process. While the micro-sized crystalline silk domains are still visible on the photographs of fiber crosssections as speckles of colored light, at the same time, a clearly defined pattern of radially aligned domains (as seen in Figure 3.1 (c-f)) is missing in the case of fibers. For optical characterization, the fibers were held straight and aligned with respect to the apertures A1 and A2 that marked the locations of the focal points of the input and output off-axis parabolic mirrors (see Figure 3.5). Reliable and efficient coupling between the THz beam and the fiber was easy to realize as the fiber diameter is somewhat larger than the THz beam diameter of 3 mm.

3.5.2 Interpretation of the cutback measurements of silk foam fibers

Spectral and phase analysis of the cutback data

The modal transmission characteristics are deduced from the cutback data and fitting procedure describe in the literature [42, 94]. In general, the normalized transmission through the

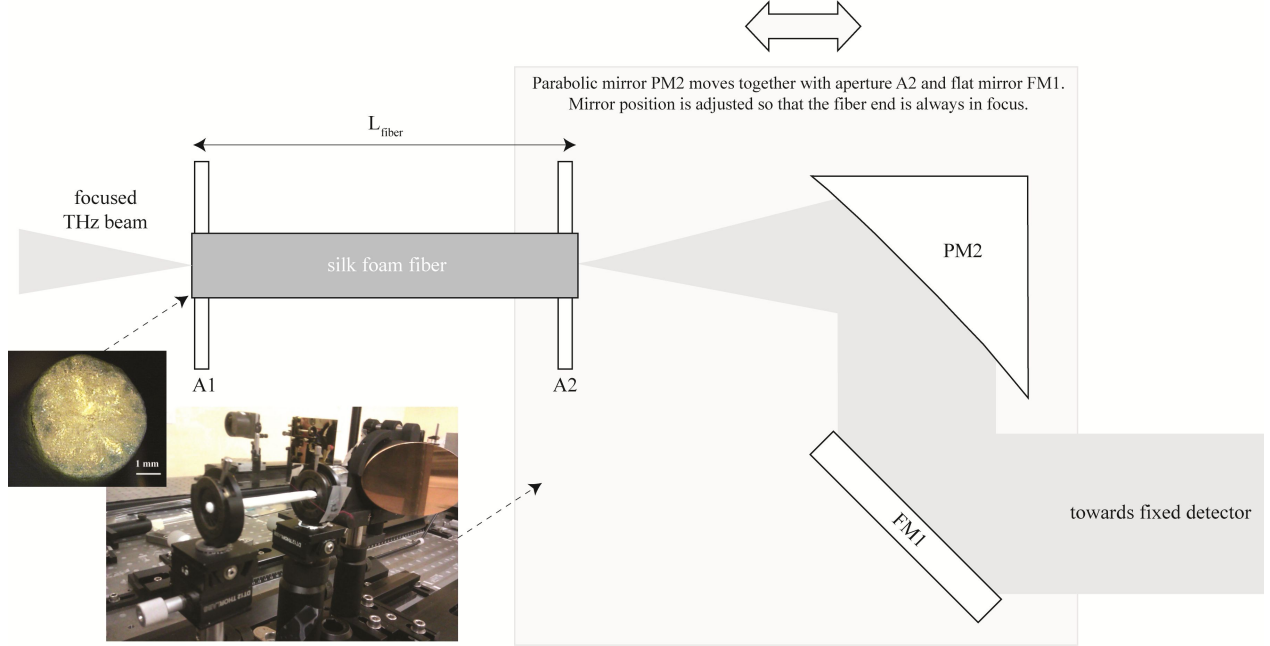


Figure 3.5 Schematic of the THz setup used for characterization of the foam-based fibers. Insets – 5 mm-diameter fiber crosssection, silk foam fiber mounted inside of a setup.

fiber is given by:

$$\frac{E_{\text{mode}}(\omega, L)}{E_{\text{ref}}(\omega, L)} = C_{\text{in}}(\omega)C_{\text{out}}(\omega)e^{i\phi(\omega)}e^{-\alpha_{\text{mode}}(\omega)L} \quad (3.10)$$

$$\phi(\omega) = -\frac{\omega}{c}(n_{\text{mode}}(\omega) - 1)L$$

where E_{mode} is the complex electric field of the propagating mode characterized by the effective refractive index $n_{\text{mode}}(\omega)$ and propagation loss $\alpha_{\text{mode}}(\omega)$. L is the fiber length, E_{ref} is the reference electric field measured without fiber at the position of the coupling plane, while $C_{\text{in}}(\omega)$ and $C_{\text{out}}(\omega)$ are the frequency dependent input and output coupling coefficients. Fiber transmission spectra are presented in Figure 3.6 (a) for four different fiber lengths. If all the spectra are to be used in the interpretation of the cutback results, then our analysis has to be limited to a narrow frequency range $0.2 \text{ THz} < \nu < 0.4 \text{ THz}$ where intensities of all the spectra are above the noise level. At these frequencies, the loss extracted from the cutback data (Figure 3.6 (c)) can be fitted well with a second order polynomial with respect to frequency:

$$\alpha_{\text{mode}}[\text{cm}^{-1}] = 0.035 + 3.1 \cdot (\nu[\text{THz}])^2 \quad (3.11)$$

At higher frequencies, due to modal confinement of the fundamental mode in the fiber core, modal propagation loss is expected to follow closely absorption loss of the core material (silk foam) $\alpha_{\text{mode}} \approx \alpha_{\text{foam}}$. At lower frequencies, modal propagation loss can be, in principle, significantly lower than the foam absorption loss as modal fields have significant presence outside of the fiber core and in the low-loss gaseous cladding. In practice, consistent measurements at lower frequencies are problematic as fiber modes become sensitive to the core surface roughness and various environmental factors that change during sample handling.

In order to extract phase information we use as a reference transmission data for the shortest fiber of length $L_0 = 2.04$ cm. In this case, from Equation 3.10 it follows that the normalized transmission through the fiber of length L can be presented as:

$$\frac{E_{\text{mode}}(\omega, L)}{E_{\text{mode}}(\omega, L_0)} = e^{i\phi(\omega)} \cdot e^{-\alpha_{\text{mode}}(\omega)(L-L_0)} \quad (3.12)$$

$$\phi(\omega) = -\frac{\omega}{c} (n_{\text{mode}}(\omega) - 1) (L - L_0)$$

Using the complex normalized transmission spectra of Equation 3.12, we can then extract modal phase information for different fiber lengths (Figure 3.6 (b)). Extraction of the modal effective refractive index from the unwrapped phase data can be somewhat problematic in the case of guided modes at low frequencies ($\nu < 0.2$ THz as defined in the next section). This is related to the fact that at low frequencies, the intensity of THz source is weak and the data is prone to noise; additionally, modal refractive index vary significantly at low frequencies due to rapid changes in the modal confinement. At higher frequencies, fundamental mode effective refractive index becomes virtually constant and is close to the refractive index of the core material (silk foam). Considering that in the frequency region $0.2 \text{ THz} < \nu < 0.4 \text{ THz}$, modal effective refractive index is constant, analysis of the phase data (Figure 3.6 (d)) gives the following value for the effective refractive index of the core mode:

$$n_{\text{foam}}^r \Big|_{\nu > 0.2 \text{ THz}} = 1.0654 \quad (3.13)$$

Time trace analysis of the cutback data

A complementary method of finding the modal propagation characteristics is to fit directly the measured cutback time traces. In what follows we use as a reference the time trace $E_{\text{fiber}}(t, L_0)$ corresponding to the shortest fiber piece L_0 . Then, the time trace corresponding

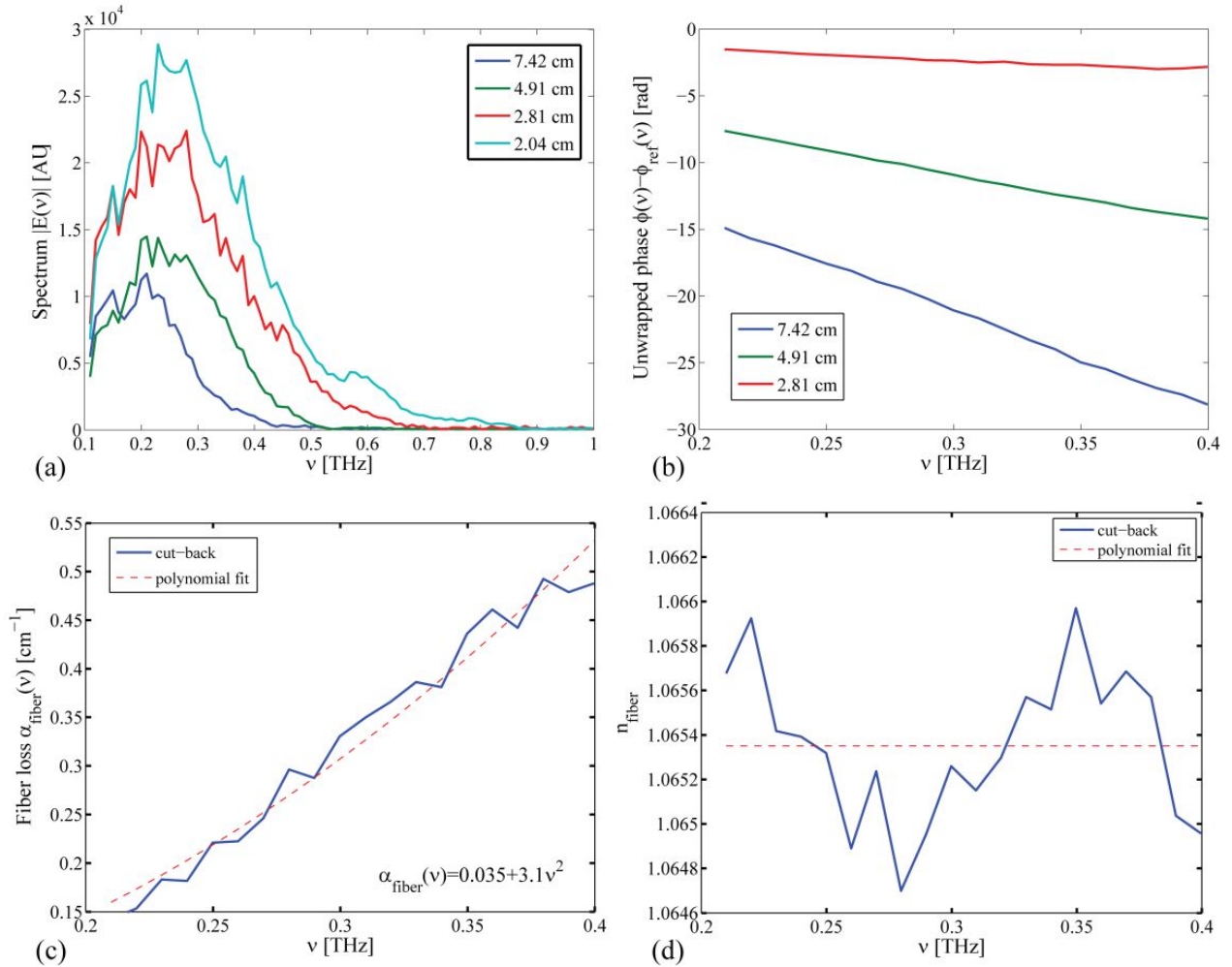


Figure 3.6 Cutback measurements using 5 mm-diameter silk foam fiber. (a) Unnormalized transmission spectra, (b) unwrapped phases (relative to the 2.04 cm-long fiber reference). Extracted (c) fiber absorption losses, (d) modal effective refractive index.

to the fiber of length $L > L_0$ can be calculated as:

$$E_{\text{fiber}}(t, L) = \text{ifft} \left\{ \text{fft} [E_{\text{fiber}}(t, L_0)] \exp \left[\frac{-i\omega [n_{\text{foam}}^r(\omega) - 1] [L - L_0]}{c} - \alpha_{\text{foam}}(\omega)(L - L_0) \right] \right\} \quad (3.14)$$

In order to reproduce reliably the time traces at various fiber lengths using Equation 3.14, one needs to know the dependence of the modal refractive index (real part), as well as of the modal losses in a broad frequency range covering the whole THz spectrum. Polynomial approximations for the modal loss and for the modal effective refractive index (Equations 3.11 and 3.13) found from the spectral and phase analysis of the cutback data are only valid in the narrow spectral range of $0.2 \text{ THz} < \nu < 0.4 \text{ THz}$. Therefore, when trying to reproduce the measured cutback time traces using Equations 3.11 and 3.12, one does not, generally, expect to find a good agreement. In order to approximate correctly modal refractive index and modal loss in the broad THz frequency range, we evaluate them from the exact complex dispersion relation of the fundamental HE_{11} mode of a 5 mm-diameter circular stepindex fiber. This dispersion relation is calculated using standard transfer matrix theory (see, for example [97] assuming silk foam as a core material. Particularly, we suppose that the real part of the core refractive index is frequency independent n_{core}^r , while the core material absorption losses have quadratic dependence on frequency $\alpha_{\text{core}} = \alpha_1 \cdot \nu^2$. Next, we adjust the values of n_{core}^r and α_1 in order to obtain the best possible fit between the experimental and analytical time traces. Particularly, for every choice of the core material parameters n_{core}^r and α_1 we recalculate the fundamental HE_{11} mode dispersion relation that we later use in Equation 3.14 to compute the time traces. As in the case of bulk foam samples, we note that n_{core}^r mostly affects pulse position along the time axis, while α_1 has a strong effect on the pulse width. By fitting the pulse positions and the pulse widths for various fiber lengths (Figure 3.7 (a)), we find the following core material parameters that best fit all the time traces:

$$\alpha_{\text{core}}[\text{cm}^{-1}] = 3.5 \cdot (\nu[\text{THz}])^2 \quad (3.15)$$

$$n_{\text{core}}^r = 1.058 \quad (3.16)$$

The found values for the core material refractive index and losses are close to the values found for the bulk foam samples (Equations 3.9 and 3.10) For completeness, in Figure 3.7 (b) we present dispersion relation and losses of the fundamental HE_{11} mode of a 5 mm-diameter silk foam fiber calculated using core material parameters at Equations 3.15 and 3.16.

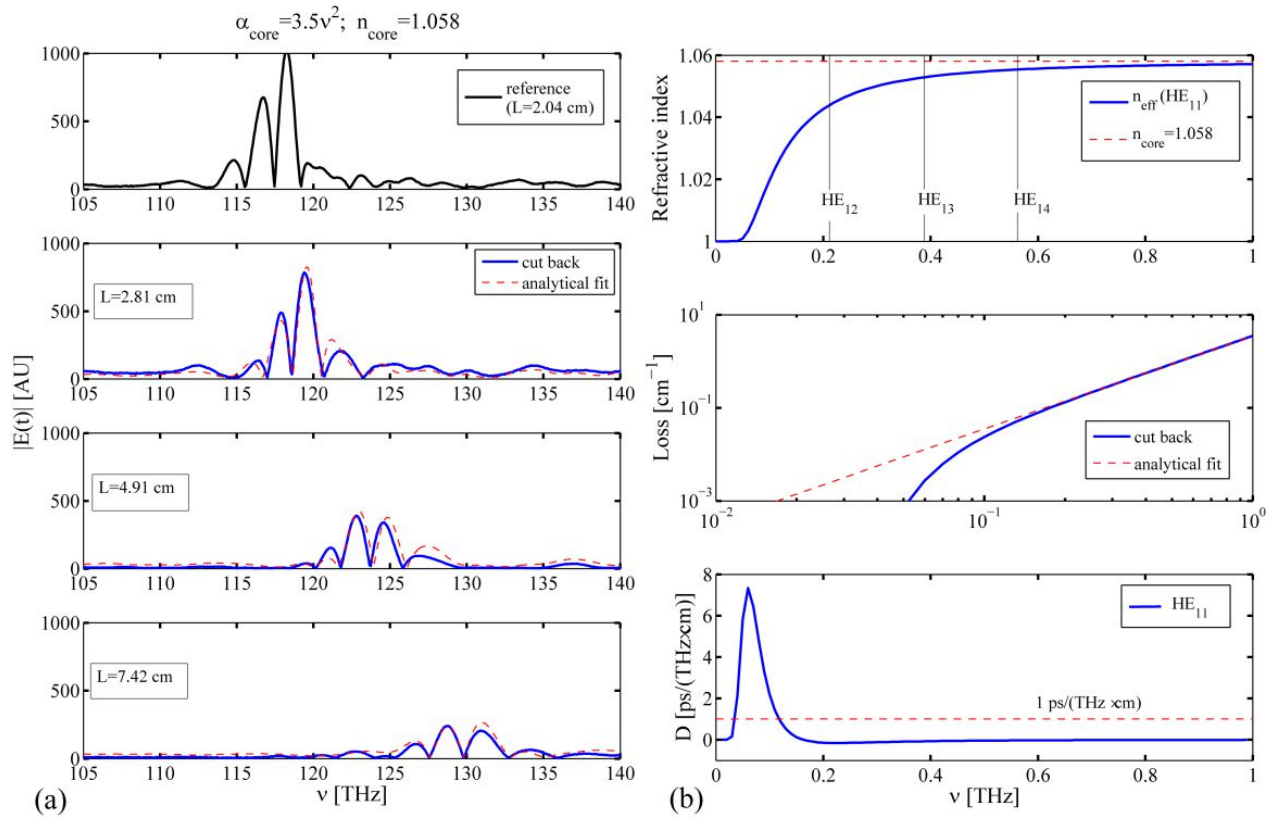


Figure 3.7 Time traces corresponding to the cutback measurements of 5 mm-diameter silk foam fibers. (a) Solid lines – experimentally measured time traces, dotted lines – analytical fit (Equation 3.14) using 3.15 and 3.16 for the core material refractive index and bulk losses. (b) Optical properties of the fundamental HE_{11} mode of a silk foam fiber.

3.6 Guidance mechanism in the silk foam fibers

As it is detailed in our prior work [89, 94, 97], a circular micro porous step-index fiber operates in the subwavelength regime if the operation frequency is smaller than a characteristic value of $\nu_0 = c/(\pi d\sqrt{\Delta\epsilon})$ (see p.116, and ch.11 of [97]), where d is the fiber diameter and $\Delta\epsilon$ is the difference in the effective dielectric constants of the fiber core and cladding materials. In the case of silk foam fibers considered in this work ($d \sim 5 \text{ mm}$, $n_{\text{core}} \sim 1.058$), the characteristic frequency is, therefore, $\nu_0 \sim 0.055 \text{ THz}$. In the subwavelength guidance regime the fiber supports a single doubly degenerate HE_{11} mode, which has a strong field presence outside of the fiber core. In this regime, modal guidance is very sensitive to the environment, and light guidance can be easily lost due to scattering on the imperfections at the core/air interface. In the vicinity of ν_0 , the fundamental mode shows fast transition from the subwavelength guidance regime to the strong confinement in the fiber core (Figure 3.7 (b)), thus resulting in the relatively large value of the modal group dispersion $D_{\text{max}, \nu \sim \nu_0} \sim d\Delta\epsilon^{3/2}/(4c^2 n_{\text{clad}}) \approx 6 \text{ ps}/(\text{THz}\cdot\text{cm})$. When increasing operation frequency, the mode remains well confined in the fiber core, and eventually, at frequencies higher than $2.41 \cdot \nu_0 \sim 0.13 \text{ THz}$ the fiber becomes multimode. For practical purposes, however, the multimode nature of the fiber does not reveal itself up to a higher frequency of $3.83 \cdot \nu_0 \sim 0.21 \text{ THz}$ (see p.121 of [97]), as centered and normally incident THz Gaussian beam used for fiber excitation cannot excite most of the higher order modes due to symmetry mismatch. At these intermediate frequencies fiber mode dispersion decreases to a fraction of its maximal value (achieved in the vicinity of ν_0), and it becomes smaller than $\sim 1 \text{ ps}/(\text{THz}\cdot\text{cm})$ (Figure 3.7 (b)). Furthermore, even at frequencies as high as $10.2 \cdot \nu_0 \sim 0.56 \text{ THz}$, only 4 modes can be excited in the fiber core (using THz Gaussian beam focused into the fiber center as the excitation source), with most power propagating in the fundamental HE_{11} mode. Finally, at these higher frequencies, modal loss is virtually identical to the bulk absorption loss of the silk foam due to high modal confinement in the fiber core.

In Figure 3.8 we summarize some important properties of the fundamental HE_{11} mode of silk foam fibers of various diameters. We assume the core refractive index to be $n_{\text{core}}^r = 1.058$. In Figure 3.8 (a) we present the longitudinal flux distributions corresponding to the fundamental HE_{11} modes of the two silk fibers with diameters of 1.5 mm and 4 mm at various operation frequencies. At low frequency (0.2 THz), a significant portion of the modal fields is found outside of the fiber core and in the low-loss air cladding, which is especially pronounced for the 1.5 mm-diameter fiber. This is the regime of subwavelength guidance. When increasing the frequency of operation significantly beyond the characteristic frequency of subwavelength guidance ($\nu_0 \sim 0.06 \text{ THz}$ for 4 mm-diameter fiber and $\nu_0 \sim 0.16 \text{ THz}$ for

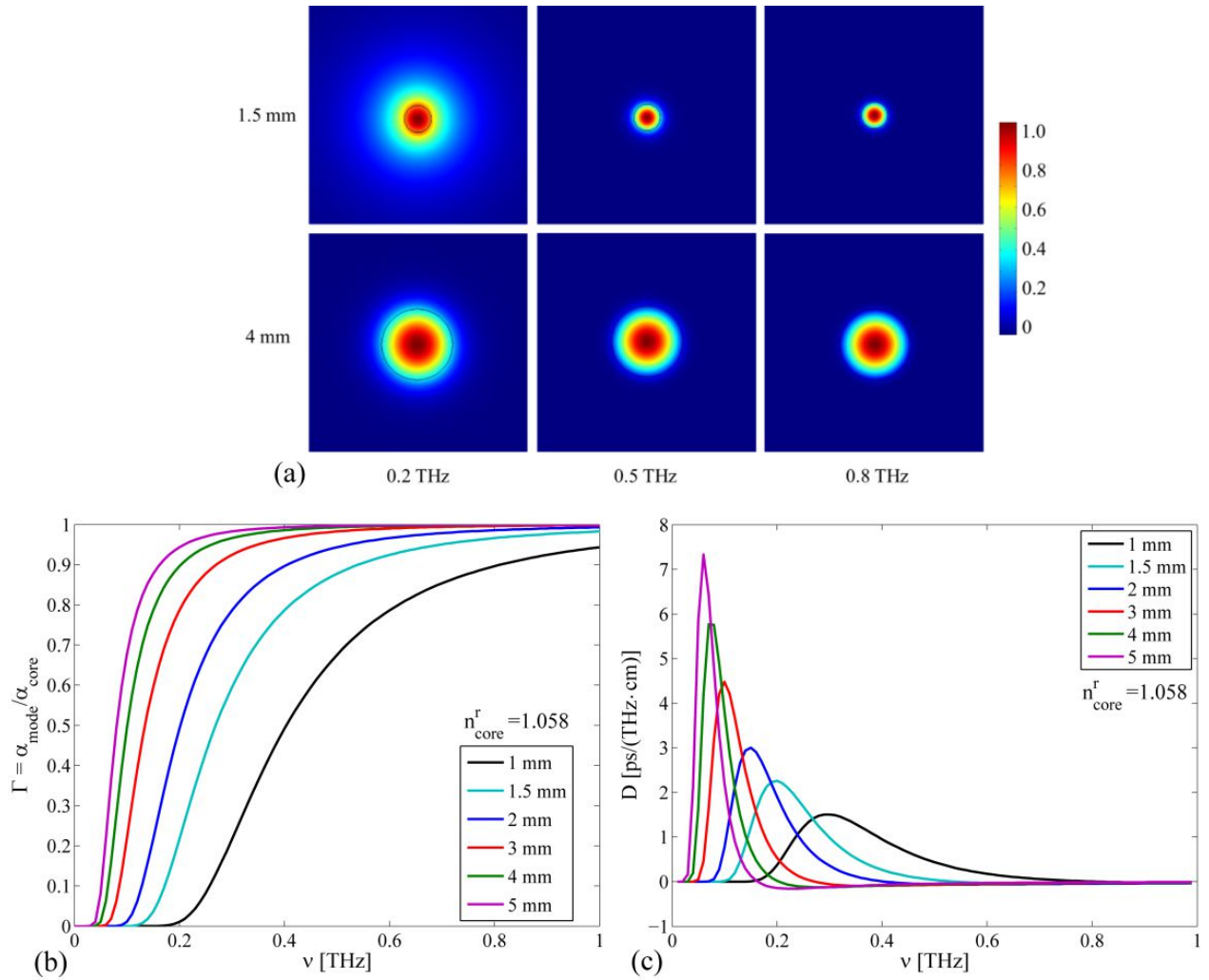


Figure 3.8 (a) Longitudinal flux distribution in the fundamental HE_{11} mode of a step-index silk foam fiber at various frequencies. Black circle marks the core/cladding interface. Top row – fiber diameter is 1.5 mm. Bottom row – fiber diameter is 4.0 mm. (b) Propagation loss of HE_{11} mode normalized by the bulk absorption loss of the core material. (c) Group velocity dispersion of the HE_{11} mode.

1.5 mm-diameter fiber), the fundamental guided mode shows strong localization in the fiber core. In this regime, fiber propagation loss becomes virtually identical to the core material loss. In Figure 3.8 (b) we present loss of the fundamental fiber mode normalized by the value of the core material absorption loss $\Gamma = \alpha_{\text{mode}}/\alpha_{\text{core}}$. Clearly, transition from the subwavelength guidance regime to the regime of strong confinement of the modal fields in the fiber core clearly correlates with the rapid increase in the modal propagation loss.

Finally, in Figure 3.8 (c) we present group velocity dispersion of the fundamental mode of a foam fiber for various values of the fiber diameter. Modal dispersion is maximal in the vicinity of the characteristic frequency ν_0 which is not surprising as modal localization changes rapidly in this frequency range. In the regime of strong modal confinement in the fiber core ($\nu > \nu_0$), modal dispersion is significantly lower than its maximal value by as much as two orders of magnitude. Therefore, for larger diameter fibers (> 3 mm), at frequencies above 0.2 THz, modal dispersion can be significantly lower than 1 ps/(THz·cm). At the same time, modal losses will be identical to that of the core material, which can become significant at higher frequencies (> 3 cm⁻¹) at 1 THz). For smaller diameter fibers (< 3 mm), the characteristic frequency ν_0 shifts into the mid THz range and group velocity dispersion becomes significant > 1 ps/(THz·cm) even at higher frequencies > 0.2 THz. At the same time, in mid THz frequency range, small diameter fibers guide predominantly in the subwavelength guidance regime characterized by small propagation losses < 1 cm⁻¹ at 1 THz. Therefore, when deciding on the optimal diameter of a foam fiber, there is a tradeoff between high loss/low modal dispersion of the large-core fibers and low loss/high modal dispersion of the small-core fibers.

3.7 Discussion

We would like to comment now on several important properties of silk foams and waveguides made from such foams that were demonstrated in this paper. First, the absorption loss of silk foams in THz spectral range is reduced by almost one order of magnitude compared to that of the bulk silk. By further decreasing the porosity of the silk foam, we could further reduce the foam loss to be comparable to that of standard low loss THz plastics such as polyethylene. At the same time, the main advantage of the silk foam compared to standard plastics is that it is biocompatible, biodegradable and, due to its porous nature, it could be biofunctionalized with various materials. Moreover, the foam porous structure can be useful for sampling of various biofluids using capillary effect for applications in biosensing, for instance. This cannot be done with standard plastics. On the other hand, if the goal is to prevent liquid penetration in the liquid core, one can trivially seal the pores on the fiber

surface.

Second, in this paper we report a waveguide that has air as cladding, and therefore the guided mode is partially present outside of the foam material. In order to confine the guided mode fully within the fiber structure one can use foams of two different densities for the fiber core and cladding regions. As it follows from the discussion of the theoretical section, foam based fibers can be designed with 1 mm dimensions, thus making it comparable with many existing endoscopes for in vivo applications.

Finally, we want to clearly distinguish foam fibers presented in this paper and porous plastic fibers (see [94, 98], for example) developed for guidance of THz waves. The size of the pores in foams is at least an order of magnitudes smaller than the size of the pores in the abovementioned porous plastic fibers. The porous fibers are manufactured using drawing of structured preforms, therefore limiting the material of a fiber to thermoplastics. At the same time, silk cannot be drawn, therefore a completely different processing has to be used for the fabrication of silk fibers. In fact, the fabrication method presented in this paper is suitable for many biologically important water soluble materials that cannot be otherwise drawn into optical fibers. Finally, we note that although many other low-loss hollow-core terahertz waveguides exist with approximately the same fiber diameter that our silk fiber, most of such fibers are either made of plastic or plastic/metal combinations. So far, to the best of our knowledge, there were no demonstrations of THz fibers made from truly biocompatible materials such as silk.

3.8 Conclusion

Our work is motivated by the lack of bio-friendly waveguides for low-loss, low-dispersion guidance of terahertz waves. Such waveguides are desirable in the numerous potential applications in remote and stand-off sensing in bio-medical and agroalimentary industries. In this paper, we present novel silk foam material that was developed in our group using freeze drying (lyophilisation) of the purified silk solutions. Weight and volume measurements show that our foam material is 94% porous by volume. We use cutback technique to characterize optical properties of the silk foams in the THz spectral range. We find that refractive index of silk foams used in our experiments is close to that of air (~ 1.06), while material absorption loss of the silk foams is almost an order of magnitude smaller than that of bulk silk at THz frequencies, which is due to presence of low-loss gas in the foam structure. Moreover, bulk foam losses are strongly dependent on frequency and are in the $\sim 1-2 \text{ cm}^{-1}$ range at 0.5 THz, while being less than $\sim 1 \text{ cm}^{-1}$ at lower frequencies $< 0.3 \text{ THz}$. To demonstrate potential of silk foams for guiding of THz waves, we then cast 5 mm-diameter, 10 cm-long silk foam

fibers and use cut back technique to describe their optical properties in the THz frequency range. We find that 5 mm-diameter, 10 cm-long fibers guide well in the mid THz frequency range of 0.2~0.5 THz with a typical loss less than 0.8 cm^{-1} . In this spectral range, modal group velocity dispersion is estimated to be less than $0.2 \text{ ps}/(\text{THz}\cdot\text{cm})$. Our experiments confirm the overall feasibility of using silk foams as an enabling material for the development of biocompatible guided wave devices in THz frequency range.

3.9 Experimental section

3.9.1 Purified aqueous silk fibroin solution

Bombyx mori silk is composed of silk fibroin protein covered by sericin protein. For biomedical applications, sericin should be removed as it provokes adverse reaction of the immune system [66]. Once sericin is removed, the silk fibroin protein can be dissolved in an aqueous LiBr solution, purified and then formed into various shapes using standard solution-based processes [95]. First, the Bombyx mori cocoons were cut into pieces and boiled for 30 min in a Na_2CO_3 (0.02 M). Then, they were rinsed three times with deionized water (20 min per rinse) in order to remove the gluey sericin protein. The degummed silk mass was then placed in the fume hood over night to dry. Next, dry silk was dissolved in LiBr solution (9.3 M) at room temperature, yielding a 20 wt% solution. This solution was then dialyzed in deionized water using a Slide-a-Lyzer dialysis cassettes (Pierce, MWCO 3500) for 48 h. After that, the solution was centrifuged twice at $4 \text{ }^\circ\text{C}$ with a spinning speed of 9000 r.p.m. for 20 min. Finally we have obtained an aqueous silk solution with silk concentration of 7.0~8.0 wt%, which was determined by weighing the silk material after drying a part of the solution (see [99] for more details). The final silk solution is clear with a slight tint of yellow. The silk solution is slightly more viscous than water, and it can be stored at $4 \text{ }^\circ\text{C}$ for at least one month.

3.9.2 Silk foams and foam-based fibers

In order to fabricate silk foam, we used lyophilisation method that causes less damage, shrinkage or toughening of the material being dried than other dehydration methods. A conical test tube with silk solution was placed vertically in a freezer (dry ice filled box) at $-80 \text{ }^\circ\text{C}$ for several hours until the solution was completely frozen. Then the frozen sample was connected to a low vacuum system (mechanical pump). Eventually, the water sublimated and left behind the silk foam in a test tube.

THz fibers were cast from the purified silk fibroin solution using 5 mm-diameter plastic

straws as molds. We started by filling the straws with silk solution with one end of the straw connected to a syringe, while the other end immersed in solution. While filling the straws, care must be taken to avoid introduction of air bubbles. After the straws were filled, one of their ends was closed, the straws were frozen at $-80\text{ }^{\circ}\text{C}$, and then they were placed under vacuum for lyophilisation. After the removal of water, the THz fibers were easily pushed out of the molds.

3.10 Acknowledgments

H. Guerboukha and G. Yan contributed equally to this work. This work was supported in part by the NSERC Strategic Grant 430420-12.

CHAPTER 4 ARTICLE 2 : TIME RESOLVED DYNAMIC MEASUREMENTS AT THz FREQUENCIES USING A ROTARY OPTICAL DELAY LINE

This chapter addresses the issue of the time acquisition. It is a transcription of a manuscript published in *IEEE Transactions on Terahertz Science and Technology* [26]. As we saw in Chapter 1, in a regular THz-TDS system, the data acquisition is time-consuming, its main limitation being the linear micropositioning delay line. Mechanically, a rotary movement can reach high speeds. In a recent publication, our group presented curvilinear surfaces that provide, in reflection, linear delay line with the rotation angle [27]. In this chapter, we present the experimental implementation of such a surface along with its complete characterization. Additionally, new practical applications for the THz are explored.

4.1 Authors

Hichem Guerboukha, Andrey Markov, Hang Qu and Maksim Skorobogatiy

Department of Engineering Physics, Ecole Polytechnique de Montréal, H3C 3A7, Montreal, Quebec, Canada

4.2 Abstract

Fabrication, characterization, and applications of a fast rotary linear optical delay line (FRLODL) for THz time-domain spectroscopy are presented. The FRLODL features two reflective surfaces with spatially separated incoming and outgoing beams. It has been manufactured using CNC machining. A linear dependence of the optical delay on the rotation angle allows a straightforward extraction of the conversion factor between the acquisition time (in ms) and the terahertz pulse time (in ps). We also discuss the accuracy of the rotary delay line detailing the possible sources of imprecision. The FRLODL has been tested using rotation speeds of up to 48 Hz, corresponding to an acquisition rate of up to 192 Hz with four blades incorporated on the same disk. At high speeds we observe a decrease of the bandwidth due to the limitations of the electronics, in particular, the transimpedance amplifier. An error analysis is performed by experimentally evaluating the signal-to-noise ratio and the dynamic range. With regard to the applications of the FRLODL, we first present observation of the evaporation of liquids, namely water, acetone and methanol. We then demonstrate monitoring of the spray painting process. Finally, detection of fast moving objects at 1 m/s and

their thickness characterization are presented.

4.3 Introduction

For several decades, THz spectroscopy and imaging have been used in many different applications [100]. Due to the relatively low loss of most dry materials in the THz spectral range, and due to the strong sensitivity of material losses to humidity, there has been a growing interest in using THz waves in non-destructive imaging and process control. Various industrial applications of THz spectroscopy are currently under investigation. In particular, for use in detection of inorganic inclusions in food products, detection of dangerous chemicals disguised by packaging, detection of defects in packaged electronic chips, as well as monitoring of water content in paper and textile fabrication lines. However, some challenges still remain in THz spectroscopy commercial generalization.

One of these difficulties lies in the limited scanning speed of a THz system. For rapid terahertz imaging and real-time process monitoring, a high scanning rate optical delay line is required for efficient sampling of the terahertz pulses. In a typical THz time-domain spectroscopy system, the THz pulse is sampled in time by means of delay lines based on linear micropositioning stages with mounted retroreflectors. The popularity of this solution is related to reliability of the micropositioning technology and its relatively low price. Moreover, optical delay produced by such delay lines depends linearly on the stage displacement, which greatly simplifies encoding and readout of the optical delay value of a micrometer linear delay line. While this method permits high precision of the pulse reconstruction, it is time-consuming, as a single scan takes typically several seconds.

To solve the low acquisition rate problem, several approaches have been explored [27, 101–115]. Galvanometer based delay lines were presented over 20 years ago for high speed scanning of THz pulses [101]. In the aforementioned system, the optical beam is reflected by a mirror mounted on a galvanometer vibrating device oscillating with a fixed amplitude and frequency. This system was capable of achieving an optical delay of 300 ps with a scanning rate of 30 Hz. However, the position and velocity of the mirror in this setup changes sinusoidally; consequently, the optical delay does not change linearly in time.

As of recently, rotating prisms in the optical [102–104] or in the THz [105] beam path have been suggested. In that case, the delay is modified by the optical path inside a rotating prism made of a higher refractive index material. In this arrangement, the reflected beam follows the same path as the incident beam, thereby requiring separation of the two at the output of the delay line. Scanning rates as high as 380 Hz were demonstrated with optical delay in

100s of ps. Placing the cube on the air turbine can further improve the scanning speed by almost an order of magnitude. Introducing a rapidly rotating prism in the THz beam path [105] instead of the conventional optical path is beneficial in terms of its decreased sensitivity to fabrication imperfections due to much longer THz wavelengths as compared to the laser wavelength. However, these systems generate an optical delay that is strongly nonlinear with respect to the rotation angle, leading to complex time-consuming calibration on raw data. Furthermore, when using larger prisms, the group velocity dispersion of the prism material can become important leading to a pulse broadening and attenuation of both THz and optical beams.

Asynchronous optical sampling has also been used for THz [116]. In these systems, probe and source pulses are provided by two mode-locked femtosecond lasers with slightly different frequencies. A repetition rate of several kHz can be obtained using this technique. However, the use of two femtosecond lasers is expensive and requires precise adjustment that may affect the stability of the recorded THz pulse.

We also note that fast optical delay lines are required in other research fields, for example, in optical coherence tomography (OCT). In those systems, multiple-pass cavity delay lines [106, 107] and combinations of a curved or a straight mirror and a scanning mirror [108, 109] were suggested. Nevertheless, they feature small optical delays (< 20 ps), which are suitable for OCT applications, but not for THz time-domain spectroscopy. In the latter, large optical delays increase the spectral resolution. In addition, longer optical delays allow the sampling of high refractive index and/or dispersive materials.

To date, several solutions based on rotating mirrors and curvilinear surfaces were demonstrated for THz applications [110–114]. Such designs feature linear dependence of the optical delay on the rotation angle, as well as large maximum delay and high scanning rates. When using rotary delay lines that feature linear dependence of the optical delay on the reflector rotation angle, one can, in principle, forgo complex optical encoders if the rotation rate is precisely controlled. By placing several reflectors on the same rotating base, one can increase the acquisition speed by an order of magnitude. Scanning rates of 400 Hz and the total delay of 140 ps have been demonstrated when using six reflectors, all fitting into an 8cm diameter circle [114].

Recently, we presented several classes of analytical and semi-analytical solutions for the design of fast rotary linear optical delay lines (FRLODL) [27, 115]. The optical delay provided by such systems is proportional to the reflector size. When using relatively small systems that fit into a 10 cm-diameter circle, an optical delay in excess of 600 ps can be achieved, which is comparable to the optical delay generated by a typical linear micropositioning stage

with a retroreflector.

The rotary delay lines require careful design of the shapes of their reflector surfaces. In particular, we require the resultant optical delay to be linear and long enough for THz applications (at least 100 ps). Also, at the input and output of the FRLODL, the optical beams must stay spatially invariant and separated during the reflector rotation. The latter enables to forgo the use of beamsplitters to separate the incoming and the outgoing beams, thus reducing the loss of the laser power.

The main goal of this work is to understand the engineering challenges arising during the experimental implementation of a rotary delay line. We first discuss the accuracy of the FRLODL, detailing the possible sources of imperfection. We consider both errors occurring due to a finite size of the laser beam (as opposed to an optical ray) and the precision with which the blade rotation frequency can be maintained, as well as the errors coming from the limited accuracy of CNC machining. Then, the experimental implementation of the FRLODL is presented. We demonstrate characterization of the rotary delay line, confirm its linearity, and compare the system's response at different rotation speeds. Finally, we present examples of practical applications for the FRLODL: evaporation of liquids, monitoring of spray painting, and detection of fast moving objects.

4.4 Characterization of the FRLODL

The operating principle of the FRLODL has been introduced in details in our previous papers [27, 115]. The FRLODL consists of four blades, and an individual blade is composed of two curvilinear reflectors. In Figure 4.1 (a) we show the working principle of an individual blade. We assume that the incoming light beam is arriving parallel to OZ and that it is displaced by R_i along the OY direction. The incoming beam is reflected by the first rotating reflector at the point $(x_i(\theta), R_i)$ onto the second rotating reflector at the point $(x_o(\theta), R_o)$, where θ is the angle between the OY axis and OZ axis. Finally, the beam is sent out of the delay line system along a line parallel to the OZ axis. Note that, regardless of the rotation angle, the outgoing beam always follows the fixed path; in other words, R_o is a constant value. Moreover, another important property of the FRLODL is that the optical delay provided by such a rotating blade is a linear function of the rotating angle. In [27], we have shown that a blade with two curvilinear reflectors could be designed by numerically solving a first-order differential equation. Similarly, we have also demonstrated that once the incoming beam position R_i is specified, only a unique solution of the curvilinear reflectors can be numerically obtained. Note that the maximum optical delay of the FRLODL system is dependent on the value of R_i . In that paper, we specified $R_i \approx 2.97$ cm in order to maximize the optical delay

of the system that fits into a 10 cm diameter circle. The corresponding optical delay as a function of the rotation angle is numerically calculated (see Figure 4.1 (b)).

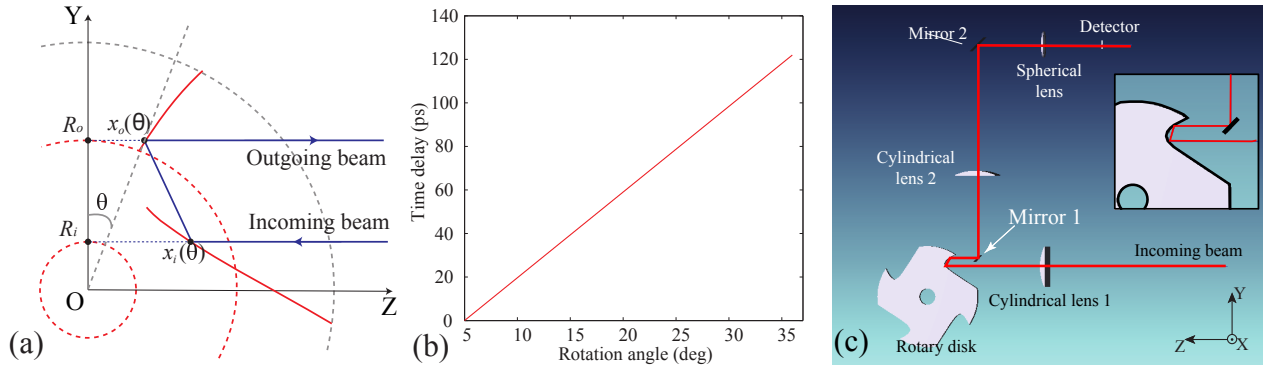


Figure 4.1 (a) The schematic of an individual rotating blade consisting of two curvilinear reflectors [27]; (b) The time delay of the FRLODL; (c) The optical setup of the FRLODL in Zemax.

To elucidate the working principle of the FRLODL, we perform a simulation based on the commercial optical design software Zemax. In Figure 4.1 (c), we show the Zemax schematic of the whole delay line system. As a light source, we use a collimated Gaussian beam with a waist radius of 0.5 mm. For an incoming beam with a finite size, the curvilinear reflectors of the disk have a "lens" effect on the beam and thus defocus the incoming beam in the OY direction. To minimize this effect, we place the FRLODL between two cylindrical lens (focal length: 100 mm) in order to collimate the outgoing beam. Finally, the outgoing beam is focused by another spherical lens (focal length: 60 mm) to a virtual detector which interrogates the spatial position and intensity distribution of the outgoing beam. In our simulation, we trace 20000 rays. Note that, in this Zemax simulation, the optical setup follows the emitter arm of the experimental setup delay line closely, as demonstrated in the following section.

In our Zemax simulation, we also set $R_i = 2.97$ cm, and subsequently interrogate changes in position and radius of the outgoing beam on the virtual detector as a function of the rotation angle θ of the FRLODL disk. In Figure 4.2 (a-d), we show the outgoing beam on the detector screen at several rotation angles. During the simulation, the curvilinear reflectors are considered to be perfectly planar in OX direction (Figure 4.1 (c)), and consequently, they have no optical aberration in this direction. However, we note that the centroid position and intensity distribution of the outgoing beam vary considerably in the OY direction when the disk rotates to different angles. To explain this, we simply recall that the reflectors have irregular curvilinear profiles that would defocus the incoming beam. In addition, we note

that when the rotation angle is less than 6° or greater than 34° , the incident beam is cut by the edge of the reflectors, resulting in an incomplete reflection. Between 6° and 34° , the number of rays reaching the detector (as calculated by Zemax) is the same as the emitted number of rays. This shows that the beam is completely reflected.

In Figure 4.2 (e) and (f), we plot changes in the centroid position and the root-mean-square (RMS) radius of the outgoing beam as a function of the rotation angle. Typically, the RMS radius of the outgoing beam is in the range of $6 - 20 \mu\text{m}$, and the centroid position of the outgoing beam oscillates within a $\sim 70 \mu\text{m}$ range. As demonstrated in the following experimental section, the outgoing beam from the FRLODL would be coupled to a photoconductive antenna (emitter) that generates THz pulses. The amplitude of the generated THz signal is dependent on the intensity and the spatial position of the incoupled beam. In the following experiment, therefore, we use an antenna with a $100 \mu\text{m}$ gap that would, in principle, have insignificant influence on the generated THz signal.

In the above simulation, we use an ideal rotary reflection disk without taking into consideration fabrication errors. In practice, the rotary reflection disk is fabricated by CNC machining followed by a diamond paste-polishing process. According to [114], it is reasonable to assume the average surface roughness of the produced reflectors to be $\sim 1 \mu\text{m}$. The imperfect reflector surfaces would lead to optical scattering, changing the intensity distribution and spatial position of the outgoing beam. Therefore, we perform another Zemax simulation that takes into account roughness of the reflector surface ($R_\alpha \approx 1 \mu\text{m}$). First we numerically calculate the profile of the curvilinear reflectors. Then, we add a $1 \mu\text{m}$ -uncertainty in the 3D coordinates of each point on the reflector surfaces. The simulation results shown in Figure 4.3 suggest very strong optical scattering of the outgoing beam. The RMS radius of the outgoing beam is generally on the order of several hundreds of micrometers that considerably exceed the dimension of the photoconductive area in the antenna. Besides, we see pronounced variations in the centroid position and intensity distribution of the outgoing beam. Thus, we expect that the amplitude of the generated THz signal from the antenna would vary a considerable amount as the rotary disk rotates to different angles. This was also confirmed in our experiments as shown in the following section. We note that in order to reduce the amplitude variations, a more precise CNC machining or diamond turning technique should be used for the fabrication of the FRLODL.

The experimental setup is depicted in Figure 4.4. A 100 fs Ti:Sapphire laser (Mai Tai, Spectra-Physics) with a wavelength of 800 nm and a repetition rate of 100 MHz delivers 100 mW and 10 mW to the THz photoconductive emitter and detector antennae (PCA) respectively. A linear delay line is placed on the detector (Tera8-1, Menlo Systems, $5 \times 20 \mu\text{m}^2$ gap)

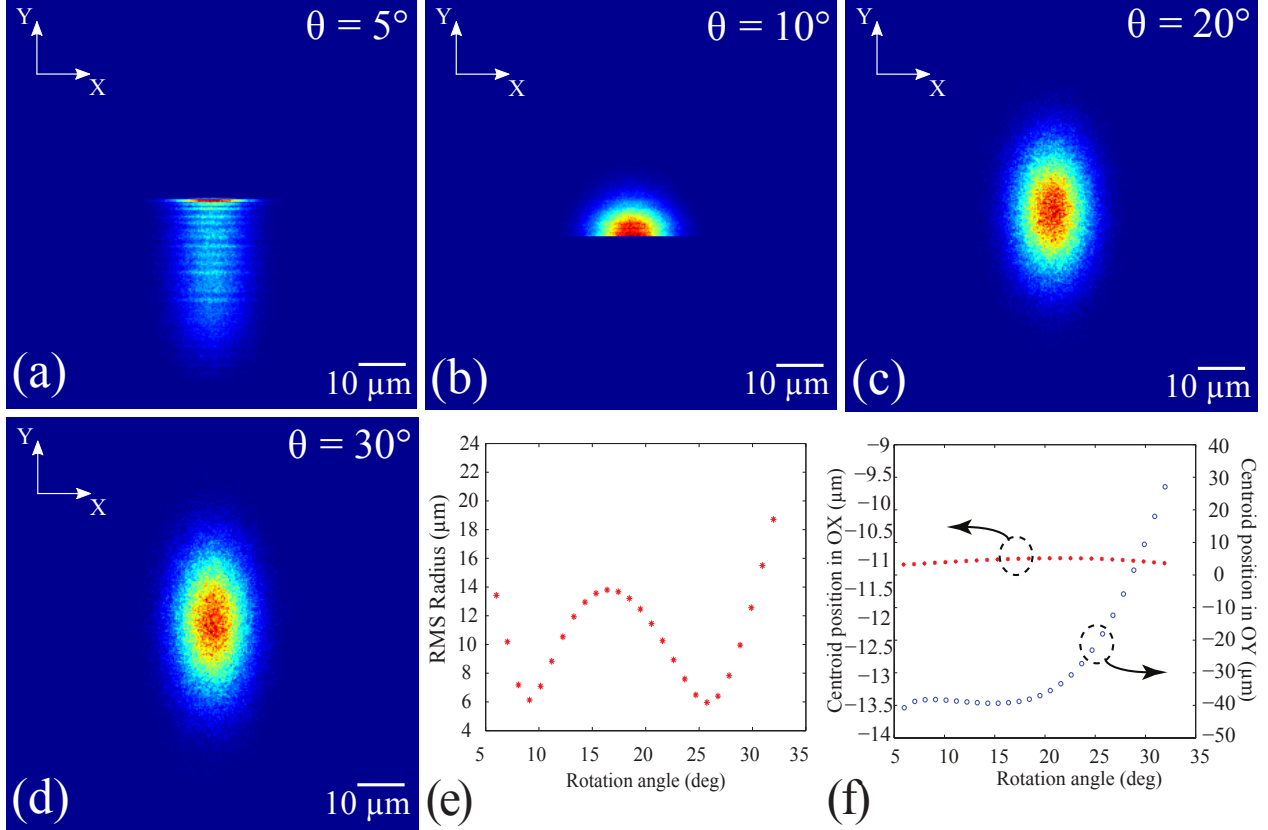


Figure 4.2 (a-d) The outgoing beam captured by the detector screen at the rotation angle θ of 5, 10, 20 and 30° . The rotation angle θ is defined in Figure 4.1 (a). Particularly, when the rotation angle is 5° , the incoming beam is cut by the edge of the curvilinear reflector, thus resulting in an incomplete reflection. (e) The RMS radius of the outgoing beam at different rotation angles; (f) The centroid position of the outgoing beam in OX and OY direction on the detector screen as a function of the rotation angle.

side. While this linear delay line is needed for the initial characterization, we will show later that the FRLODL can be used alone. The FRLODL is placed on the emitter side and, adjacently, a lens focuses the beam on the emitter PCA (T-Era-400A-800-Air, TeTechS, $100 \times 100 \mu\text{m}^2$). During the measurements, the emitter is supplied by 50 V DC. The detector PCA current output is connected to a low noise transimpedance amplifier (DLPCA-200, FEMTO) which enables high signal-to-noise ratio. The analog output of the current amplifier is then connected to a data acquisition card (NI USB-6343, National Instruments) that samples at 500 kHz with 16 bit resolution. In contrast with a regular THz-TDs setup, our FRLODL-based setup does not require using a lock-in amplifier.

The FRLODL surface is made utilizing computer numerical control machining (Charly 2U,

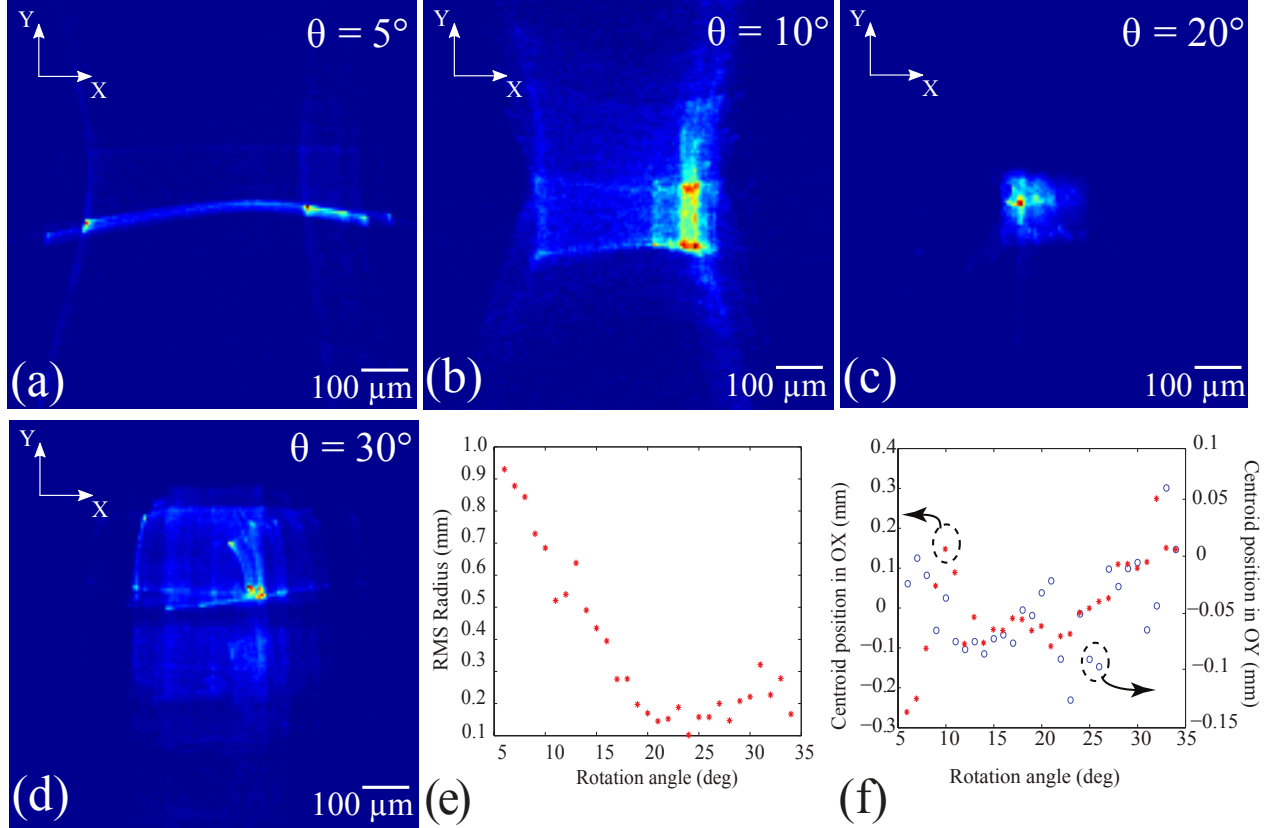


Figure 4.3 (a-d) The outgoing beams reflected by a rotary disk with $1 \mu\text{m}$ average roughness of the reflector surfaces for rotation angles 5, 10, 20 and 30° respectively. The rotation angle θ is defined in Figure 4.1 (a). (e) The RMS radius of the outgoing beam at different rotation angles. (f) The centroid position of the outgoing beam in OX and OY direction on the detector screen as a function of the rotation angle.

CNC machine) with a linear translation precision of $3 \mu\text{m}$ and a repeatability of $20 \mu\text{m}$. The blade surfaces were then manually diamond-paste-polished. The incoming and outgoing optical beams are parallel and have a constant 1 cm separation in space. This configuration avoids the usage of additional moving devices.

Using this technique, we fabricated four blades on the same disk. The number of scans per second increases in proportion to the number of blades on the disk, thereby enabling higher scan rates in a system with the same rotation motor and acquisition setup. To further increase the sampling rate, one could use a disk with a greater radius allowing the incorporation of a larger number of blades. Due to limitations in the optical quality of our blades, there are variations in the generated THz pulse depending on the rotation angle. In Figure 4.5 (a), we present THz time traces for different delays between the emitter and the detector sides

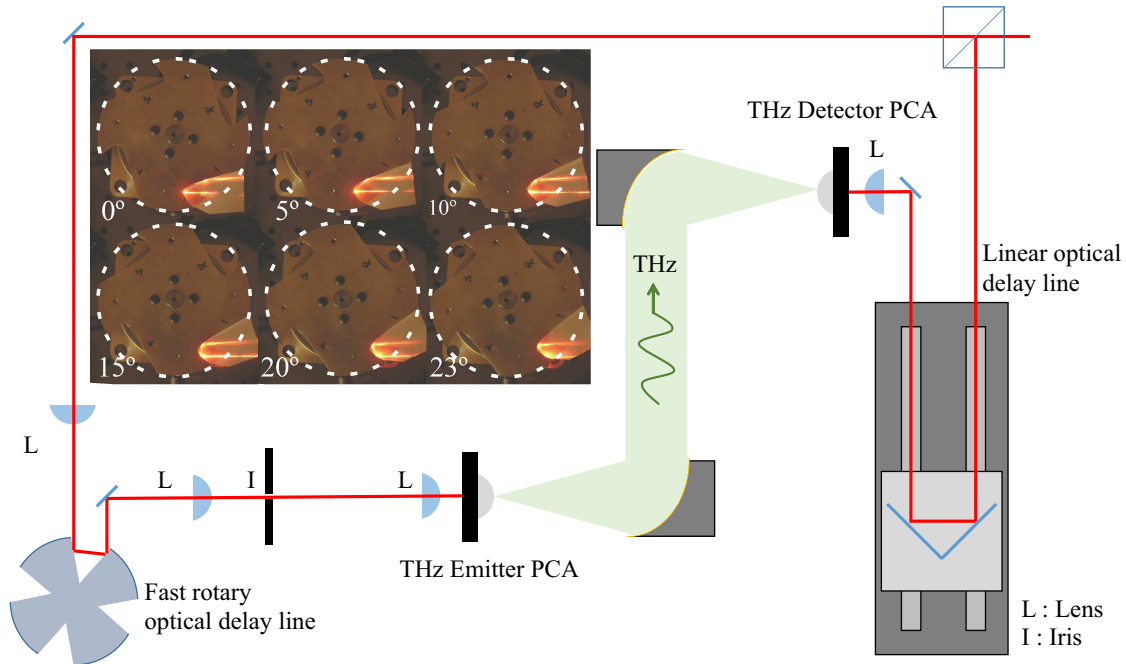


Figure 4.4 The experimental setup. Inset shows the FRLODL disk with its four manufactured blades. Notice the parallel incoming and outgoing optical beams at different rotation angles.

achieved using the fast rotary delay line. We add time delay by moving the linear delay line by increments of $50 \mu\text{m}$ (0.33 ps) over a range of 25 mm (165 ps) and record the resultant THz pulses. As depicted in Figure 4.5 (a), there are amplitude variations that are primarily caused by the quality of the CNC micro-machined FRLODL surface. Indeed, the linear precision of the CNC machining is on the same order as the laser wavelength. As demonstrated in the simulations, this leads to both intensity variations and spatial displacements of the optical beam.

To utilize the full extent of the optical delays provided by the rotary delay line, precise calibration of the generated THz power as a function of the rotation angle is required. However, as we will show in the following sections, multiple THz applications do not require extended delays or focus only on the temporal position of the main THz peak. In this case, calibration is not a prerequisite for the operation of the rotary delay line. To reduce the effect of the beam spatial displacement, we placed an iris on the beam path just before focusing on the THz emitter. Due to the large photoconductive area of the THz emitter, these small variations do not prevent the excitation of THz pulses. In the following, we used only one of the four FRLODL blades to get a consistent rigorous analysis.

In Figure 4.5 (a), the ms-time scale refers to the actual acquisition time as recorded by the

analog-to-digital acquisition card. A linear micropositioning stage with a retroreflector placed on the emitter side was used to calibrate the rotary delay line. Knowing the increment of the main THz peak in the ps-scale (position of the micropositioning stage) and in the ms-scale, it is possible to find a linear relation between the two scales (Figure 4.5 (b)). The slope of this curve confirms the linearity of the FRLODL and provides an experimental conversion factor between the ms and ps-scale (in this case 16.85 ps/ms). Note that this experiment was conducted at a rotation speed of 12 Hz. Therefore, for different rotation speeds, one needs to perform a simple cross-multiplication to find the correct conversion factor. By applying the conversion factor in Figure 4.5 (a), we find a maximum efficient optical delay of ~ 100 ps.

In Figure 4.5 (c), we present several measurements at different rotation speeds of the FRLODL. In principle, acquisition rate can be further increased four times if all the blades on the disk are used. The dashed blue curve corresponds to a scan made by the linear delay line in a regular setup using a lock-in amplifier. The ps-scale was obtained through the cross-multiplication of the conversion factor by the rotation speed, giving appropriate results as can be evaluated by the position of the water lines in the spectrum (Figure 4.5 (d)).

As depicted in Figure 4.5 (c), when enhancing the speed of the scan, the THz pulse time structure becomes less pronounced. This is directly related to the low-noise current amplifier. In our setup, the amplifier has a 10–90 % rise time of $50 \mu\text{s}$. Converting this value to ps-scale using the above conversion factor, we find 0.84 ps at 12 Hz, but 3.4 ps at 48 Hz. As a result, the THz pulse will be less defined as each data point corresponds to a time average over longer sampling intervals at higher FRLODL rotation speeds. The impact of the acquisition electronics can be directly seen in the spectrum, in which bandwidth decreases with increase in the rotation speed. To overcome this issue, one could either use a faster transimpedance amplifier or increase the power of the THz signal.

Finally, to complete the characterization of our FRLODL system, we present error measurements (Figure 4.5 (e) and (f)). We take standard time-based error calculation to define signal-to-noise ratio (SNR) and dynamic range (DR) [117]:

$$\begin{aligned} \text{SNR} &= \frac{\text{mean at peak maximum}}{\text{standard deviation at peak maximum}} \\ \text{DR} &= \frac{\text{mean at peak maximum}}{\text{standard deviation at noise level}} \end{aligned} \tag{4.1}$$

In this definition, the SNR measures the accuracy on the amplitude, while the DR gives an idea of the system response to strongly attenuating samples. In a regular setup with a lock-in amplifier, the SNR is greatly enhanced because of the high value of the integrating time

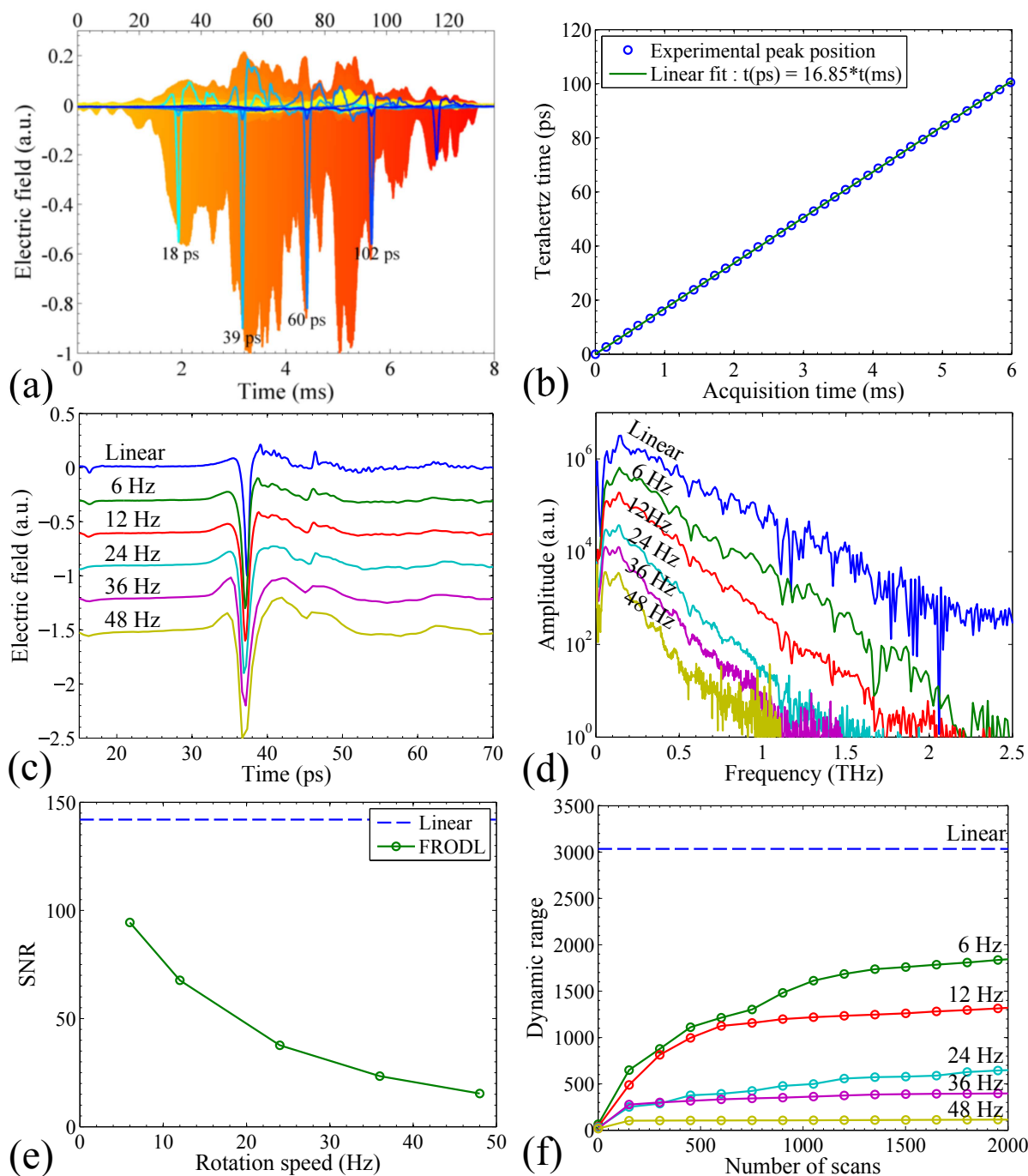


Figure 4.5 Characterization of the FRLODL. (a) THz time traces for different delays between the emitter and detector lines and (b) the deduced positions (in ms) of the main peak knowing the delay (in ps). (c) The averaged and normalized pulses for different rotation speeds and (d) the corresponding power spectra. The arrow points to the noise level of the FRLODL measurements. The "Linear" curve corresponds to the measurement with a standard micropositioning linear stage and is added for comparison of the positions of the water absorption lines. (e) The signal-to-noise ratio for different rotation speeds and (f) the dynamic range as a function of the number of averaging.

constant. For example, with a 100 ms time constant, we obtain an SNR of approximately 140. Obviously, with the FRLODL, the SNR decreases with the rotation speed and again, this is linked to the rise time of the transimpedance amplifier. In Figure 4.5 (f), we present the DR after averaging the pulse. In some applications, it is possible to perform this averaging at the expense of the total acquisition time. A regular setup with a linear micropositioning stage gives a DR of approximately 3000, but with a total acquisition time of 3-4 minutes, while, in comparison, our FRLODL produces a DR of nearly 1000 with 20 seconds (250 scans at 12 Hz) acquisition time.

4.5 Practical applications of the FRLODL

4.5.1 Monitoring of the evaporation process

As a potential application of the FRLODL for THz spectroscopy, we first present real-time non-contact monitoring of the evaporation process for different liquids. For this purpose, a paper tissue is positioned in the path of the THz beam and THz signal recording is initialized using the FRLODL at a rotation speed of 12 Hz. A volume of 50 μL of water, acetone, or methanol is then applied to the surface of the tissue. In Figure 4.6 (a), we show the electric field amplitude variation of the main peak. The THz wave passing through the liquid is absorbed differently depending on the absorption coefficient and the thickness of the liquid layer. As the liquid evaporates, the peak amplitude returns back to its initial value. As expected, acetone evaporates faster than methanol and water [118]. In particular, in Figure 4.6 (b), we present time traces and spectra for acetone evaporation. One can clearly see the absorption in a broad range of frequencies related to the losses in the liquid.

It is worth noticing that in Figure 4.6 (a), the apparent noise is directly correlated to the limited signal-to-noise ratio. As defined above, the SNR is a measure of the accuracy on the amplitude measurement. At a rotation speed of 12 Hz, with an SNR of roughly 70, it is still possible to get sufficient contrast between the noise and the signal. Naturally, it is possible to decrease the rotation speed in order to improve the SNR, however, in this case ms-time scale processes will not be resolved.

4.5.2 Monitoring of spray painting

In the previous experiment, the three tested liquids were transparent in the optical range. Contrarily, in this section, we will present a monitoring of the drying process of non-transparent red enamel spray paint. A paper substrate is placed in the path of the THz beam and recording of the THz signal is initialized while the FRLODL rotates at a speed of 10 Hz. We then

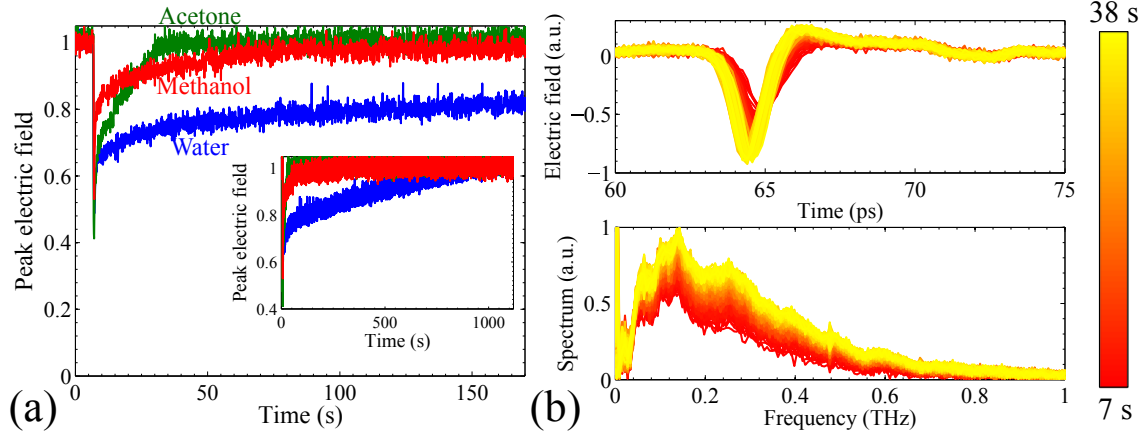


Figure 4.6 The evaporation process measured with the FRLODL. (a) The normalized electric field amplitude of the main THz peak as a function of time for water, acetone and methanol. Inset: longer time scale. (b) The time traces (top) and spectra (bottom) for the evaporation of acetone.

apply the spray paint to the surface of the paper for a duration of 7 – 8 seconds, then allow it to dry for several minutes. In Figure 4.7 (a), we present the variation of the main peak in amplitude (top blue line) and in time delay (bottom red line). There are two notable regimes and we show their time traces in Figure 4.7 (b). The first regime (I) corresponds to the spraying process and lasts about 8 seconds. As more paint is added, the THz wave is absorbed more strongly, thus the main peak amplitude is reduced. The spray paint also possesses a larger refractive index, thereby delaying the THz pulse in time. The second regime (II) corresponds to the drying process. In the spray paint, volatile solvents such as acetone are used. As seen from Figure 4.7 (a), they evaporate very quickly, on the order of 30 seconds. The recorded THz pulse then stabilizes. In Figure 4.7 (d), we perform an averaging of 1000 pulses (100 seconds) before and after applying the spray paint. It is possible to estimate the thickness of the paint layer from the shift in time and in the peak absorption. For our sample, the thickness, as measured with a micrometer, is around 20 – 30 μm . The THz measurements of the main peak show a shift in time of 0.11 ps and an absorption of 6 %.

4.5.3 Detection and thickness evaluation of moving objects

In the final application of the FRLODL, we present the detection and thickness characterization of fast moving objects. This application intends to show the large time delay available with the FRLODL. While recording THz pulses at 24 Hz, we drop samples of low density of polyethylene (LDPE) of varying thicknesses in the path of the THz beam (Figure 4.8 (a)).

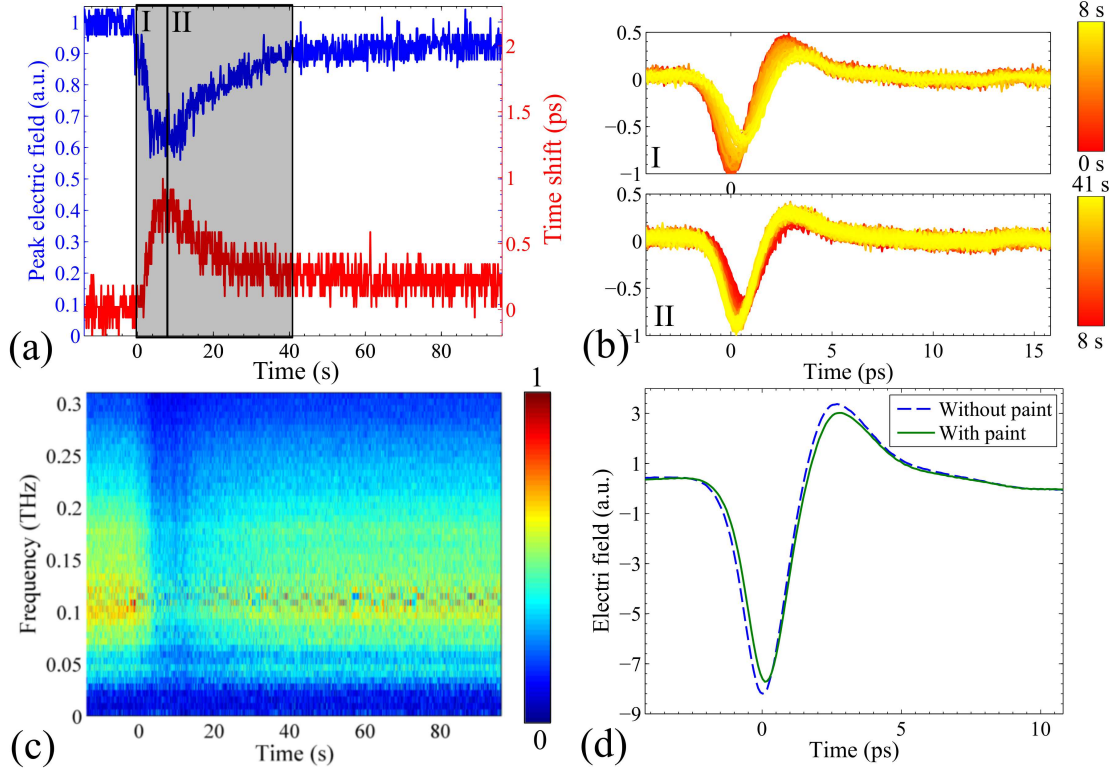


Figure 4.7 Monitoring of the painting process using the FRLODL. (a) The normalized amplitude (top blue) and time shift (bottom red) of the main THz peak along time. (b) The THz time traces during spraying (top) and drying (bottom). (c) The normalized power spectra evolution along time. (d) The averaged pulse before and after the painting process.

The samples are cylindrically shaped with a diameter of 52.5 mm. The rate of fall at the position of the THz beam is ~ 1 m/s. Figure 4.8 (b) shows the relative time position of the main peak from the beginning of the recording until the end. When the LDPE sample passes through the THz beam, the pulse experiences a retardation, resulting from the LDPE refractive index of $n = 1.513$ [119], and is shifted in time. The time delay is directly proportional to the thickness L of the sample :

$$\Delta t = \frac{L}{c_0}(n - 1) \quad (4.2)$$

where c_0 is the speed of light in vacuum. In this manner, it is possible to assess the thicknesses of the LDPE samples (see Table 4.1).

A closer look at the recorded THz traces shows how fast the acquisition is. At a constant 1 m/s rate of fall, with a FRLODL rotation speed of 24 Hz, a single recording is conducted every 41.7 mm. With a sample diameter of 52.5 mm, two acquired pulses effectively show

the passage through the LDPE (traces II and III in Figure 4.8 (c)). It is worth noticing that in our particular case, the THz beam is collimated, therefore we recorded a part of the beam passing through the sample while the other part passed through air, which explains why two peaks are observable.

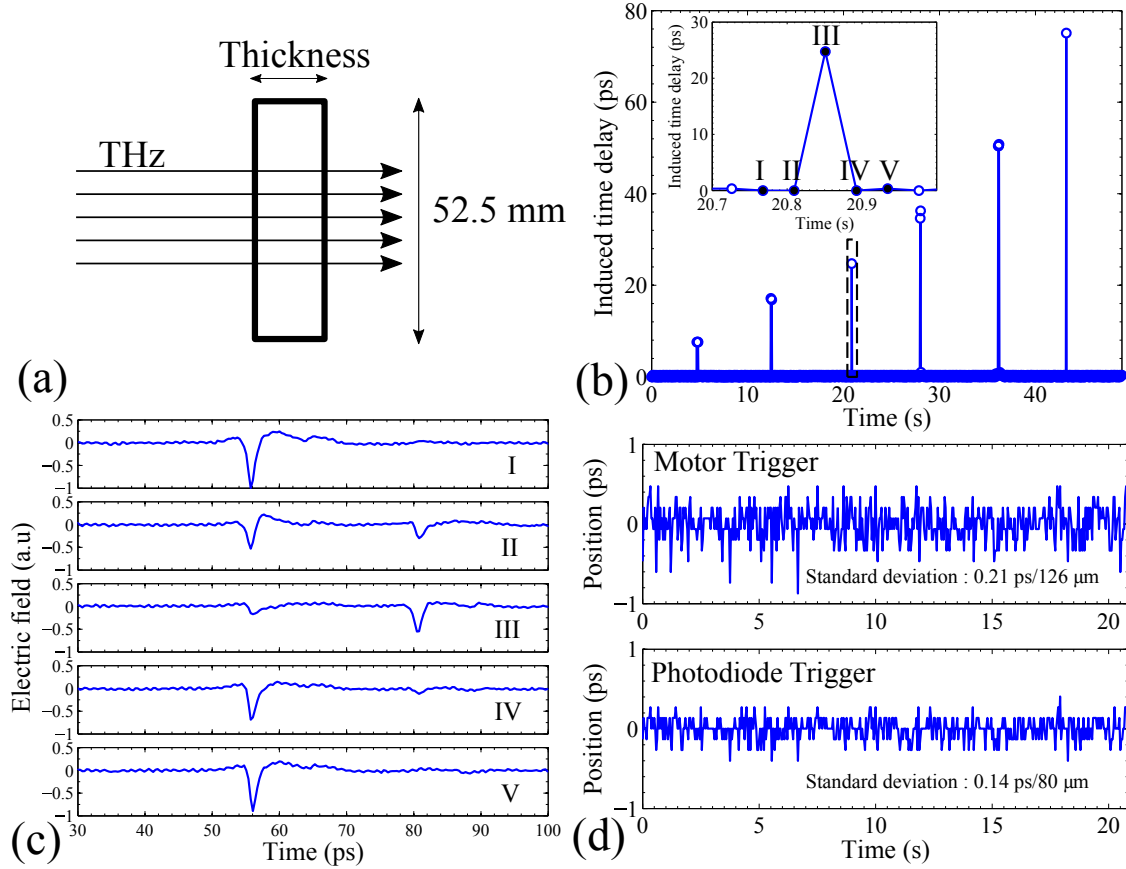


Figure 4.8 The detection of fast moving LDPE samples. (a) Experimental setup. The THz beam is collimated and the LDPE sample drops vertically. (b) The detected time delay by the passing of the LDPE samples. Inset: zoom at the passing of the 14.72 mm sample and (c) the corresponding time traces. (d) The inaccuracy of the temporal position of the peak when using the motor trigger (top) or the photodiode trigger (bottom).

Table 1 shows the assessed thickness of LDPE based upon Equation 4.2. The thickness resolution of this method is directly related to the speed of the acquisition card and the FRLODL rotation frequency. For example, if one uses a 500 kHz card, then each data point is separated by $2 \mu\text{s}$ which can be directly converted to the ps-scale using the above conversion factor. At 24 Hz, $2 \mu\text{s}$ corresponds to 0.0674 ps and, for LDPE, this is $39.4 \mu\text{m}$ from Equation 4.2. Noise arises primarily from jitter in the motor rotation. For the data acquisition to begin, it is important to have a reliable electric trigger. If one uses the electric output of the rotating motor, fluctuations in the speed of the motor can lead to different

Table 4.1 Thickness of LDPE samples assessed with micrometer and FRLODL.

Micrometer (mm)	FRLODL(mm)
4.43	4.44 ± 0.31
9.98	10.03 ± 0.31
14.56	14.46 ± 0.31
20.30	20.25 ± 0.31
29.54	29.50 ± 0.31
44.20	44.26 ± 0.31

temporal positions of the peak. To avoid this problem, we deviated a small fraction of the optical beam into a photodiode placed prior to the emitter PCA. Then, we use the electrical output of the photodiode as the trigger. This method allows the data acquisition to begin at the same time as the optical excitation of the emitter PCA thus avoiding jitter noise. At the top of Figure 4.8 (d), we show the temporal positions of the main peak when the acquisition is triggered by the motor. We simultaneously recorded the electric output of the photodiode. Then, in bottom of Figure 4.8 (d), we correct the THz pulses, by superimposing the photodiode electric outputs. By applying this method we are able to significantly reduce the jitter noise. Note that for this particular experiment, we used two channels on the acquisition card (one for the THz pulse and one for the photodiode), therefore each channel was sampled at 250 kHz and the aforementioned resolution has to be doubled. Notice also that the FWHM of the main peak is about 0.5 ps (8 data points at 24 Hz), giving an upper value for the 312 μm error. However, experimental thickness measurements show better results in most cases.

4.6 Conclusion

In summary, we demonstrated the experimental implementation of a rotary linear optical delay line. We discussed the accuracy of the FRLODL and detailed the possible sources of imprecision. The finite size of the laser beam reflected from the surface of the rotary delay line (as opposed to an optical ray) leads to its defocusing. As a result, the beam spot size on the PCA is found in the range of 6 – 20 μm with the centroid position oscillating within a ~ 70 μm range. For large gap photoconductive antennas, these oscillations will have an inconsequential influence on the generated THz signal. However, the errors coming from limited accuracy of CNC machining cause considerable variation of the THz signal amplitude as a function of the rotation angle.

In this paper, we demonstrated experimental characterization of a fast rotary optical delay

line for terahertz time-domain spectroscopy. The use of this device is greatly facilitated due to the linearity of the time delay. A simple conversion factor between the acquisition time and THz time can be used for calibration. This system has been tested at acquisition rates of up to 48 Hz per blade. In principle, four times higher speeds can be obtained when using all four blades. Ultimately, the time acquisition is limited by the electronics, in particular by the transimpedance amplifier.

Then, we showed several applications for the FRLODL. Firstly, the evaporation process of similar transparent liquids was observed, providing a way to identify each liquid by its evaporation rate. Secondly, monitoring of the painting process was demonstrated. The spraying and drying phases of the paint were clearly visible in the time traces, with a shift in both amplitude and time delay. Thirdly, we showed detection of fast moving LDPE samples. We also used the shift in time to evaluate sample thicknesses of up to 44 mm (75 ps). Jitter noise in the motor rotation was reduced by using a photodiode as an electrical trigger.

4.7 Acknowledgment

We would like to thank TeTechS Inc. for their general support of this project and their donation of the THz equipment. We would like to thank the Fonds de Recherche du Québec en Nature et Technologie (FRQNT) and the Natural Sciences and Engineering Research Council of Canada (NSERC) for funding.

CHAPTER 5 3D THz COMPUTED TOMOGRAPHY

In this chapter, we describe a 3D imaging modality performed with THz : Computed tomography (CT). First, we begin by the mathematical description of the imaging. Then, we will briefly show an experimental implementation of such a system. Several experimental challenges are discussed and, in some cases, resolved.

5.1 Principles of 3D CT

CT is a very well known imaging modality in the biomedical field [120]. The basic idea is that different images of the object are taken at several angles. This operation is known as the Radon transform. To extract an object tridimensional structure from a set of projections, one must perform what is called a back-projection reconstruction. In this section, we present the mathematical description underlying the CT imaging.

5.1.1 Radon transform

Suppose a function $f(x, y)$ describing an object that will be imaged. Let us define a new coordinate system $Ox'y'$ with an angle ϕ from the original (Figure 5.1 (a)). A projection is taken along y' and can be mathematically expressed as the integration

$$g_\phi(x') = \int_{-\infty}^{\infty} f(x, y) dy' \quad (5.1)$$

where x' represents the lateral distance from the rotation axis. To perform the integral, one needs to map the (x, y) coordinates in the projected coordinates (x', y') . Recall the rotation transformation:

$$\begin{bmatrix} x' \\ y' \end{bmatrix} = \begin{bmatrix} \cos \phi & \sin \phi \\ -\sin \phi & \cos \phi \end{bmatrix} \begin{bmatrix} x \\ y \end{bmatrix} \quad (5.2)$$

then, the Radon transform is defined as:

$$g_\phi(x') = \int_{-\infty}^{\infty} f(x' \cos \phi - y' \sin \phi, x' \sin \phi + y' \cos \phi) dy' \quad (5.3)$$

This integral is performed at a particular ϕ . If we perform the same operation for several angles, we get the sinogram $g(x', \phi)$ (Figure 5.1 (b)). This sinogram is the data that a typical

CT experiment collects. The reconstruction to get $f(x, y)$ is conducted from this sinogram. We explain this in the next section.

5.1.2 Filtered back-projection reconstruction

Let $g(x', \phi)$ be the 2D radon transform of $f(x, y)$. The filtered back-projection reconstruction is based upon the Fourier slice theorem, which links the Radon transform to the Fourier transform:

$$\tilde{g}_{1D}(x', \phi) = \tilde{f}_{2D}(x' \cos \phi, x' \sin \phi) \quad (5.4)$$

where the \sim denotes the Fourier transform and the subscripts $1D$ and $2D$ specify the dimensionality of the Fourier transform. In words, it means that the 1D Fourier transform of a projection (at angle ϕ) is a slice of the 2D Fourier transform of the image (at the same ϕ). As one can see in Figure 5.2, in the 2D Fourier transform of the image, the line that passes through the origin with an angle ϕ is the same as the 1D Fourier transform of the projection at the same ϕ .

Mathematically, let us first write the inverse Fourier transform of $\tilde{f}_{2D}(x' \cos \phi, x' \sin \phi)$ in polar coordinates:

$$f(x, y) = \int_0^{2\pi} \int_0^\infty \tilde{f}_{2D}(x' \cos \phi, x' \sin \phi) \exp(i2\pi x'(x \cos \phi + y \sin \phi)) x' dx' d\phi \quad (5.5)$$

Then, we can use the Fourier slice theorem (Equation 5.4) to rewrite:

$$\begin{aligned} f(x, y) &= \int_0^{2\pi} \int_0^\infty \tilde{g}_{1D}(x', \phi) \exp(i2\pi x'(x \cos \phi + y \sin \phi)) x' dx' d\phi \\ &= \int_0^\pi \left[\int_{-\infty}^\infty |x'| \tilde{g}_{1D}(x', \phi) \exp(i2\pi x'(x \cos \phi + y \sin \phi)) dx' \right] d\phi \end{aligned} \quad (5.6)$$

where the last step is possible because of the symmetry of the operation.

In Equation 5.6, the outer integral represents the summation over all the angles. The inner integral can be seen as the 1D inverse Fourier transform of the product of the Fourier transform of $g(x', \phi)$ by $|x'|$. Here, $|x'|$ acts essentially as a filter. Thus, this operation is known as a *filtered* back-projection. Precisely, the filter $|x'|$ is a high-pass filter. Therefore, in experimental conditions, it will enhance the high frequency noise. Thus, combination of $|x'|$ with other filters is used to overcome the noise : Hann or Hamming window for instance.

In short, the filtered back-projection algorithm involves essentially five steps: 1) Collection

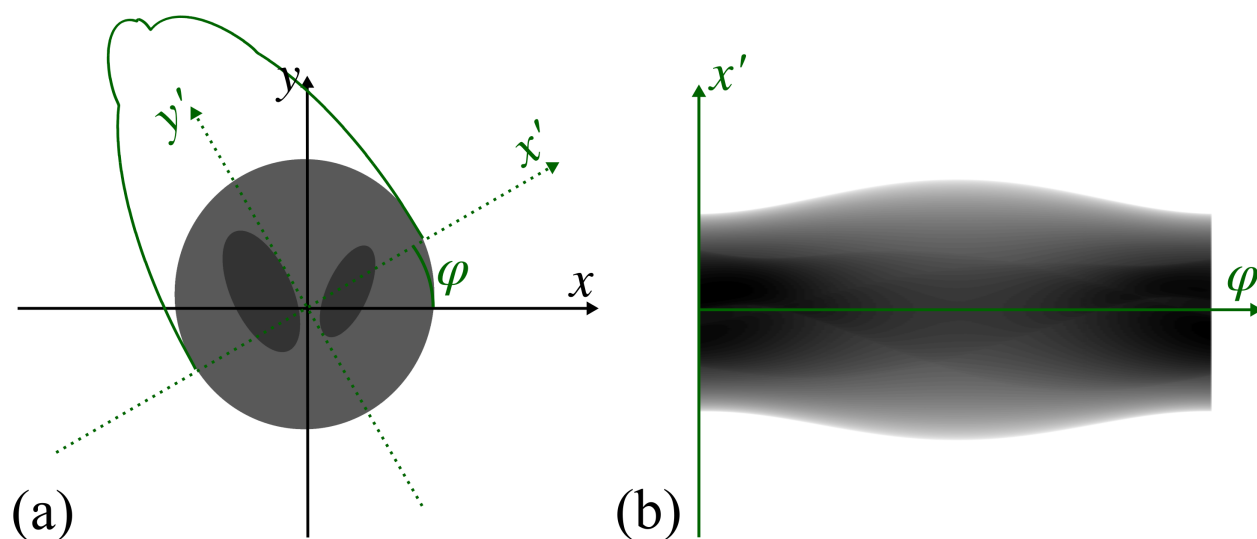


Figure 5.1 Principles of Radon transform. (a) Line integral projection at angle ϕ along x' , performed in the direction of the y' axis. (b) Collection of all the projections results in a sinogram $g(x', \phi)$.

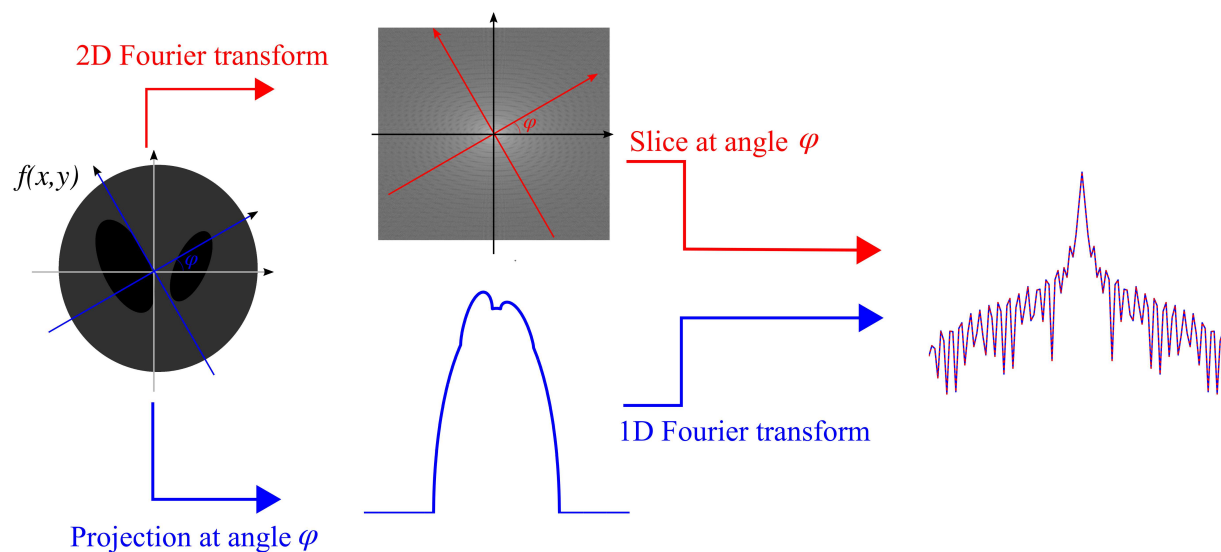


Figure 5.2 Visual explanation of the Fourier slice theorem.

of projections at the angles from 0 to π , 2) Fourier transform on each projection, 3) Multiplication by a specific filter, 4) Inverse Fourier transform and 5) Summation over the angles. In Matlab, the filtered back-projection algorithm is already implemented in the *iradon* function and it gives the possibility to chose from several filters [121]. We use this function below.

5.2 3D CT in THz

Yet, we have not discussed about the nature of $f(x, y)$. In X-ray CT, only the intensity is recorded. Therefore, $f(x, y)$ can be considered as the attenuation coefficient $\mu(x, y)$. In a body, each tissue has its own attenuation coefficient (see for example [122]). Sometimes, contrast agents are even used to provide the necessary image clarity. In THz-TDS, both the electric field and the phase are recorded at the same time, and at different frequencies. This provide a brand new way to interrogate the structure and the *nature* of the imaged material. A simple way to construct $f(x, y)$ has been introduced in early work on THz CT [123, 124]. Suppose a set of multiple pulses recorded for different rotation angles ϕ and x' positions. By considering the Fourier transform of each pulse, the detected THz signal can be approximated as the following line integral :

$$E_d(\omega, \phi, x') = E_0(\omega) \exp \left[\int_{-\infty}^{\infty} \frac{-i\omega}{c} \hat{n}(\omega, y') dy' \right] \quad (5.7)$$

where E_d and E_0 are the Fourier transforms of the detected and incident THz electric field respectively. $\hat{n}(\omega, y')$ is the complex refractive index of the sample :

$$\hat{n}(\omega, y') = n_r(\omega, y') + in_i(\omega, y') \quad (5.8)$$

with n_r the real refractive index and $n_i = \alpha c/2\omega$ the extinction coefficient linked to the absorption α . By measuring the complex electric field, we can divide the solution in its magnitude and phase components:

$$\begin{aligned} \Gamma_n &= \int_{-\infty}^{\infty} n_r(\omega, y') dy' = \frac{c}{\omega} \angle \left(\frac{E_d}{E_0} \right) \\ \Gamma_\alpha &= \int_{-\infty}^{\infty} \alpha(\omega, y') dy' = 2 \ln \left| \frac{E_d}{E_0} \right| \end{aligned} \quad (5.9)$$

with \angle and $||$ the operators for the phase and the magnitude respectively. We note that this reconstruction technique assumes that the beam is parallel. Already, more advanced work has been performed to take in account a more realistic propagation behavior of the THz beam [125, 126].

5.3 Implementation of THz CT imaging

In this section, we discuss about the practical implementation of a 3D CT imaging in a THz-TDS system. As we will see, some technical problems need to be overcome in order to realize proper images.

5.3.1 Technical issues

First, in medical X-ray, the source and the detector move around the body of the patient to collect data at different angles. Obviously, in THz, this cannot be performed since the setup is quite bulky. Instead, it is the sample that we rotate.

Second, in X-ray, the beam is practically parallel since the wavelength is in the \sim nm scale. In THz however, to be able to have a good lateral resolution, the beam needs to be focused. At 1 THz, a Gaussian beam focused in a 1 mm spot, results in a Rayleigh range¹ of \sim 1 cm. This means that the axial size of the sample must be in the cm scale, which is problematic for big samples. This issue was already pointed out in [125, 126] where the propagation behavior of the THz beam is taken in account in the reconstruction algorithm.

Third, in X-ray multiple detectors are used at the same time, resulting in a faster complete scanning. For a 3D reconstruction, the previously described filtered back-projection needs to collect 2D images at sufficient angles. As this would take literally days to collect in THz, in the following demonstration, we performed only a 2D reconstruction. Interestingly, in [127], by spatially spreading the time pulse, the authors were able to reduce the total time to 6 minutes.

5.3.2 Fast acquisition and correction for THz CT imaging

Early when implementing THz CT imaging, we observed the need to have a fast acquisition time. The first measurements were performed by manually rotating and moving the sample, resulting in one week of acquisition time. In a later implementation, we used an automated x' lateral positioning. This allowed to reduce the acquisition time to two full days. However, the pulse recording was still taking the most important time (\sim 2 min per pulse). Moreover, in strongly absorbing materials it is necessary to average several pulses to get appropriate signal-to-noise ratios.

To overcome the pulse acquisition time issue, we implemented a new way to record the pulse

¹For a Gaussian beam, the Rayleigh range corresponds to the distance along the propagation axis for which the area of the cross-section is twice the minimal waist.

with the use of the lock-in amplifier and an acquisition card. It is necessary to understand that, previously, the acquisition program instructed the delay line to move to each specified step. The phase and amplitude were then recorded at each one of them. This method was highly time-consuming. Our new program instructs to directly move to the maximal specified step. The recording of the phase and amplitude is performed with the acquisition card at the same time as the movement. With this type of program, one pulse is acquired in ~ 5 seconds. This way, we were able to reduce the time acquisition to ~ 4 hours. However, some post-corrections are needed to get appropriate results.

First, the acquisition card and the high sampling rate that we use introduce noise in the acquired pulse (blue in Figure 5.3). However, this noise is located at high frequencies in the spectrum (between 2 and 2.5 kHz on Figure 5.3 (b)). Therefore, to remove the noise, we simply Fourier transform the pulse, then set the values above 2 kHz to zero and perform an inverse Fourier transform (red in Figure 5.3).

Second, there is a desynchronization between the start of the delay line movement and the acquiring of the signal. Therefore, the averaging of multiple pulses will not be satisfactory (Figure 5.4 (a)). To counter this, we used a cross-correlation algorithm to superimpose the different pulses. Note that there is an imprecision on the position of the pulse. Yry, this position is useful if one wants to deduce the refractive index of the sample for example. This uncertainty is reduced by taking the average position of all the pulses (Figure 5.4 (b)).

Finally, we still need to pass from the ms-time scale to the ps-time scale. Indeed, in Figures 5.3 and 5.4, the time scale corresponds to the acquisition time. To find the ps-scale, we use the positions of the water absorption lines. This assumes that the delay line moves at a constant speed around the position of the THz pulse.

In Figure 5.5, the fully corrected pulse is presented. High frequencies have been removed, multiple pulses have been superimposed and a average of them has been taken. Moreover, the time and frequency scale have been adjusted to the ps and THz scales respectively.

5.4 Reconstruction

In this section, we present the first CT imaging performed in our THz-TDS system. As a sample we used a LDPE rod with a diameter of 25.4 mm and three holes of 6.35 mm (Figure 5.6). The rod is placed vertically in the system, in the y direction. The scanning is performed along x and the sample is rotated by ϕ around the y axis. Specifically, the x step is 0.5 mm and the ϕ step is 10° . Because of the vertical symmetry of the sample, with this sampling, we should be able to image the crossection of the sample (as in Figure 5.6 (a))

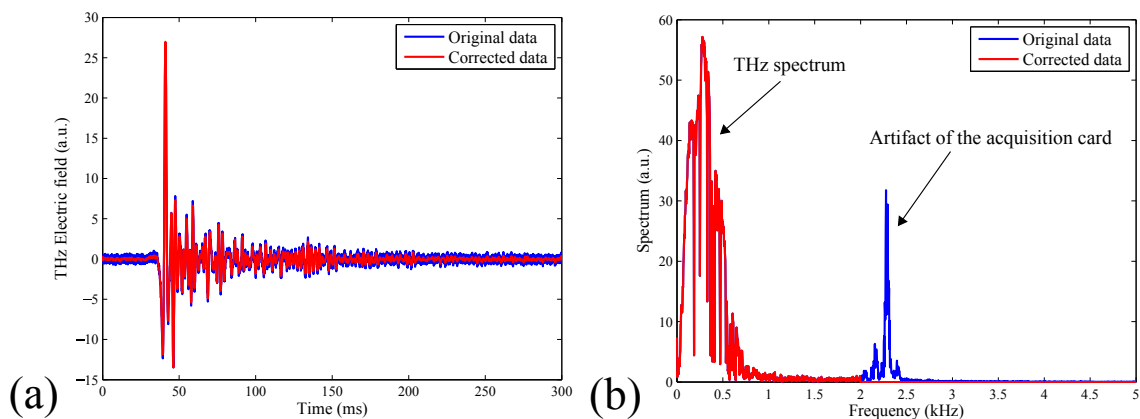


Figure 5.3 Removal of high frequencies in the acquired data. (a) Electric field and (b) spectrum of one THz pulse before (blue) and after (red) the correction.

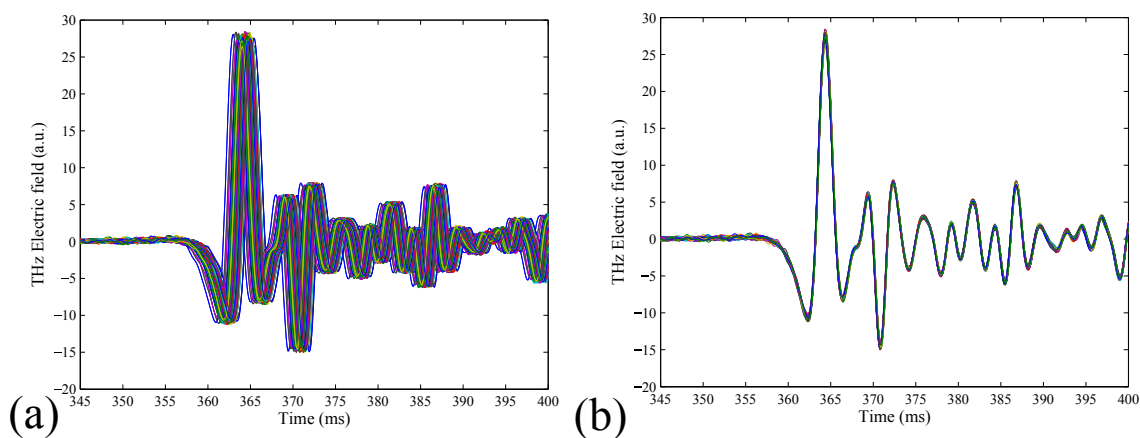


Figure 5.4 Superimposition of multiple pulses. A hundred electric fields (a) before and (b) after the correction.

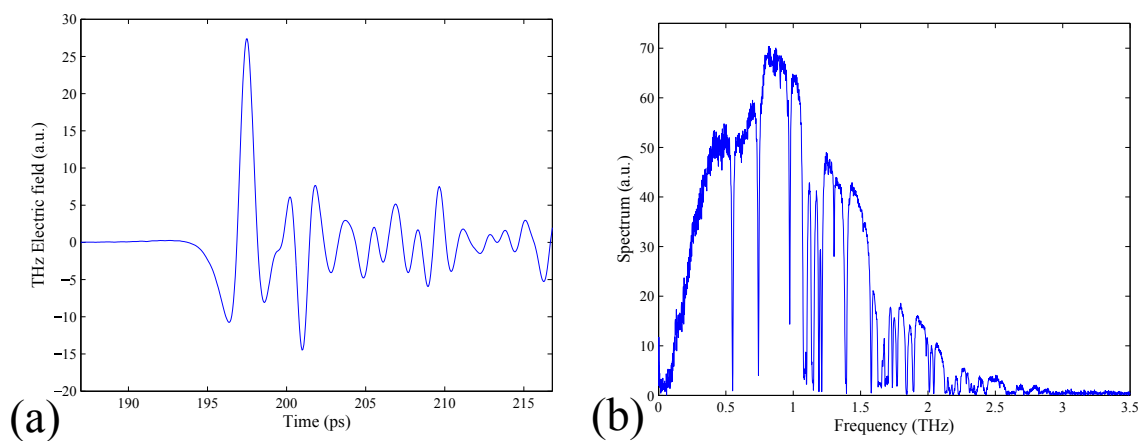


Figure 5.5 Fully corrected pulse. (a) Electric field and (b) spectrum.

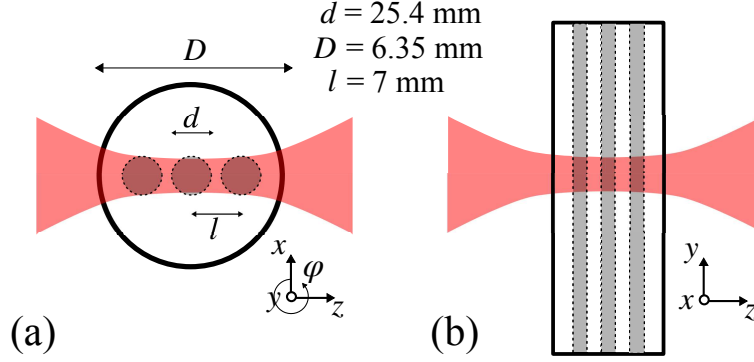


Figure 5.6 The configuration of the LDPE rod with three holes in the THz-TDS system in (a) a top (b) and lateral view. Note that the beam waist is not at scale compared to the size of the holes.

In Figure 5.7, we present the ratio Γ_α for different frequencies. In Figure 5.7 (a)-(d), we show the measured sinogram and in Figure 5.7 (e)-(h) the filtered back-projection for each sinogram. As it is possible to see, by increasing the frequency, finer details can be seen in the sinogram, at the expense, however, of the signal-to-noise ratio. In the filtered back-projection images, the three holes cannot be distinguished.

To reduce the effect of the noise in the reconstruction, we average the sinogram on different frequency bands. In Figure 5.7 (i)-(k), the sinogram is smoother. This leads to a smoother reconstruction in Figure 5.7 (l)-(n). However, the three holes are still not distinguishable.

To further analyze the problems in our imaging, in Figure 5.7 (o), we plot the ideal structure. Then, in Figure 5.7 (p), we compute the Radon transform with the Matlab *radon* function.

The fine structure in the middle part of the sinogram is the most difficult to obtain experimentally. There, the projection is not able to distinguish the three holes. This can be explained by the fact that the THz beam waist is too large compared to the wall between two holes. This wall measures 0.65 mm whereas the beam waist is estimated to be ~ 1 mm. In fact, the beam waist needs to be characterized better, with a knife-edge technique for instance [128].

Also, the noise in the measured sinogram is still very high. To compensate for this, we need to average more pulses. However, this will increase the total scanning time. This is why, it is important to optimize the scanning system.

Plus, a decrease of the angular step in the measurements could positively impact the reconstruction. Again, this will increase the total time acquisition. Adding a electro-mechanical angular positioning stage can greatly help.

Finally, in Figure 5.7 (p), the sinogram has a perfectly horizontal outline whereas in our measurements the shape has a small vertical deviation. This is explained by the fact that in our measurements the rotation axis is not perfectly in the middle of the sample.

To conclude, we want to state that 3D CT is possible in THz as it was demonstrated by other groups. However, a number of hurdles must be overcome. Most notably, the time acquisition is a major issue.

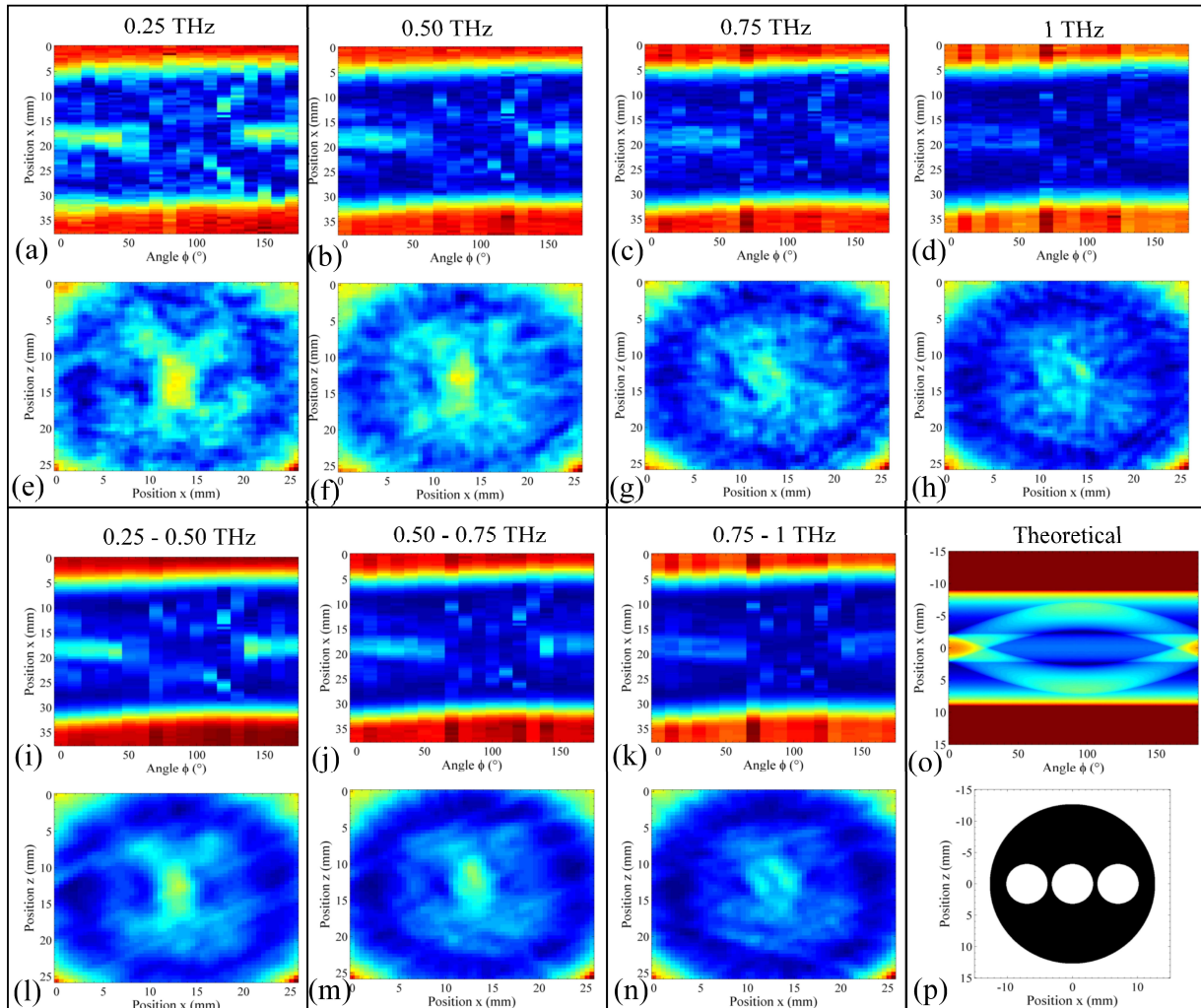


Figure 5.7 (a)-(d) Sinograms at different frequencies : (a) 0.25, (b) 0.50, (c) 0.75 and (d) 1 THz. (e)-(f) Corresponding filtered back-projections : (e) 0.25, (f) 0.50, (g) 0.75 and (h) 1 THz. (i)-(k) Averaged sinograms on the (i) 0.25 – 0.50 THz band, (j) 0.50 – 0.75 THz band and (k) 0.75 – 1 THz band. Corresponding filtered back-projections : (l) 0.25 – 0.50 THz band, (m) 0.50 – 0.75 THz band and (n) 0.75 – 1 THz band. (o) Simulated LDPE rod with three holes and (p) its Radon transform

CHAPTER 6 GENERAL DISCUSSION

In this chapter, we discuss general considerations about the previous sections. First, we present THz characterization of polyurethane foam. Then, we show silk foam fiber SEM images. We discuss also about the trigger operation for the fast rotary delay line. Finally, we briefly comment on the integration of the waveguide and the rotary delay line in a THz CT imaging system.

6.1 Polyurethane foam as a THz waveguide

In Chapter 2, we presented a two-wire waveguide with a polystyrene foam cladding. As a proof of concept, we pressed two slabs of polystyrene foam against the two wires. Ideally, the two wires are included in the foam structure during its fabrication. However, the production of polystyrene foam from expandable polystyrene beads requires complex machining. Nevertheless, we explored another type of dielectric foam, the polyurethane foam.

Different types of polyurethane exists and we use one intended for thermal isolation. The fabrication involves two solutions denoted A and B. When the two solutions are mixed in a 1 : 1 ratio, the molecules polymerize to form long chains of polyurethane. At the same time, water decomposes to produce carbone dioxide which acts as a blowing agent and causes the polyurethane to expand [129].

To explore the ability of polyurethane foam to encapsulate the two-wire waveguide, we need first to characterize its bulk behavior in the THz region. For that, we mix 80 mL of solutions A and B in a cylindrical 2 L plastic bottle. Then, we cut different parts of polyurethane foam and introduce them in the THz-TDS system. Using the same procedure as Section 2.2.1, we record the time traces for different lengths of polyurethane foams and we compute the Fourier transform amplitude and phase (Figure 6.1). As it is possible to see, the high THz frequencies (above 0.9 THz) are completely lost after 27.8 mm. This has to be compared with the polystyrene foam where frequencies up to 1.75 THz are still present even after 152.4 mm (Figure 2.1).

Now, using Equations ??, we calculate the refractive index and the losses of polyurethane foam (Figure 6.2). Note that the values above 0.45 THz should be viewed cautiously since the transmission spectrum shows poor signal-to-noise ratio there. Nevertheless, we find a slightly increasing refractive index around 1.021, which is again understandable by the high porosity of the sample. Below 0.45 THz, the losses follow a polynomial function and are

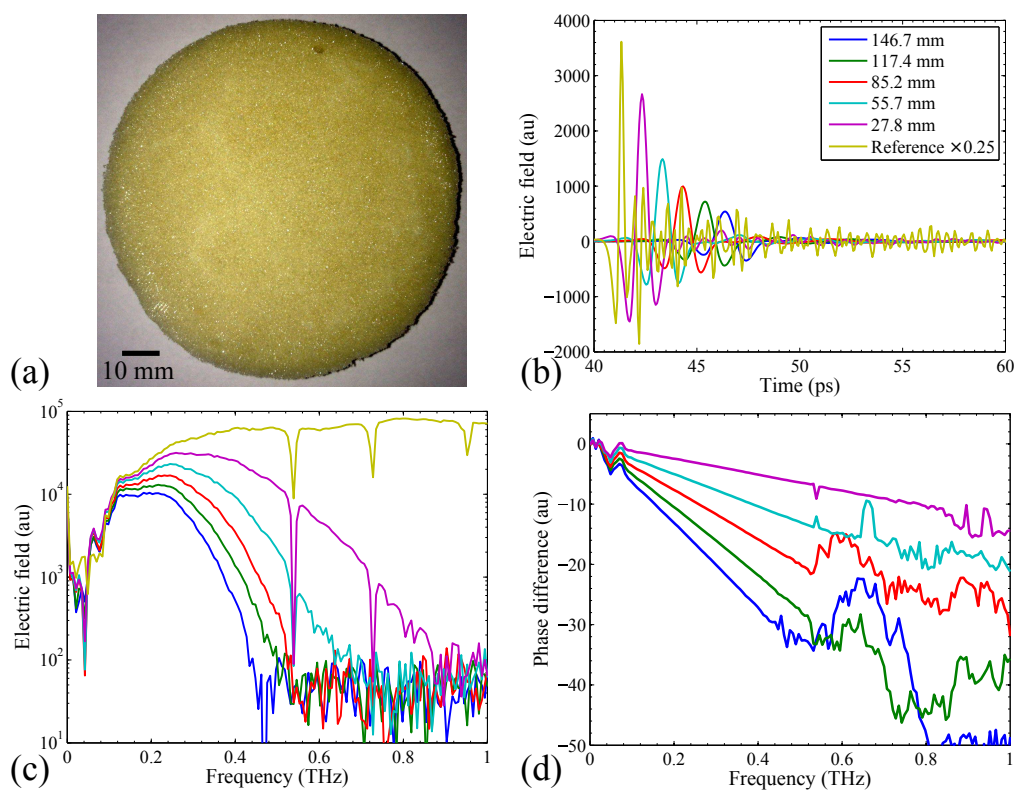


Figure 6.1 (a) Photograph of the polyurethane foam. Diameter is 95 mm. (b) Time-domain electric field of the cutback measurement for different lengths of polyurethane foam. The reference corresponds to the measurement in an empty THz-TDS system. It has been multiplied by 0.25 for clarity. (c) Transmission spectra. (d) Unwrapped phase relative to reference.

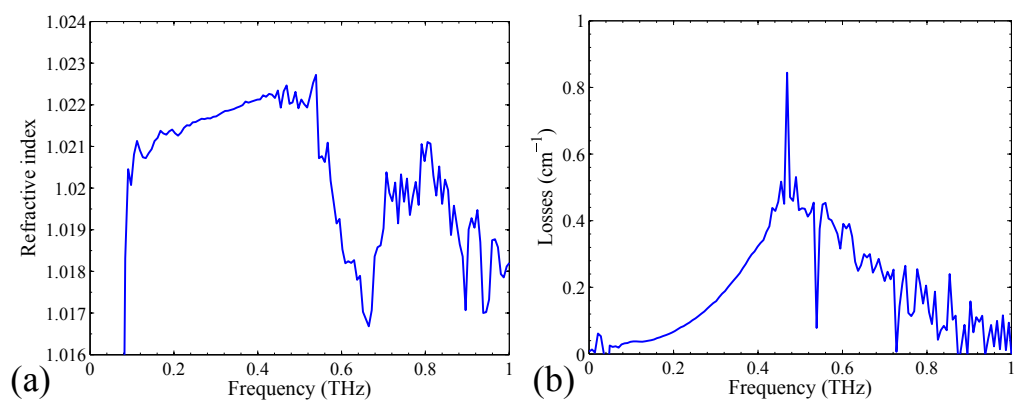


Figure 6.2 (a) Refractive index and (b) losses of polyurethane foam.

stronger than the polystyrene foam losses (compare with Figure 2.2).

Because of these results, we did not continue with enclosing the two-wire waveguide in the polyurethane foam. However, a variety of other foams are available [130]. For future research, two directions are possible. One could contact polystyrene foam manufacturers to explore the possibility to directly introduce the two wires during the expanding. Also, one could characterize new foams in the THz region. The goal is to find a foam that presents low losses and in which it is easy to include the two wires during the fabrication.

6.2 Silk foam terahertz waveguides

In Chapter 3, we presented a novel kind of material to guide the THz, the silk foam. Here, we address particular points that were not mentioned in the publication.

SEM images of the silk sample reveals a very unique structure. Some pictures of the bulk silk foam were presented in Figure 3.1. Here, we would like to extend the presentation to pictures of the fiber silk foam (Figure 6.3).

Unlike the bulk silk foam, the structure in the fiber silk foam is less radially ordered. As we already explained in the paper, we believe that the radial order is caused by the freezing dynamics. These dynamics may be less important in the fiber silk foam because of its size. As one can see in Figure 6.3, the microstructure is a combination of flat $\sim 10 \mu\text{m}$ walls and circular holes with diameters of $\sim 100 \mu\text{m}$.

We would like to stress that the silk foam has other relevant biomedical applications than strict waveguiding. The structure of the silk foam is highly porous. In our samples, we found a porosity of 94%. Plus, the SEM images show that the surface to volume ratio is very high. This property already drew attention of researchers in the field of tissue engineering (see for example [131]). There, for the cells to reproduce and mimic the tissue, they need a 3D biological substrate. Our contribution was to show that silk foam is transparent to THz. At the same time, water contained in the cells absorbs significantly the THz. It is therefore possible to assess the cell concentration in a particular silk foam. This is especially relevant in tissue engineering where this concentration reveals the success or not of a particular organ reconstruction for example.

6.3 Trigger for fast rotary delay line

In this section, we discuss about the trigger operation in the fast rotary delay line. In the setup depicted in Figure 4.4, we added a photodiode prior to the emission antenna to trigger

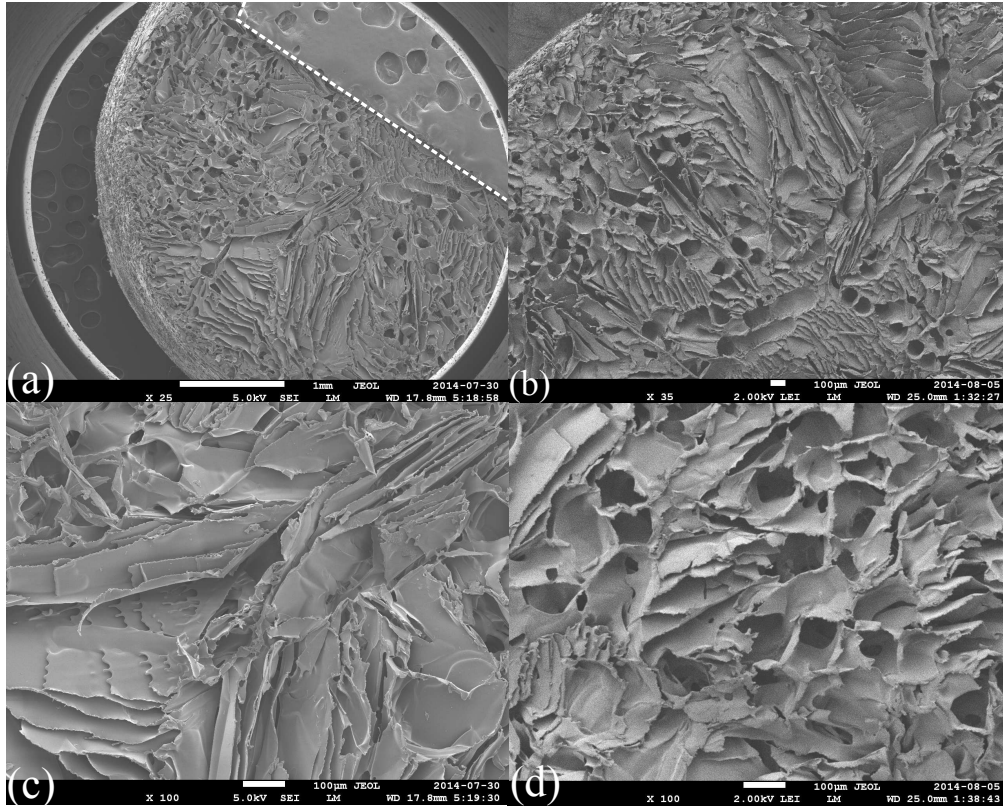


Figure 6.3 SEM images of the fiber silk foam. (a) Low magnification revealing the macrostructure. The dotted line indicates the position of the tape used to hold the sample. (b) Periphery of the sample. (c) Higher magnifications showing the flat walls and (d) the circular holes.

the data acquisition. At the end of Section 4.5.3, we briefly state that the use of the electric output of the rotating motor leads to an inaccuracy on the temporal position of the peak (see Figure 4.8(d)). Here, we would like to further comment on this.

The electrical output of the rotation motor is a step function (Figure 6.4 (a)). The passing of 500 square pulses corresponds to a complete rotation of the motor. Therefore, by counting them, we can generate a trigger. For that, we use the electric circuit schematically shown in Figure 6.4. First, with an operational amplifier, we saturate the signal so that it spans from 0 to 1 V (Figure 6.4 (b)). Then, we use three electronic logical counters placed in series. These counters will successively output a logical step from pin 1 to pin 10. Connecting the pin 10 to the clock input of a second electronic counter will allow the counting of tens. By doing the same with a third electronic counter, hundreds can be count. In this way, pin 5 of the last counter corresponds to a full turn and its output is the trigger for data acquisition. However, as we already saw in Figure 4.8 (d), compared to the photodiode trigger, the motor trigger provides less repeatability. Indeed, the position of the main peak fluctuates in time

from one measurement to another. This is explained by the fact that one full rotation is divided in only 500 steps. At the same time, the photodiode outputs a voltage strictly when the optical pulse hits it. This avoids the jitter noise, which is defined as a deviation from the periodic rotation of the motor.

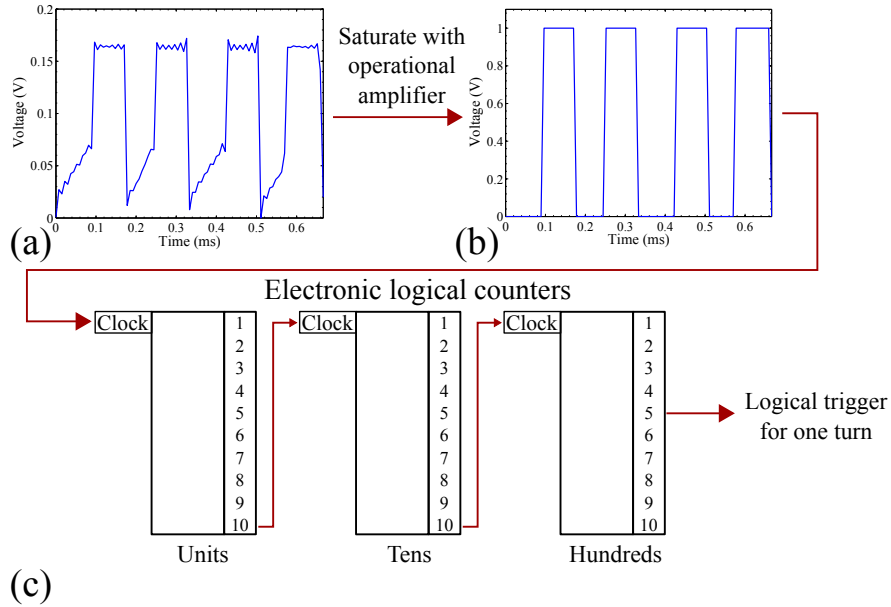


Figure 6.4 Generation of the trigger based on the electrical output of the rotation motor. (a) Raw electrical output of the motor. (b) Saturated signal. (c) Electronic logical counters stage.

6.4 Waveguide and rotary delay line in a THz CT imaging system

In this last section, we briefly discuss on the possibility of assembling together the different parts covered in this thesis for the CT imaging application.

First, the THz waveguide can be used for imaging [132]. We saw that for THz CT imaging, it is easier to rotate the sample than the emitter and the detector. This is due to the cumbersome THz-TDS instrumentation. However, large samples cannot be rotated. For them, THz waveguides could help guide the THz light around.

Second, the work performed on CT imaging showed that it is important to have a fast acquisition scheme. In Chapter 4, we precisely demonstrated a fast rotary delay line that can provide acquisition speeds of several Hz. Then, for CT imaging, the scanning of the sample will be limiting the overall acquisition time. Also, complex correction algorithms would be needed to overcome synchronization issues for a continuous scan [133].

CONCLUSION

Summary of results

Within this thesis, we have explored solutions to two current problems in THz-TDS instrumentation : the THz beam handling and the long acquisition time. We have also presented a practical implementation of a THz CT imaging, based on the THz-TDS system.

The first issue is the THz beam handling. As we saw, the THz-TDS system is cumbersome and, in many applications, it is desirable to have a stand-off distance between the THz source and the sample. A solution would be to have a waveguide able of transporting it. For that, our contribution was to study foam waveguides.

First, we explored polystyrene foam as a dielectric material for waveguiding. We confirmed that it has very low losses and refractive index close to 1 in THz. This was explained by the fact that most of it was made of gas. Then, we used it to enclose the two-wire waveguide. By comparing the propagation of the THz with and without the polystyrene foam, we concluded that the polystyrene foam has little effect, both in losses and in dispersion.

Second, we studied an exotic biological foam material : the silk foam. From a purified silk solution, we fabricated bulk and fiber silk foam through lyophilisation and casting techniques. The refractive index was found to be very close to that of air. This is explained by the porous nature of the silk foam. The silk foam losses scale quadratically with frequency and are one order of magnitude smaller than those of solid silk. Also, we studied a 10 cm long, 5 mm diameter step-index THz fiber. We showed that this waveguide operates in a single mode regime and modal group velocity dispersion is very small.

The second issue is the long time acquisition. Its main cause is the linear micropositioning stage in the standard THz-TDS system. Mechanically, a rotary movement can achieve high speeds. Previously, our group showed curvilinear reflective surfaces that provide a linear delay with the rotation. Within this thesis, we experimentally implemented a rotary optical delay line. With a CNC machine, we fabricated four surfaces on the same blade. Rotation speeds of up to 48 Hz were tested, corresponding to an acquisition rate of up to 192 Hz if the four blades were used. The imprecision on the pulse reconstruction was mainly attributed to the CNC machining. Also, by increasing the rotation speed, we observed a decrease in the THz bandwidth, due to the limitations in the electronics, specifically the transimpedance amplifier. Finally, novel applications for THz were shown. First, we observed the evaporation process of three optically transparent liquids, providing a non-contact method to identify each

one by its evaporation rate. Second, we monitored the painting process of a red enamel spray paint. The spraying and drying phases were clearly visible in the time traces, with a shift in both amplitude and time delay. Third, we demonstrated detection and thickness evaluation of up to 44 mm low density polyethylene samples.

The third part of this thesis was dedicated to the practical implementation of THz CT imaging. The THz-TDS offers several advantages such as multifrequency imaging and direct extraction of complex refractive index. However, when doing CT imaging on a THz-TDS system, several challenges arise, the main one being the time acquisition. Within this thesis, we did not have the time to use the rotary delay line that we previously characterized. Rather, we modified the acquisition technique in order to accelerate it from the minute scale to the second scale. However, the first CT images were not able to reproduce the fine structure in a perforated LDPE rod. We suspect the large THz beam waist and the low signal-to-noise ratio for that.

Limitations and future research directions

The overall objectives presented in the introduction were generally fulfilled in this thesis. Some particular limitations remain and they pave the way to future research.

The foam waveguides that we have developed are prototypes. In this research, two slabs of polystyrene foam were pressed against the two wires. Ideally, the two wires are directly included during the polystyrene foam fabrication. For the silk foam, we studied its THz properties and explored the possibility to use it as a THz waveguide. However, it is also possible to use it to develop a THz biomedical sensor.

Regarding the fast rotary delay line, the machining can be improved. We observed that the THz pulse was modified depending on the rotation angle, meaning that the CNC manufacturing produced an irregular surface. In fact, optical surfaces with rugosity below the wavelength are achievable with specific fabrication techniques. Also, in our prototype, we were able to put four surfaces on the same blade. It is possible to add even more surfaces to reach higher speeds.

For the THz CT imaging, work is still needed to achieve a suitable image. The noise is still very high. To reduce it, one could average more, at the expense of the acquisition time however. Implementing the fast rotary delay line with the THz CT imaging system could help decrease the total scanning time. Also, we saw that the THz beam waist may be too large. To test this hypothesis, it is necessary to perform a knife-edge measurement to get the frequency dependence shape of the beam.

REFERENCES

- [1] J.-H. Son, Ed., *Terahertz Biomedical Science and Technology*. IOP Publishing, 2014.
- [2] P. C. Ashworth, E. Pickwell-MacPherson, E. Provenzano, S. E. Pinder, A. D. Purushotham, M. Pepper, and V. P. Wallace, “Terahertz pulsed spectroscopy of freshly excised human breast cancer,” *Optics Express*, vol. 17, no. 15, pp. 12 444–12 454, 2009.
- [3] R. M. Woodward, B. E. Cole, V. P. Wallace, R. J. Pye, D. D. Arnone, E. H. Linfield, and M. Pepper, “Terahertz pulse imaging in reflection geometry of human skin cancer and skin tissue,” *Physics in Medicine and Biology*, vol. 47, no. 21, p. 3853–3863, 2002.
- [4] Y. C. Sim, J. Y. Park, K.-M. Ahn, C. Park, and J.-H. Son, “Terahertz imaging of excised oral cancer at frozen temperature,” *Biomedical Optics Express*, vol. 4, no. 8, p. 1413–1421, 2013.
- [5] J. Xu, K. W. Plaxco, and S. J. Allen, “Probing the collective vibrational dynamics of a protein in liquid water by terahertz absorption spectroscopy,” *Protein Science*, vol. 15, no. 5, pp. 1175–1181, 2006.
- [6] Z.-P. Zheng, W.-H. Fan, Y.-Q. Liang, and H. Yan, “Application of terahertz spectroscopy and molecular modeling in isomers investigation: glucose and fructose,” *Optics Communications*, vol. 285, no. 7, pp. 1868–1871, 2012.
- [7] A. J. Fitzgerald, B. E. Cole, and P. F. Taday, “Nondestructive analysis of tablet coating thicknesses using terahertz pulsed imaging,” *Journal of Pharmaceutical Sciences*, vol. 94, no. 1, pp. 177–183, 2005.
- [8] C. J. Strachan, P. F. Taday, D. A. Newnham, K. C. Gordon, J. A. Zeitler, M. Pepper, and T. Rades, “Using terahertz pulsed spectroscopy to quantify pharmaceutical polymorphism and crystallinity,” *Journal of Pharmaceutical Sciences*, vol. 94, no. 4, pp. 837–846, 2005.
- [9] J. A. Zeitler and Y.-C. Shen, *Terahertz Spectroscopy and Imaging*. Springer, 2013, ch. Industrial applications of terahertz imaging, pp. 451–489.
- [10] R. K. May, M. J. Evans, S. Zhong, I. Warr, L. F. Gladden, Y. Shen, and J. A. Zeitler, “Terahertz in-line sensor for direct coating thickness measurement of individual tablets during film coating in real-time,” *Journal of Pharmaceutical Sciences*, vol. 100, no. 4, pp. 1535–1544, 2010.

- [11] K. Yamamoto, M. Yamaguchi, M. Tani, M. Hangyo, S. Teramura, T. Isu, and N. Tomita, “Degradation diagnosis of ultrahigh-molecular weight polyethylene with terahertz-time-domain spectroscopy,” *Applied Physics Letters*, vol. 85, no. 22, pp. 5194–5196, 2004.
- [12] N. Krumbholz, T. Hochrein, N. Vieweg, T. Hasek, K. Kretschmer, M. Bastian, M. Mikulics, and M. Koch, “Monitoring polymeric compounding processes inline with THz time-domain spectroscopy,” *Polymer Testing*, vol. 28, no. 1, pp. 30–35, 2009.
- [13] C. Jordens and M. Koch, “Detection of foreign bodies in chocolate with pulsed terahertz spectroscopy,” *Optical Engineering*, vol. 47, no. 3, p. 037003, 2008.
- [14] P. Parasoglou, E. P. J. Parrott, J. A. Zeitler, J. Rasburn, H. Powell, L. F. Gladden, and M. L. Johns, “Quantitative water content measurements in food wafers using terahertz radiation,” *Terahertz Science and Technology*, vol. 3, no. 4, pp. 172–182, 2010.
- [15] J. M. Chin, V. Narang, X. Zhao, M. Y. Tay, A. Phoa, V. Ravikumar, L. H. Ei, S. H. Lim, C. W. Teo, S. Zulkifli, M. C. Ong, and M. C. Tan, “Fault isolation in semiconductor product, process, physical and package failure analysis: Importance and overview,” *Microelectronics Reliability*, vol. 51, no. 9-11, pp. 1440–1448, 2011.
- [16] L. Tian, Q. Zhou, B. Jin, K. Zhao, S. Zhao, Y. Shi, and C. Zhang, “Optical property and spectroscopy studies on the selected lubricating oil in the terahertz range,” *Science in China Series G: Physics, Mechanics and Astronomy*, vol. 52, no. 12, pp. 1938–1943, 2009.
- [17] P. Mousavi, F. Haran, D. Jez, F. Santosa, and J. S. Dodge, “Simultaneous composition and thickness measurement of paper using terahertz time-domain spectroscopy,” *Applied Optics*, vol. 48, no. 33, pp. 6541–6546, 2009.
- [18] M. Girard and M. Skorobogatiy, “Integrated terahertz multiparameter sensors using fiber/frequency selective surface couplers,” *Journal of Optics*, vol. 16, no. 9, p. 094007, 2014.
- [19] K. Fukunaga and M. Picollo, “Terahertz spectroscopy applied to the analysis of artists’ materials,” *Applied Physics A*, vol. 100, no. 3, pp. 591–597, 2010.
- [20] Y. C. Shen, T. Lo, P. F. Taday, B. E. Cole, W. R. Tribe, and M. C. Kemp, “Detection and identification of explosives using terahertz pulsed spectroscopic imaging,” *Applied Physics Letters*, vol. 86, no. 24, p. 241116, 2005.

- [21] D. Zimdars, J. A. Valdmanis, J. S. White, G. Stuk, S. Williamson, W. P. Winfree, and E. I. Madaras, “Technology and applications of terahertz imaging non-destructive examination: Inspection of space shuttle sprayed on foam insulation,” in *AIP Conference Proceedings*, vol. 760, no. 1, 2005, pp. 570–577.
- [22] T. Kleine-Ostmann and T. Nagatsuma, “A review on terahertz communications research,” *Journal of Infrared, Millimeter, and Terahertz Waves*, vol. 32, no. 2, pp. 143–171, 2011.
- [23] A. Markov, H. Guerboukha, and M. Skorobogatiy, “Hybrid metal wire–dielectric terahertz waveguides: challenges and opportunities,” *Journal of the Optical Society of America B*, vol. 31, no. 11, pp. 2587–2600, 2014.
- [24] H. Guerboukha, G. Yan, O. Skorobogata, and M. Skorobogatiy, “Silk foam terahertz waveguides,” *Advanced Optical Materials*, vol. 2, no. 12, pp. 1181–1192, 2014.
- [25] N. Horiuchi, “Terahertz optics: Silk foam waveguides,” *Nature Photonics*, vol. 8, p. 812, 2014.
- [26] H. Guerboukha, A. Markov, H. Qu, and M. Skorobogatiy, “Time resolved dynamic measurements at THz frequencies using a rotary optical delay line,” *IEEE Transactions on Terahertz Science and Technology*, 2015, (accepted).
- [27] M. Skorobogatiy, “Linear rotary optical delay lines,” *Optics Express*, vol. 22, no. 10, pp. 11 812–11 833, 2014.
- [28] D. H. Auston, “Picosecond optoelectronic switching and gating in silicon,” *Applied Physics Letters*, vol. 26, no. 3, pp. 101–103, 1975.
- [29] M. C. Beard, G. M. Turner, and C. A. Schmuttenmaer, “Subpicosecond carrier dynamics in low-temperature grown GaAs as measured by time-resolved terahertz spectroscopy,” *Journal of Applied Physics*, vol. 90, no. 12, pp. 5915–5923, 2001.
- [30] Y.-S. Lee, *Principles of Terahertz Science and Technology*. Springer, 2009, ch. Generation and Detection of Broadband Terahertz Pulses.
- [31] L. Duvillaret, F. Garet, J.-F. Roux, and J.-L. Coutaz, “Analytical modeling and optimization of terahertz time-domain spectroscopy experiments using photoswitches as antennas,” *IEEE Journal on Selected Topics in Quantum Electronics*, vol. 7, no. 4, pp. 615–623, 2001.

- [32] Z. Piao, M. Tani, and K. Sakai, "Carrier dynamics and THz radiation in biased semiconductor structures," in *Proceedings of the SPIE*, vol. 2145, 1999, pp. 49–56.
- [33] P. R. Smith, D. H. Auston, and M. C. Nuss, "Subpicosecond photoconducting dipole antennas," *IEEE Journal of Quantum Electronics*, vol. 24, no. 2, pp. 255–260, 1988.
- [34] D. Grischkowsky, S. Keiding, M. van Exter, and C. Fattinger, "Far-infrared time-domain spectroscopy with terahertz beams of dielectrics and semiconductors," *Journal of the Optical Society of America B*, vol. 7, no. 10, pp. 2006–2015, 2006.
- [35] M. Naftaly and R. Dudley, "Terahertz reflectivities of metal-coated mirrors," *Applied Optics*, vol. 50, no. 19, pp. 3201–3204, 2011.
- [36] J. H. Scofield, "Frequency-domain description of a lock-in amplifier," *American Journal of Physics*, vol. 62, no. 2, pp. 129–133, 1994.
- [37] M. V. Exter, C. Fattinger, and D. Grischkowsky, "Terahertz time-domain spectroscopy of water vapor," *Optics Letters*, vol. 14, no. 20, pp. 1128–1130, 1989.
- [38] R. A. Cheville and D. Grischkowsky, "Far-infrared foreign and self-broadened rotational linewidths of high-temperature water vapor," *Journal of the Optical Society of America B*, vol. 16, no. 2, pp. 317–322, 1999.
- [39] R. W. McGowan, G. Gallot, and D. Grischkowsky, "Propagation of ultrawideband short pulses of terahertz radiation through submillimeter-diameter circular waveguides," *Optics Letters*, vol. 24, no. 20, pp. 1431–1433, 1999.
- [40] G. Gallot, S. P. Jamison, R. W. McGowan, and D. Grischkowsky, "Terahertz waveguides," *Journal of the Optical Society of America B*, vol. 17, no. 5, pp. 851–863, 2000.
- [41] R. Mendis and D. Grischkowsky, "THz interconnect with low-loss and low-group velocity dispersion," *IEEE Microwave and Wireless Components Letters*, vol. 11, no. 11, pp. 444–446, 2001.
- [42] R. Mendis and D. Grischkowsky, "Undistorted guided-wave propagation of subpicosecond terahertz pulses," *Optics Letters*, vol. 26, no. 11, pp. 846–848, 2001.
- [43] K. Wang and D. M. Mittleman, "Metal wires for terahertz wave guiding," *Nature*, vol. 432, pp. 376–379, 2004.
- [44] T.-I. Jeon, J. Zhang, and D. Grischkowsky, "THz sommerfeld wave propagation on a single metal wire," *Applied Physics Letters*, vol. 86, no. 16, p. 161904, 2005.

- [45] M. Mbonye, R. Mendis, and D. M. Mittleman, “A terahertz two-wire waveguide with low bending loss,” *Applied Physics Letters*, vol. 95, no. 23, p. 233506, 2009.
- [46] S. P. Jamison, R. W. McGowan, , and D. Grischkowsky, “Single-mode waveguide propagation and reshaping of sub-ps terahertz pulses in sapphire fibers,” *Applied Physics Letters*, vol. 76, no. 15, pp. 1987–1989, 2000.
- [47] R. Mendis and D. Grischkowsky, “Plastic ribbon THz waveguides,” *Journal of Applied Physics*, vol. 88, no. 7, pp. 4449–4451, 2000.
- [48] L.-J. Chen, H.-W. Chen, T.-F. Kao, J.-Y. Lu, and C.-K. Sun, “Low-loss subwavelength plastic fiber for terahertz waveguiding,” *Optics Letters*, vol. 31, no. 3, pp. 308–310, 2006.
- [49] H.-W. Chen, Y.-T. Li, C.-L. Pan, J.-L. Kuo, J.-Y. Lu, L.-J. Chen, and C.-K. Sun, “Investigation on spectral loss characteristics of subwavelength terahertz fibers,” *Optics Letters*, vol. 32, no. 9, pp. 1017–1019, 2007.
- [50] H. Han, H. Park, M. Cho, and J. Kim, “Terahertz pulse propagation in a plastic photonic crystal fiber,” *Applied Physics Letters*, vol. 80, no. 15, pp. 2634–2636, 2002.
- [51] T. Hidaka, H. Minamide, H. Ito, J.-I. Nishizawa, K. Tamura, and S. Ichikawa, “Ferroelectric PVDF cladding terahertz waveguide,” *Journal of Lightwave Technology*, vol. 23, no. 8, pp. 2469–2473, 2005.
- [52] C.-H. Lai, Y.-C. Hsueh, H.-W. Chen, Y.-J. Huang, H.-C. Chang, and C.-K. Sun, “Low-index terahertz pipe waveguides,” *Optics Letters*, vol. 34, no. 21, pp. 3457–3459, 2009.
- [53] A. Dupuis, K. Stoeffler, B. Ung, C. Dubois, and M. Skorobogatiy, “Transmission measurements of hollow-core THz bragg fibers,” *Journal of the Optical Society of America B*, vol. 28, no. 4, pp. 896–907, 2011.
- [54] M. Skorobogatiy and A. Dupuis, “Ferroelectric all-polymer hollow bragg fibers for terahertz guidance,” *Applied Physics Letters*, vol. 90, no. 11, p. 113514, 2007.
- [55] B. Ung, A. Mazhorova, A. Dupuis, M. Rozé, , and M. Skorobogatiy, “Polymer microstructured optical fibers for terahertz wave guiding,” *Optics Express*, vol. 19, no. 26, pp. B848–B861, 2011.
- [56] A. Dupuis, “Dielectric THz waveguides,” Ph.D. dissertation, Ecole Polytechnique de Montréal, 2010.

- [57] S. Atakaramians, S. A. V., T. M. Monro, and D. Abbott, “Terahertz dielectric waveguides,” *Advances in Optics and Photonics*, vol. 5, no. 2, pp. 169–215, 2013.
- [58] M. Yan and N. A. Mortensen, “Hollow-core infrared fiber incorporating metal-wire metamaterial,” *Optics Express*, vol. 17, no. 17, pp. 14 851–14 864, 2009.
- [59] J. A. Harrington, R. George, P. Pedersen, and E. Mueller, “Hollow polycarbonate waveguides with inner Cu coatings for delivery of terahertz radiation,” *Optics Express*, vol. 12, no. 21, pp. 5263–5268, 2004.
- [60] A. Markov and M. Skorobogatiy, “Two-wire terahertz fibers with porous dielectric support,” *Optics Express*, vol. 21, no. 10, pp. 12 728–12 743, 2013.
- [61] J. Anthony, R. Leonhardt, and A. Argyros, “Hybrid hollow core fibers with embedded wires as THz waveguides,” *Optics Express*, vol. 21, no. 3, pp. 2903–2912, 2013.
- [62] A. Markov, H. Guerboukha, A. Argyros, and M. Skorobogatiy, “A complementary study to “hybrid hollow core fibers with embedded wires as THz waveguides” and “two-wire terahertz fibers with porous dielectric support:” comment,” *Optics Express*, vol. 21, no. 23, pp. 27 802–27 803, 2013.
- [63] N. Yudasari, J. Anthony, and R. Leonhardt, “Terahertz pulse propagation in 3D-printed waveguide with metal wires component,” *Optics Express*, vol. 22, no. 21, pp. 26 042–26 054, 2014.
- [64] G. Zhao, M. Mors, T. Wenckebach, and P. Planken, “Terahertz dielectric properties of polystyrene foam,” *Journal of the Optical Society of America B*, vol. 19, no. 6, pp. 1476–1479, 2002.
- [65] C. Roman, O. Ichim, L. Sarger, V. Vigneras, and P. Mounaix, “Terahertz dielectric characterisation of polymethacrylimide rigid foam: the perfect sheer plate?” *Electronics Letters*, vol. 40, no. 19, pp. 1167–1169, 2004.
- [66] G. H. Altman, F. Diaz, C. Jakuba, T. C. Rebecca, L. Horan, J. Chen, H. Lu, J. Richmond, and D. L. Kaplan, “Silk-based biomaterials,” *Biomaterials*, vol. 24, no. 3, pp. 401–416, 2003.
- [67] V. Elisseeff, *The Silk Roads: Highways of Culture and Commerce*. Berghahn Books, 2000.
- [68] S. Vainker, *Chinese Silk: A Cultural History*. Rutgers University Press, 2000.

- [69] H. Perry, A. Gopinath, D. L. Kaplan, L. D. Negro, and F. G. Omenetto, “Nano- and micropatterning of optically transparent, mechanically robust, biocompatible silk fibroin films,” *Advanced Materials*, vol. 20, no. 16, pp. 3070–3072, 2008.
- [70] S. T. Parker, P. Domachuk, J. Amsden, J. Bressner, J. A. Lewis, D. L. Kaplan, and F. G. Omenetto, “Biocompatible silk printed optical waveguides,” *Advanced Materials*, vol. 21, no. 23, pp. 2411–2415, 2009.
- [71] A. K. Manocchi, P. Domachuk, F. G. Omenetto, and H. Yi, “Facile fabrication of gelatin-based biopolymeric optical waveguides,” *Biotechnology and Bioengineering*, vol. 103, no. 4, pp. 725–732, 2009.
- [72] R. Capelli, J. J. Amsden, G. Generali, S. Toffanin, V. Benfenati, M. Muccini, D. L. Kaplan, F. G. Omenetto, and R. Zamboni, “Integration of silk protein in organic and light-emitting transistors,” *Organic Electronics*, vol. 12, no. 7, pp. 1146–1151, 2011.
- [73] K. Tsioris, W. K. Raja, E. M. Pritchard, B. Panilaitis, D. L. Kaplan, and F. G. Omenetto, “Fabrication of silk microneedles for controlled-release drug delivery,” *Advanced Functional Materials*, vol. 22, no. 2, pp. 330–335, 2011.
- [74] D.-H. Kim, J. Viventi, J. J. Amsden, J. Xiao, L. Vigeland, Y.-S. Kim, J. A. Blanco, B. Panilaitis, E. S. Frechette, D. Contreras, D. L. Kaplan, F. G. Omenetto, Y. Huang, K.-C. Hwang, M. R. Zakin, B. Litt, and J. A. Rogers, “Dissolvable films of silk fibroin for ultrathin conformal bio-integrated electronics,” *Nature Materials*, vol. 9, no. 6, pp. 511–517, 2010.
- [75] D. H. Kim, Y. S. Kim, J. Amsden, B. Panilaitis, D. L. Kaplan, F. G. Omenetto, M. R. Zakin, and J. A. Rogers, “Silicon electronics on silk as a path to bioresorbable, implantable devices,” *Applied Physics Letters*, vol. 95, no. 13, p. 133701, 2009.
- [76] B. D. Lawrence, J. K. Marchant, M. A. Pindrusa, F. G. Omenetto, and D. L. Kaplan, “Silk film biomaterials for cornea tissue engineering,” *Biomaterials*, vol. 30, no. 7, pp. 1299–1308, 2009.
- [77] H. Tao, S. M. Siebert, M. A. Brenckle, R. D. Averitt, M. Cronin-Golomb, D. L. Kaplan, and F. G. Omenetto, “Gold nanoparticle-doped biocompatible silk films as a path to implantable thermo-electrically wireless powering devices,” *Applied Physics Letters*, vol. 97, no. 12, p. 123702, 2010.

- [78] C. Li, C. Vepari, H.-J. Jin, H. J. Kim, and D. L. Kaplan, “Electrospun silk-BMP-2 scaffolds for bone tissue engineering,” *Biomaterials*, vol. 27, no. 16, pp. 3115–3124, 2006.
- [79] S. E. Wharram, X. H. Zhang, D. L. Kaplan, and S. P. McCarthy, “Electrospun silk material systems for wound healing,” *Macromolecular Bioscience*, vol. 10, no. 3, pp. 246–257, 2010.
- [80] G. H. Altmana, R. L. Horana, H. H. Lua, J. Moreaua, I. Martinb, J. C. Richmondc, and D. L. Kaplan, “Silk matrix for tissue engineered anterior cruciate ligaments,” *Biomaterials*, vol. 23, no. 20, pp. 4131–4141, 2002.
- [81] S.-J. He, R. Valluzzi, and S. P. Gido, “Silk I structure in Bombyx mori silk foams,” *International Journal of Biological Macromolecules*, vol. 24, no. 2, pp. 187–195, 1999.
- [82] B. D. Lawrence, M. Cronin-Golomb, I. Georgakoudi, D. L. Kaplan, and F. G. Omenetto, “Bioactive silk protein biomaterial systems for optical devices,” *Biomacromolecules*, vol. 9, no. 4, pp. 1214–1220, 2008.
- [83] J. P. Mondia, J. J. Amsden, D. Lin, L. D. Negro, D. L. Kaplan, and F. G. Omenetto, “Rapid nanoimprinting of doped silk films for enhanced fluorescent emission,” *Advanced Functional Materials*, vol. 22, no. 41, pp. 4596–4599, 2010.
- [84] K. Tsioris, G. E. Tilburey, A. R. Murphy, P. Domachuk, D. L. Kaplan, and F. G. Omenetto, “Functionalized-silk-based active optofluidic devices,” *Advanced Functional Materials*, vol. 20, no. 7, pp. 1083–1089, 2010.
- [85] H. Tao, J. J. Amsden, A. C. Strikwerda, K. Fan, D. L. Kaplan, X. Zhang, R. D. Averitt, and F. G. Omenetto, “Metamaterial silk composites at terahertz frequencies,” *Advanced Materials*, vol. 22, no. 32, pp. 3527–3531, 2010.
- [86] H. Tao, M. A. Brenckle, M. Yang, J. Zhang, M. Liu, S. M. Siebert, R. D. Averitt, M. S. Mannoor, M. C. McAlpine, J. A. Rogers, D. L. Kaplan, and F. G. Omenetto, “Silk-based conformal, adhesive, edible food sensors,” *Advanced Materials*, vol. 24, no. 8, pp. 1067–1072, 2012.
- [87] R. Mendis and D. Grischkowsky, “Plastic ribbon THz waveguides,” *Journal of Applied Physics*, vol. 88, no. 7, pp. 4449–, 2000.
- [88] C. S. P. Jr., R. Pobre, E. Estacio, N. Sarukura, A. Argyros, M. C. J. Large, and M. A. van Eijkelenborg, “Transmission of terahertz radiation using a microstructured polymer optical fiber,” *Optics Letters*, vol. 33, no. 9, pp. 902–904, 2008.

- [89] B. Ung, A. Mazhorova, A. Dupuis, M. Rozé, and M. Skorobogatiy, “Polymer microstructured optical fibers for terahertz wave guiding,” *Optics Express*, vol. 19, no. 26, pp. B848–B861, 2011.
- [90] P. Cebe, X. Hu, D. L. Kaplan, E. Zhuravlev, A. Wurm, D. Arbeiter, and C. Schick, “Beating the heat - fast scanning melts silk beta sheet crystals,” *Scientific Reports*, vol. 3, no. 1130, 2013.
- [91] X. Hu, K. Shmelev, L. Sun, E. S. Gil, S. H. Park, P. Cebe, and D. L. Kaplan, “Regulation of silk material structure by temperature-controlled water vapor annealing,” *Biomacromolecules*, vol. 12, no. 5, pp. 1686–1696, 2011.
- [92] N. C. J. van der Walk, W. A. M. van der Marel, and P. C. M. Planken, “Terahertz polarization imaging,” *Optics Letters*, vol. 30, no. 20, pp. 2802–2804, 2005.
- [93] Z. K. K. H. Ishikawa and, *Structure of Silk Proteins*. Shinkyō Publishing Co ., 1980.
- [94] A. Dupuis, A. Mazhorova, F. Desevedavy, M. Roze, and M. Skorobogatiy, “Spectral characterization of porous dielectric subwavelength THz fibers fabricated using a microstructured molding technique,” *Optics Express*, vol. 18, no. 13, pp. 13 813–13 828, 2010.
- [95] O. Mitrofanov, R. James, F. A. Fernández, T. K. Mavrogordatos, and J. A. Harrington, “Reducing transmission losses in hollow THz waveguides,” *IEEE Transactions on Terahertz Science and Technology*, vol. 1, no. 1, pp. 124–132, 2011.
- [96] M. Naftlay and R. E. Miles, *Terahertz Frequency Detection and Identification of Materials and Objects*. Springer, 2006, ch. Terahertz Beam Interactions with Amorphous Materials, pp. 107–122.
- [97] M. Skorobogatiy, *Nanostructured and Subwavelength Waveguides: Fundamentals and Applications*. Wiley, 2012.
- [98] S. Atakaramians, S. Afshar, V. B. M. Fischer, D. Abbott, and T. M. Monro, “Porous fibers: a novel approach to low loss THz waveguides,” *Optics Express*, vol. 16, no. 121, pp. 8845–8854, 2008.
- [99] D. N. Rockwood, R. C. Preda, T. Yücel, X. Wang, M. L. Lovett, and D. L. Kaplan, “Materials fabrication from *Bombyx mori* silk fibroin,” *Nature Protocols*, vol. 6, no. 10, pp. 1612–1631, 2011.

- [100] M. Tonouchi, “Cutting-edge terahertz technology,” *Nature Photonics*, vol. 1, no. 2, pp. 97–105, 2007.
- [101] D. Edelstein, R. B. Romney, and M. Scheuermann, “Rapid programmable 300 ps optical delay scanner and signal averaging system for ultrafast measurements,” *Review of Scientific Instruments*, vol. 62, no. 3, pp. 579–583, 1991.
- [102] J. Ballif, R. Gianotti, P. Chavanne, R. Walti, and R. P. Salathe, “Rapid and scalable scans at 21 m/s in optical low-coherence reflectometry,” *Optics Letters*, vol. 22, no. 11, pp. 757–759, 1997.
- [103] J. Szydlo, N. Delachenal, R. Gianotti, R. Walti, H. Bleuler, and P. R. Salathe, “Air-turbine driven optical low coherence reflectometry at 28.6 kHz scan repetition rate,” *Optics Communications*, vol. 154, no. 1-3, pp. 1–4, 1998.
- [104] G. G. Lamouche, M. Dufour, B. Gauthier, V. Bartulovic, M. Hewko, and J.-P. Monchalain, “Optical delay line using rotating rhombic prisms,” in *Proceedings of the SPIE*, vol. 6429, 2007, p. 64292G.
- [105] T. Probst, A. Rehn, S. F. Busch, S. Chatterjee, M. Koch, and M. Scheller, “Cost-efficient delay generator for fast terahertz imaging,” *Optics Letters*, vol. 39, no. 16, pp. 4863–4866, 2014.
- [106] P.-L. Hsiung, X. Li, C. Chudoba, I. Hartl, T. H. Ko, and J. G. Fujimoto, “High-speed path-length scanning with a multiple-pass cavity delay line,” *Applied Optics*, vol. 42, no. 4, pp. 640–648, 2003.
- [107] L. Liu and N. G. Chen, “Double-pass rotary mirror array for fast scanning optical delay line,” *Applied Optics*, vol. 45, no. 21, pp. 5426–5431, 2003.
- [108] X. Liu, M. J. Cobb, and X. Li, “Rapid scanning all-reflective optical delay line for real-time optical coherence tomography,” *Optics Letters*, vol. 29, no. 1, pp. 80–82, 2004.
- [109] K. Locharoenrat and I. J. Hsu, “Optical delay line for rapid scanning low-coherence reflectometer,” *International Journal of Information and Electronics Engineering*, vol. 2, no. 6, pp. 904–906, 2012.
- [110] C.-L. Wang and C.-L. Pan, “Scanning optical delay device having a helicoid reflecting mirror,” Patent US 5 907 423 A, 1999.
- [111] T. D. Dorney, “Scanning optical delay line using a reflective element arranged to rotate,” Patent US 7,046,412, 2006.

- [112] G. J. Kim, Y. S. Jin, S. G. Jeon, and J. I. Kim, "Rotary optical delay line," Patent US 7 453 619 B2, 2008.
- [113] J. Xu and X.-C. Zhang, "Circular involute stage," *Optics Letters*, vol. 29, no. 17, pp. 2082–2084, 2004.
- [114] G.-J. Kim, S.-G. Jeon, J.-I. Kim, and Y.-S. Jin, "High speed scanning of terahertz pulse by a rotary optical delay line," *Review of Scientific Instruments*, vol. 79, no. 10, p. 106102, 2008.
- [115] H. Qu and M. Skorobogatiy, "Design of the curvilinear reflectors for linear rotary optical delay lines," in *International Optical Design Conference*, 2014, p. IM2B.4.
- [116] A. Bartels, R. Cerna, C. Kistner, A. Thoma, F. Hudert, C. Janke, and T. Dekorsy, "Ultrafast time-domain spectroscopy based on high-speed asynchronous optical sampling," *Review of Scientific Instruments*, vol. 78, no. 3, p. 035107, 2007.
- [117] M. Naftaly, "Metrology issues and solutions in THz time-domain spectroscopy," *IEEE Sensors Journal*, vol. 13, no. 1, pp. 8–17, 2013.
- [118] ASTM D3539-11, "Standard test methods for evaporation rates of volatile liquids by shell thin-film evaporimeter," *ASTM International*, 2011.
- [119] J. R. Birch, "The far infrared optical constants of polyethylene," *Infrared Physics*, vol. 30, no. 2, pp. 195–197, 1990.
- [120] J. L. Price and J. Links, *Medical imaging signals and systems*. Pearson, 2006, ch. Computed tomography.
- [121] Matlab. Inverse radon transform. [Online]. Available: <http://www.mathworks.com/help/images/ref/iradon.html;jsessionid=eeddf29752e4e7addcaf12590734>
- [122] J. H. Hubbell and S. M. Seltzer. Tables of x-ray mass attenuation coefficients and mass energy-absorption coefficients. [Online]. Available: <http://physics.nist.gov/xaamdi>
- [123] B. Ferguson, S. Wang, D. Gray, D. Abbot, and X.-C. Zhang, "T-ray computed tomography," *Optics Letters*, vol. 27, no. 15, pp. 1312–1314, 2002.
- [124] X. Yin, B. W.-H. Ng, and D. Abbott, *Terahertz imaging for biomedical applications: pattern recognition and tomographic reconstruction*. Springer Science and Business Media, 2012, ch. Terahertz computed tomography.

- [125] B. Recur, A. Younus, S. Salort, P. Mounaix, B. Chassagne, P. Desbarats, J.-P. Caumes, and E. Abraham, “Investigation on reconstruction methods applied to 3D terahertz computed tomography,” *Optics Express*, vol. 19, no. 6, pp. 5105–5117, 2011.
- [126] B. Recur, J. P. Guillet, I. Manek-Hönninger, J. C. Delagnes, W. Benharbone, P. Desbarats, J. P. Domenger, L. Canioni, and P. Mounaix, “Propagation beam consideration for 3D THz computed tomography,” *Optics Express*, vol. 20, no. 6, pp. 5817–5829, 2012.
- [127] M. Jewariya, E. Abraham, T. Kitaguchi, Y. Ohgi, M.-A. Minami, T. Araki, and T. Yasui, “Fast three-dimensional terahertz computed tomography using real-time line projection of intense terahertz pulse,” *Optics Express*, vol. 19, no. 6, pp. 5105–5117, 2011.
- [128] B. M. F. H. Lin, C. Fumeaux and D. Abbott, “Modelling of sub-wavelength THz sources as gaussian apertures,” *Optics Express*, vol. 18, no. 17, pp. 17 672–17 683, 2010.
- [129] C. Defonseka, *Practical guide to flexible polyurethane foams*. Smithers Rapra, 2013, ch. Polyurethane raw materials.
- [130] A. H. Landrock, Ed., *Handbook of Plastic Foams*. Noyes Publication, 1995.
- [131] J. R. Mauney, T. Nguyen, K. Gillen, J. M. G. C. Kirker-Head, and D. L. Kaplan, “Engineering adipose-like tissue in vitro and in vivo utilizing human bone marrow and adipose-derived mesenchymal stem cells with silk fibroin 3D scaffolds,” *Biomaterials*, vol. 28, no. 35, pp. 5280–5290, 2007.
- [132] M. M. Awad and R. A. Cheville, “Transmission terahertz waveguide-based imaging below the diffraction limit,” *Applied Physics Letters*, vol. 86, no. 22, p. 22107, 2005.
- [133] B. Reitemeier, S. F. Busch, T. Probst, M. Scheller, and M. Koch, “Low-cost delay line for fast terahertz imaging,” in *38th International Conference on Infrared, Millimeter, and Terahertz Waves*, no. 13916056, 2013.